Contrib Mineral Petrol (2015) 170:5
DOI 10.1007/s00410-015-1155-2

ORIGINAL PAPER

Fine-scale temporal recovery, reconstruction and evolution of a post-supereruption magmatic system

Simon J. Barker[1,2] · **Colin J. N. Wilson**[1] · **Aidan S. R. Allan**[1,3] · **C. Ian Schipper**[1,4]

Received: 22 January 2015 / Accepted: 9 June 2015 / Published online: 7 July 2015

Abstract Supereruptions ($>10^{15}$ kg $\approx$ 450 km^3 of ejected magma) have received much attention because of the challenges in explaining how and over what time intervals such large volumes of magma are accumulated, stored and erupted. However, the processes that follow supereruptions, particularly those focused around magmatic recovery, are less fully documented. We present major and trace-element data from whole-rock, glass and mineral samples from eruptive products from Taupo volcano, New Zealand, to investigate how the host magmatic system reestablished and evolved following the Oruanui supereruption at 25.4 ka. Taupo's young eruptive units are precisely constrained chronostratigraphically, providing uniquely fine-scale temporal snapshots of a post-supereruption magmatic system. After only ~5 kyr of quiescence following the Oruanui eruption, Taupo erupted three small volume (~0.1 km^3) dacitic pyroclastic units from 20.5 to 17 ka, followed by another ~5-kyr-year time break, and then eruption of 25 rhyolitic units starting at ~12 ka. The dacites show strongly zoned minerals and wide variations in melt-inclusion compositions, consistent with early magma mixing followed by periods of cooling and crystallisation at depths of >8 km, overlapping spatially with the inferred basal parts of the older Oruanui silicic mush system. The dacites reflect the first products of a new silicic system, as most of the Oruanui magmatic root zone was significantly modified in composition or effectively destroyed by influxes of hot mafic magmas following caldera collapse. The first rhyolites erupted between 12 and 10 ka formed through shallow (4–5 km depth) cooling and fractionation of melts from a source similar in composition to that generating the earlier dacites, with overlapping compositions for melt inclusions and crystal cores between the two magma types. For the successively younger rhyolite units, temporal changes in melt chemistry and mineral phase stability are observed, which reflect the development, stabilisation and maturation of a new, probably unitary, silicic mush system. This new mush system was closely linked to, and sometimes physically interacted with, underlying mafic melts of similar composition to those involved in the Oruanui supereruption. From the inferred depths of magma storage and geographical extent of vent sites, we consider that a large silicic mush system (>200 km^3 and possibly up to 1000 km^3 in volume) is now established at Taupo and is capable of feeding a new episode or cycle of volcanism at any stage in the future.

Keywords Supereruption · Taupo Volcanic Zone · Caldera · Rhyolite · Taupo volcano

Introduction

Supereruptions are defined as those that eject $>10^{15}$ kg (or ~450 km^3) of magma, equivalent to >1000 km^3 of

---

Communicated by Gordon Moore.

Electronic supplementary material The online version of this article (doi:10.1007/s00410-015-1155-2) contains supplementary material, which is available to authorized users.

✉ Simon J. Barker
smnbarker@gmail.com

[1] School of Geography, Environment and Earth Sciences, Victoria University of Wellington, P.O. Box 600, Wellington 6140, New Zealand

[2] School of Environment, University of Auckland, Private Bag 92019, Auckland 1142, New Zealand

[3] Environmental Protection Authority, PO Box 63002, Wellington 6140, New Zealand

[4] R&D Center for Ocean Drilling Science, Japan Agency for Marine-Earth Science and Technology (JAMSTEC), 2-15 Natsushima-cho, Yokosuka, Kanagawa 237-0061, Japan

pyroclastic material (see Miller and Wark 2008 for overview), and are often interpreted to result from a unique set of circumstances that lead to the accumulation and mobilisation of large amounts of magma (Caricchi et al. 2014; Malfait et al. 2014). It is now widely regarded that significant volumes of partly molten crystal-rich mush are required to generate the huge volumes of melt(s) required for supereruptions (Bachmann and Bergantz 2004, 2008; Hildreth 2004; Glazner et al. 2004; Wilson et al. 2006; Hildreth and Wilson 2007; Lipman 2007; Girard and Stix 2009; Wilson and Charlier 2009; Allan 2013; Lipman and Bachmann 2015). Such studies often highlight the crucial interplay of this evolved crystal mush with a deeper-seated feeder system of less evolved mafic melts and their crystalline products (Hildreth 1981). This feeder system not only supplies a heat source and fractionation products to the base of the magma reservoir, but may also affect the longevity and stability of the overlying mush system (Hildreth 2004; Bachmann and Bergantz 2008). The evacuation of supereruptive volumes of magma from a chamber will then undoubtedly have significant effects on the deeper subvolcanic reservoir, as well as the overall regional structure of the crust. Questions then arise as to how, and on what timescales, the host magmatic system rebuilds and evolves following a supereruption. For example, how does the catastrophic release of vast amounts of magma affect the structure of the magmatic system as a whole [i.e. the melt-dominant zone, crystal mush zone and crustal reservoir of Hildreth and Wilson (2007)] and the chemical composition of the melts it produces? How long does it take for the magmatic system to reestablish to the point where eruptions resume? Such questions are central to understanding the dynamics of supervolcanoes and for building a framework for future hazard assessments.

One of the biggest challenges in assessing supervolcanic recovery processes is the scarcity of detail about activity that occurred immediately post-supereruption in the geological record. This scarcity may arise from the lack of long-term preservation of smaller eruptive units bracketing a supereruption. In older examples, the uncertainties of the methods employed to date eruptions are often larger than the interval between eruptions (e.g. 10^4–10^5 years using ^{40}Ar/^{39}Ar or U–Pb systematics: Simon et al. 2014). Having a record of magmatic activity through closely spaced eruptions coupled with preservation of their products is critical for tracing the immediate post-supereruption reorganisation of a magmatic system.

Located in the central North Island of New Zealand, Taupo volcano provides a unique opportunity to investigate the dynamics of both pre- and post-supereruption magmatic systems because of its young age, high eruptive frequency and the high degree of preservation of its eruptive products. The young eruptive history of Taupo is exceptionally well constrained by field stratigraphy, radiocarbon dating and correlation with other young tephras from the Taupo Volcanic Zone (TVZ) (Wilson 1993; Wilson et al. 2009). Taupo's caldera was primarily formed in the catastrophic 25.4 ka Oruanui event, the world's youngest supereruption, which evacuated >530 km^3 of magma (>1100 km^3 of pyroclastic material) (Wilson 2001; Wilson et al. 2006; Vandergoes et al. 2013; Allan 2013; Allan et al. 2012, 2013; Fig. 1). U–Th disequilibrium model-age contrasts between zircons extracted from the precursor 'Oruanui-type' magmas and those from the Oruanui magma itself (Wilson and Charlier 2009) and element diffusion modelling (Allan et al. 2013) indicate that although the broader Oruanui mush source likely developed over tens of thousands of years, the eruptible melt-dominant magma body was accumulated in 3000 years or less. The Oruanui juvenile material was >99 % rhyolite, with a minor (<1 %) component of mafic magmas (Sutton et al. 1995; Wilson et al. 2006). Investigation of pumice compositions has shown that there was a complex range of rhyolite melts involved, with a dominant high-silica rhyolite (HSR), minor amounts of a low-silica rhyolite (LSR) and traces of an independent biotite-bearing (BtB) magma introduced via syneruptive diking from the contemporaneous NE dome magmatic system (Wilson et al. 2006; Allan et al. 2012; Allan 2013; Fig. 1a). In addition, crystals and melts from Quaternary intrusions and Mesozoic greywacke metasediments were incorporated into the melt-dominant magma body during its growth (Liu et al. 2006; Charlier et al. 2008).

Despite evacuating a large volume of magma during the Oruanui eruption, Taupo resumed erupting after only ~5 kyr, albeit on a smaller scale. There have been 28 eruptions following the Oruanui, 25 of which occurred in the last 12 kyr, with the largest at 232 ± 5 AD (Wilson 1993; Hogg et al. 2012; Fig. 1; Table 1). The first post-Oruanui eruptions (21–17 ka) were dacitic and erupted from the northern segment of the Oruanui caldera (units Ψ, Ω and A). The remaining eruptions are clustered into three temporally and chemically distinct rhyolitic subgroups (SG1–3), erupted from multiple vents in discrete periods from 11.8 to 9.95 ka (SG1: units B–E), 7.05–2.75 ka (SG2: units F–W) and 2.15–1.8 ka (SG3: units X–Z) (Sutton et al. 1995, 2000; Fig. 1; Table 1). Taupo's magmatic system demonstrably underwent significant changes following the supereruption. For example, contrasting zircon ages for the Oruanui and post-Oruanui magmas suggests that the system underwent significant heating, thermally resetting the chronological history of the magmatic system (Charlier et al. 2005, 2010; Barker et al. 2014). However, questions remain as to how and when the rhyolite-generating magmatic system was reestablished following the Oruanui eruption (e.g. Sutton et al. 2000). In particular, how did the mush system and deeper root zone

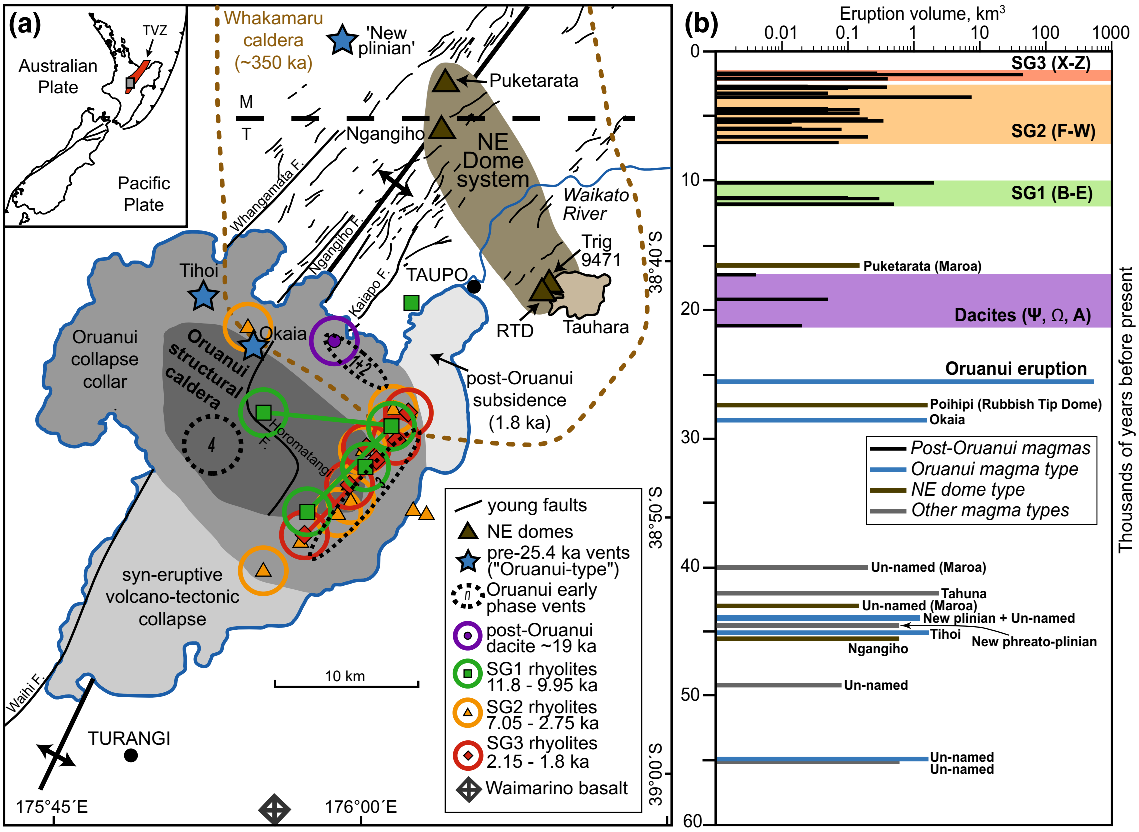

Fig. 1 Regional setting, structural features and eruptive history of Taupo volcano in the Taupo Volcanic Zone (TVZ), New Zealand (*map inset*) (modified from Wilson and Charlier 2009). **a** Map of Lake Taupo (*blue outline*) and surrounding structural and volcanic features. Lineations are young NNE–SSW surface faults. *Thick black line* with *double arrow* represents the Taupo Fault Belt rift axis from Rowland et al. (2010). The *horizontal black dashed line* marks the arbitrary boundary between Taupo (T) and Maroa (M) volcanoes, and the *brown dotted line* represents the inferred Whakamaru caldera boundary (Wilson et al. 1986). The Oruanui structural caldera, subsequent caldera collapse (*grey regions*) and approximate vent areas for the first four phases of the Oruanui eruption are from Wilson (2001). The NE dome system and pre-Oruanui vent sites are after Wilson and Charlier (2009). Inferred vent sites for the post-Oruanui eruptions with implied uncertainty of vent locations (*circle* around *symbol*) are modified from Wilson (1993). *Coloured tie lines* joining post-Oruanui vent sites represent shifting vent locations within single eruptions. Note the shift in vent site between the Ω dacite and post-Oruanui rhyolites, and the cluster of vent sites near the eastern lake shore, especially for the SG3 eruptions. **b** Eruptive history of the Taupo–Maroa area over the past 60 ka with approximate volumes of erupted magma shown on a log scale. Magma volumes are shown as dense rock equivalent (DRE). Eruptive ages and volume estimates are from Wilson et al. (2009), Wilson and Charlier (2009) and references therein. The Oruanui eruption age is from Vandergoes et al. (2013)

(including the inferred underlying mafic feeder system) adjust, recover and chemically evolve to start producing new suites of dacite and rhyolite eruptives? What are the modern components of the magma reservoir and where are they located?

Here, we address these questions through a study of magma chemistry for the 28 post-Oruanui eruptions. Major and trace-element compositions of whole rock, glass and minerals from pyroclasts and lava are used to constrain processes involved in Taupo's post-supereruption reconstruction to the latest eruption only ~1800 years ago. This study demonstrates how Taupo's magmatic system was reestablished and then evolved at multiple critical stages, to build a new unitary silicic mush system that most recently fed one of the largest and most energetic Holocene eruptions on Earth.

Eruptive stratigraphy and sampling

The onset of modern explosive activity at Taupo commenced shortly after the Rotoiti eruption (~60 ka) from the nearby Okataina volcano (Wilson et al. 1995). The period between ~60 and 25 ka was dominated by small pyroclastic eruptions from vents now mostly concealed beneath Lake Taupo, interspersed with a series of small but chemically distinct eruptions from Maroa volcano to the north (Wilson et al. 1995; Sutton et al. 1995; Wilson and Charlier 2009;

Table 1 Summary of post-Oruanui (<25.4 ka) eruptive stratigraphy from Taupo volcano (modified from Wilson 1993)

Eruption unit	Published names	Calibrated age (years BP)	Volume (km^3)	Eruption and deposit characteristics	Material sampled
Oruanui formation		25,400	>1100	Supereruption, formed modern caldera outline	See Wilson et al. (2006), Allan (2013) for separate study
Ψ*		20,500	0.05	Small, dry open vent switching to wet, possible lava dome	Pumice lapilli, with isolated clasts up to ~5 cm
Ω*		18,800	0.1	Plinian fall unit, open vent, dry switching to wet activity	Pumice lapilli and isolated blocks up to ~10 cm
A*		17,000	0.01	Small wet event accompanying lava extrusion	Coarse ash to fine pumice lapilli. Bulk sample only
B*	Karapiti Tephra	11,800	1.4	Bilobate fall deposit, multiple styles, vent sites and layers	Subunits B1 and B3
Subunit B1*			0.23	Mostly dry erupted, non-bedded plinian fall	Pumice lapilli, with isolated clasts up to ~5 cm
Subunit B2			0.1	High lithic content, vent moving NE from B1	n/a
Subunit B3*			0.15	Poorly bedded, inverse graded, only exposed in north	Pumice lapilli and isolated blocks up to 10 cm
Subunit B4			0.82	Two vents possibly active together, possible lava extrusion	n/a
C*	Poronui Tephra	11,400	0.75	Plinian fall deposit, multiple layers reflecting variable power	Subunit C1
Subunit C1*			0.55	Inverse grading, increasing lithics, vent slumping	Pumice lapilli and isolated blocks up to 10 cm
Subunit C2			0.2	Weak explosive activity, possible lava extrusion	n/a
D*		11,380	0.2	Fall deposit accompanying lava dome extrusion on land	Lava from dome. Fine lapilli fall equivalent, bulk sample only
E*	Opepe Tephra	9950	4.8	Large complex eruption, multiple vents and layers	Subunits E1 and E3
Subunit E1*			1	Dry fall, erupted from western vent. Fluctuating vigour	Pumice lapilli, with isolated clasts up to ~5 cm
Subunit E2			0.15	Erupted 9 km East of E1, inverse graded thin fall layer	n/a
Subunit E3*			1.95	Powerful voluminous dry Plinian event, becoming episodic	Pumice blocks, large individual clasts up to 20 cm
Subunit E4			1.5	Poorly bedded and poorly sorted fall unit, water flushed	n/a
Subunit E5			0.2	Ignimbrite unit (column collapse), reached ~20 km from vent	n/a
F*		7050	0.12	Fall unit, dense material. Inferred Motutaiko Is. dome forming	Lava from dome. Fine lapilli fall equivalent, bulk sample only
G*	Motutere Tephra	6650	0.5	Fall unit, decreasing power and variable water interaction	Subunit G1
Subunit G1*			0.2	Plinian pumice fall, increasing vigour, well sorted	Pumice lapilli and isolated blocks up to 10 cm
Subunit G2			0.3	Water flushed and weakened, wet activity. Lava extrusion.	n/a
H*	Motutere Tephra	6050	0.2	Open vent plinian fall unit followed by wet activity and lava	Subunit H1
Subunit H1*			0.1	Well sorted pumice fall deposit, normal grading	Fine pumice lapilli. Bulk sample only
Subunit H2			0.1	Increasing wet activity accompanied by lava extrusion	n/a
I*	Hinemaiaia Tephra	5950	0.02	Small, wet-erupted poorly vesicular magma, lava extrusion	Coarse ash. Glass sample only

Table 1 continued

Eruption unit	Published names	Calibrated age (years BP)	Volume (km^3)	Eruption and deposit characteristics	Material sampled
J*	Hinemaiaia Tephra	5370	0.02	Small, wet-erupted poorly vesicular magma, lava extrusion	Coarse ash. Glass sample only
K*	Hinemaiaia Tephra	5350	0.35	Complexly bedded fall unit	Subunit K2
Subunit K1			0.13	Variable bedding, water flushed, possible lava extrusion	n/a
Subunit K2*			0.22	More open vent than K1, wet-erupted with fine ash	Pumice lapilli and isolated blocks up to 10 cm
L*	Hinemaiaia Tephra	5300	0.07	Small wet eruption involving moderately vesicular magma	Obsidian lava. Fine lapilli fall equivalent, bulk sample only
M*	Hinemaiaia Tephra	5250	0.2	Mainly dry activity, accompanied by lava extrusion	Pumice lapilli. Bulk sample only
N*	Hinemaiaia Tephra	4850	0.15	Mixed eruption of wet and dry activity, possible lava dome	Pumice lapilli. Bulk sample only
O*	Hinemaiaia Tephra	4800	0.05	Moderately powerful, small size, possible lava extrusion	Pumice lapilli, with isolated clasts up to ~5 cm
P*	Hinemaiaia Tephra	4750	0.05	Very-poorly sorted fall with accompanying lava extrusion	Fine pumice lapilli and obsidian chips. Bulk sample only
Q*	Hinemaiaia Tephra	4550	0.15	Similar to O, moderately powerful and possible lava extrusion	Fine pumice lapilli. Bulk sample only
R*	Hinemaiaia Tephra	4450	0.05	Small, weak fall eruption, open vent, dry becoming wet	Fine pumice lapilli. Bulk sample only
S*	Waimihia Tephra	3550	16.9	Very large dry plinian fall eruption. Mixed magma	Subunits S1 and S2
Subunit S1*	Waimihia plinian pumice		8.2	Fall unit of almost purely white rhyolite pumice	Pumice blocks with very large individual clasts up to 30 cm
Subunit S2*	Waimihia plinian pumice		7.9	Fall unit with increasing amounts of rhyodacite and scoria	Pumice lapilli and blocks, scoria clasts, mixed streaky clasts
Subunit S3*	Waimihia ignimbrite		0.8	Non-welded ignimbrite reaching ~20 km from vent	n/a
T*		3200	0.08	Wet explosive activity possibly accompanying lava extrusion	Fine pumice lapilli and obsidian chips. Bulk sample only
U*	Whakaipo Tephra	2850	0.2	Water flushed wet-erupted fall, possible lava extrusion	Pumice lapilli and obsidian, with isolated clasts up to ~5 cm
V*	Whakaipo Tephra	2800	0.8	Complex and episodic, spasmodic magma supply and extrusion	Pumice lapilli, with isolated clasts up to ~5 cm
W*		2750	0.23	Very weak explosive activity, water interaction and lava dome	Subunit W2
Subunit W1			n/a	Very fine ash bed, no material coarser than ash	n/a
Subunit W2*			n/a	Poorly sorted with ash, lapilli, blocks. Pumices and obsidian	Pumice lapilli and obsidian clast, bulk sample only
X*	Mapara Tephra	2150	0.8	Complex episodic eruption, variable vigour and external water	Subunits X1 and X2
Subunit X1*			n/a	Least water flushed, normal graded, foreign lithics	Pumice lapilli, with isolated clasts up to ~5 cm
Subunit X2*			n/a	Variably water flushed, thickest part of deposit	Pumice lapilli, with isolated clasts up to ~5 cm
Subunit X3			n/a	Increasing obsidian, explosive activity with lava extrusion	n/a
Y*	Taupo tephra	1718 (232 ± 5 AD)	45 (105)	Voluminous eruption with multiple vents and caldera collapse	Subunits Y1 through Y5 and Y7
Subunit Y1*	Initial ash		0.05	Minor wet activity, comparable to Hinemaiaia eruption styles	Basal bulk lapilli and large isolated blocks up to ~30 cm

Table 1 continued

Eruption unit	Published names	Calibrated age (years BP)	Volume (km^3)	Eruption and deposit characteristics	Material sampled
Subunit Y2*	Hatepe plinian pumice		2.5	Mostly uniform well sorted plinian fall deposit. Minor flushing	Pumice lapilli and blocks up 30 cm throughout stratigraphy
Subunit Y3*	Hatepe ash		1.9	Vigorous wet activity, juvenile obsidian. Water gullying	Pumice lapilli and blocks up 10 cm throughout stratigraphy
Subunit Y4*	Rotongaio ash		1.1	3- to 4-week break, wet-erupted fine ash, water flushed	Pumice lapilli and obsidian chips. Bulk sample only
Subunit Y5*	Taupo plinian pumice		7.7	Dry voluminous fall event, high eruption rate, dry deposited	Pumice blocks up to ~15 cm throughout stratigraphy
Subunit Y6*	Early ignimbrite flow units		1.5	Ignimbrite generated and deposited synchronously with Y5	n/a
Subunit Y7*	Taupo ignimbrite		30	Climactic ignimbrite unit, single flow, violent caldera collapse	Large pumice blocks up to 1 m, variable vesicle textures
Z*	Floated giant pumices	~1700	0.28	Subaqueous lava dome extrusion, passive floating pumices	Floated lava blocks, pumiceous dome and mafic inclusions

Published names from Froggatt and Lowe (1990). Ages from Wilson (1993) a combination of ^{14}C ages from material in layers/palaeosols and loosely constrained by older/younger deposits (underlined). Age of Oruanui is from Vandergoes et al. (2013), and age of Taupo is from Hogg et al. (2012). Given volumes are estimates for the amount of erupted material. Unit Y total volume (in brackets) given for the sum of the subunits as well as the volume of material now buried beneath Lake Taupo (from Wilson and Walker 1985). Wet and dry eruption types refer to eruptive style and fragmentation mechanism due to the interaction with external water (see Wilson 1993 for details). Water flushed deposit types have been modified or reworked by rain

* Units sampled for this study. For units D, F and L, both in situ lavas and inferred pyroclastic fall equivalents were sampled. 'Bulk sample only' refers to samples where multiple pumices had to be used to obtain enough material for analytical work

Fig. 1a). Early tephrochronological studies proposed nine post-Oruanui (<25 ka) tephra formations (Baumgart 1954; Healy 1964; Vucetich and Pullar 1973; Froggatt and Lowe 1990); however, after reexamination and reinterpretation of Taupo's post-Oruanui stratigraphy (Wilson 1993), 28 eruptions that vary widely in their eruptive sizes and styles were identified and dated (Fig. 1b; Table 1). For convenience, the 28 eruptions and their accompanying products were labelled by letter, with the two oldest denoted by the Greek letters Ψ and Ω and the remainder labelled from oldest to youngest as A through Z. These 28 eruptions were grouped into four subgroups based on broad chemical variations with time (Sutton et al. 1995, 2000; Fig. 1b).

Samples used in this study were collected within the eruptive stratigraphic framework of Wilson (1993) utilising the reference and type localities therein. Additional sample locations were found, having been exposed by modern infrastructural developments in the Taupo region. The largest and freshest juvenile materials from each eruption were collected for chemical analysis (Table 1). For eruptions that experienced a significant change in eruptive style or vent location, multiple phases of the eruptive sequence were sampled to monitor for compositional variations during single events. For subaerial eruptions D (Acacia Bay Dome), F (Motutaiko Island) and L (White Cliffs dome), both fragments of lava and the inferred fall unit equivalents were sampled for comparison. As Unit S (Waimihia) has been recorded as having multiple magma compositions and mixed pumices (Blake et al. 1992; Sutton et al. 1995), end-member rhyolitic pumice, grey hybrid rhyodacite pumice and discrete mafic clasts were collected for analysis. In addition, basaltic scoria from the nearby monogenetic Waimarino volcano, inferred by Hackett (1985) to be post-Oruanui in age, was sampled for comparison with Oruanui and post-Oruanui mafic compositions (Fig. 1a). Graham and Hackett (1987) described the Waimarino basalt in the context of andesite petrogenesis at Ruapehu volcano, ~40 km to the SW, but here it is compared directly to magmatism at Taupo due to its geographical proximity (Fig. 1a).

Analytical techniques

Due to widely varying eruptive sizes and levels of exposure, not all post-Oruanui deposits contained material appropriate for all types of chemical analysis (Table 1). For large explosive eruptions (e.g. units S and Y), abundant large lapilli or blocks could be sampled through stratigraphic sequences with enough material obtainable from single clasts for analysis. However, for smaller eruptive units such as the 'Hinemaiaia Tephra' sequence (Table 1), material available was generally too small for single-clast analyses and multiple lapilli of similar appearance and size were concentrated by sieving and combined for whole-rock analysis. In the smallest deposits (e.g. units I and J), only medium to coarse ash could be sampled, which was picked under a binocular microscope to ensure only juvenile material was selected for analysis.

Prior to processing, samples were repeatedly rinsed, scrubbed and then washed in an ultrasonic bath to remove adhering fine ash or lithic material. A final rinse was made in Milli-Q water (>18.2 MΩ) before oven drying at 110 °C. Lapilli or block-sized material was coarsely crushed with a Boyd crusher and then split into two equal portions: one portion was sieved and crushed to <2 mm, and the other portion was reserved for whole-rock powdering in an agate Tema. Large crystals were picked from the mineral–glass fraction, and the remaining material was passed through heavy liquids at a density of 2.4–2.5 g/cm^3 to separate groundmass glass from minerals. Minerals were picked under a binocular microscope and mounted into epoxy resin pucks which were polished to expose the crystal cores. For volatile analysis, plagioclase crystals with large melt inclusions were picked and mounted in crystal bond epoxy and prepared as doubly polished wafers using the methods of von Aulock et al. (2014). The glass fraction was sieved to 250 μm, repeatedly rinsed in Milli-Q water and then checked under a microscope for purity.

Whole-rock powders were analysed for major elements by X-ray fluorescence (XRF) at the Open University, UK, using the methods of Ramsey et al. (1995). Approximate 2 standard deviation (2SD) analytical precisions determined by replicate analyses of the same standards for elements are generally <1–3 relative % (Online Resource 1). Trace-element analyses of both whole-rock and glass separates were carried out by solution inductively coupled plasma mass spectrometry (ICP-MS), using a Thermo Scientific Element2 sector-field ICPMS at Victoria University of Wellington. Total procedural blanks were within background levels on all measured elements. Abundances of individual trace elements were calculated by external normalisation relative to a bracketing standard (BHVO-2), which was prepared and analysed under identical conditions to the samples. Approximate 2 SD analytical precisions derived from 19 replicate analyses of a secondary standard (BCR-2) are <6–7 relative % for most trace elements (exceptions are Li, Cr, Cs and Pb at <20 % and Ni, Cu, Nb, Mo, Ta, W at >20 %) (Online Resource 2), with accuracies also <±6–7 % (most are <±1–2 %), apart from Cu at <20 % and Ta at ~25 %. Replicate analyses of an internal Taupo pumice secondary standard have 2 SD precisions <6–7 relative % with similar exceptions to BCR-2.

Major-element analyses of mineral and glass samples were undertaken on a JEOL JXA 8230 electron probe microanalyser (EPMA) at Victoria University of Wellington using wavelength dispersive spectrometry techniques. Operating conditions were 15 kV with 20 nA current for pyroxene and Fe–Ti oxides, 12 nA for amphibole and plagioclase and 8 nA with a defocused 10-μm beam for glass with reduced count times for Na to minimise alkali loss. Calibrated international standards were analysed as unknowns to monitor instrumental drift as well as the precision and accuracy of the analyses. Approximate 2 SD precisions calculated from repeated analyses of calibrated standards are generally <5 relative % for oxides that occur in concentrations of >1 wt% (Online Resource 3). Amphibole and clinopyroxene trace-element compositions were measured in situ using a New Wave deep UV laser (193 nm solid state) coupled to an Agilent 7500CS ICP-MS at Victoria University of Wellington using ^{43}Ca for secondary data normalisation (Pearce et al. 1996), the concentration of which had previously been determined to ±5 % by EPMA. Abundances of individual trace elements for 35-μm spot sizes were calculated relative to bracketing standards BCR-2G or NIST 612. Approximate 2 SD precision and accuracy of replicate analyses is <10 % for most trace elements (Online Resource 4).

H_2O, OH^- and CO_2 concentrations in plagioclase-hosted melt inclusions were determined by Fourier transform infrared spectroscopy (FTIR) using a Varian FTS Stingray 7000 Micro Image Analyser at the Japan Agency for Marine-Earth Science and Technology (JAMSTEC). Replicate analyses ($n = 3$–5) of each inclusion included the collection of both reflection and transmission FTIR spectra (Online Resource 5). Spectra were collected across the near- and mid-IR ranges (8300–800 cm^{-1}) using a heated ceramic (globar) source and a KBr beamsplitter. Background and sample spectra were collected with 512 scans at 8 cm^{-1} resolution, using 20- to 100-μm^2 spot sizes. Backgrounds were taken on a gold-coated disc for reflection and through a KBr disc for transmission. Interference fringes on reflectance spectra were used to determine the beampath, or inclusion thickness at each analytical spot (Tamic et al. 2001; Wysoczanski and Tani 2006; Nichols and Wysoczanski 2007; von Aulock et al. 2014) using a refractive index of 1.48 (Okumura et al. 2003). Absorbance peak heights were determined from transmission spectra using Varian Win-IR Pro software (v3.3.1.014) and converted to concentrations using the Beer–Lambert law. Parameters included the reflectance-determined thicknesses, a nominal rhyolite density of 2.3 g cm^{-3} (Okumura et al. 2003) and the following molar absorptivities: 1.86 mol cm^{-1} for molecular H_2O (H_2O_{mol}) at 5200 cm^{-1} (Ihinger et al. 1994); 1.50 mol cm^{-1} for OH– at 4500 cm^{-1} (Ihinger et al. 1994); and 1214 mol cm^{-1} for CO_{2mol} at 2350 cm^{-1} (Behrens et al. 2004).

Results

Mineralogy

The post-Oruanui eruptive products contain a limited range of mineral phases that vary systematically between eruption subgroups (Table 2). The first-erupted dacitic units contain the highest concentration of crystals (~25 wt%), with dominant plagioclase, then orthopyroxene, clinopyroxene, ilmenite and magnetite. Unit A has slightly lower crystal contents (~17 % wt%); however, we consider this to reflect the fine grain size of the sample collected (Table 1), where the tephra is not representative of the bulk magma due to crystal-glass separation during syneruptive fragmentation and deposition (e.g. Wolff 1985). Apatite and sulphide inclusions are common in the dacite crystals, as previously reported by Sutton et al. (2000) and Gelman et al. (2013). Crystals are often clustered in large glomerocrysts that can reach up to 2 cm in diameter. Individual crystals are typically 1–2 mm in size, but can reach up to 1 cm long. In contrast, the first rhyolites in SG1 (units B and C) are generally crystal poor (<5–7 wt%; Table 2). The mineral assemblage is similar to that of the dacites, but with only minor clinopyroxene, and also minor amphibole. Glomerocrysts are rare, and minerals are typically euhedral to subhedral <1- to 2-mm single crystals. For later eruptions in SG1 (units D and E), clinopyroxene and amphibole become rare, and are found in only trace amounts in Unit E where they are small (<1 mm), and notably subhedral to anhedral. Lava from the Unit D dome has a slightly higher crystal content (~8 wt%), with more glomerocrysts and microlite-rich glass. For the remaining eruptions in SG2 and SG3, all pumices and lavas are generally crystal poor (typically <5 wt%), with mineral phases restricted to plagioclase, orthopyroxene, ilmenite, magnetite and apatite. Clinopyroxene is found only in scoria clasts, mafic inclusions or mixed streaky pumices in Unit S and eruption Z, along with plagioclase, orthopyroxene, magnetite, ilmenite and minor olivine and amphibole (Table 2).

Whole-rock major-element compositions

The major-element compositional spectrum of pumice, lava and mafic clasts spans a wide overall SiO_2 range, broadly similar to the Oruanui eruption products (Fig. 2a; Table 3). Mafic clasts and inclusions from eruptions S, Y and Z have similar major-element compositions to the Oruanui tholeiitic basaltic–andesite to andesite clasts and differ from the Waimarino basalt which instead follows a similar trend to the Oruanui calcalkaline clasts (Fig. 2a; Wilson et al. 2006; Allan 2013). The post-Oruanui dacites have compositions between those of mafic clasts and the rhyolitic pumices, within a relatively narrow compositional range at ~65 % SiO_2, with only Unit A trending towards higher SiO_2 due to the higher proportion of glass in the material sampled. The SG1 eruptions form separate linear trends to other post-Oruanui eruptions on major-element variation diagrams. The first SG1 eruption (Unit B) has the most evolved bulk composition, and the last eruption (Unit E) has the least evolved bulk composition, in agreement with observed changes in mineralogy (Fig. 2b; Table 3). SG1 compositions do not vary significantly with vent position and are indistinguishable between eruptive subunits that experienced a geographical shift in vent site (e.g. B1–B3 and E1–E3: Wilson 1993). SG2 rhyolites have slightly higher SiO_2 than SG1 rhyolites and fall on distinct linear trends for many elements, most notably MnO, Na_2O and CaO, and with higher FeO/MgO. In addition, some clasts from Unit S have slightly lower SiO_2 and were noted as being mixed grey pumices or streaky pumices. SG3 rhyolites fall on similar linear trends to the SG2 rhyolites but with lower SiO_2 and FeO/MgO ratios and higher TiO_2 and MnO.

Whole-rock trace-element compositions

Trace-element concentrations of Unit S and eruption Z mafic clasts confirm their close affinity to the Oruanui tholeiite mafic clasts, with mixed pumices and grey streaky pumices lying on a mixing trend between the mafic clasts and rhyolite pumices, as also observed for the Oruanui by Wilson et al. (2006) (Fig. 3a; Table 3). Rare earth element (REE) patterns for Unit S mafic clasts are identical to a subgroup of the tholeiitic Oruanui mafics (Fig. 3b). However, the Oruanui tholeiitic suite also contains a population of clasts with significantly lower REE concentrations as well as positive Eu anomalies, indicative of primitive melts with extensive plagioclase accumulation (Allan 2013). Post-Oruanui rhyolite trace-element compositions differ from the Oruanui HSR, generally having slightly higher Sr and Zr and also lower light-REE enrichments (Table 3; Fig. 3a). The REE patterns of the post-Oruanui dacites are broadly parallel to the later erupted rhyolites, with SG2 and SG3 rhyolites showing the most enrichment (Fig. 3b).

At a finer scale, there are small yet significant variations in trace-element concentrations in the post-Oruanui eruptions over time (Fig. 4; Table 3). Offsets in compatible trace elements such as Sr and V are consistent with the dacites being less evolved and having higher crystal contents than the SG1 rhyolites. Within the rhyolite subgroups, the largest variation is between the SG1 and SG2 rhyolites, with an increase in Zn, Zr and Sc and a slight decrease in La/Sm and Yb/Gd. Towards the end of SG2, units U–W show an overall decrease in most compatible elements

Table 2 Mineralogy of post-Oruanui eruptive units

Unit	Age (ka)	Mineral content (wt%)	Dominant mineral phases present (in order of relative abundance)	Mineral compositional range and average crystal rim compositions (in italics where determined)				
				Plag An. %	Opx Mg#	Cpx Mg#	Mnt	Ilm
Dacites								
Ψ	20.5	29	Plag, Opx, Cpx, Mnt, Ilm	51–92 *(58 ± 4)*	58–74 *(60 ± 2)*	67–86 *(70 ± 4)*	36–38	79–83
Ω	18.8	27	Plag, Opx, Cpx, Mnt, Ilm	42–83 *(57 ± 4)*	56–71 *(59 ± 2)*	61–75 *(67 ± 4)*	35–41	80–83
A	17	17*	Plag, Opx, Cpx, Mnt, Ilm	48–86 *(57 ± 4)*	55–66 *(60 ± 2)*	67–75 *(70 ± 3)*	36–39	80–83
Subgroup 1 rhyolites								
B1	11.8	5	Plag, Opx, Cpx, Mnt, Ilm, Amp	39–86 *(45 ± 5)*	38–61 *(45 ± 5)*	53–69 *(59 ± 4)*	38–40	88–91
B3	11.8	5	Plag, Opx, Cpx, Mnt, Ilm, Amp	36–85 *(44 ± 4)*	44–63 *(46 ± 4)*	55–68 *(59 ± 4)*	38–40	87–89
C	11.4	7	Plag, Opx, Cpx, Mnt, Ilm, Amp	38–74 *(43 ± 4)*	43–71 *(47 ± 3)*	54–65 *(57 ± 4)*	37–39	87–89
$\mathrm{D_{lava}}$	11.4	7	Plag, Opx, Mnt, Ilm, trace Cpx + Amp	38–82 *(43 ± 5)*	44–65 *(48 ± 3)*	57–67 *(59 ± 3)*	35–37	86–88
$\mathrm{D_{tephra}}$	11.4	6*	Plag, Opx, Mnt, Ilm, trace Cpx	37–85 *(45 ± 5)*	43–64 *(45 ± 4)*	57–70 *(61 ± 3)*	36–39	86–89
E1	10	3	Plag, Opx, Mnt, Ilm, trace Cpx + Amp	35–85 *(43 ± 3)*	44–63 *(46 ± 2)*	55–70 *(61 ± 6)*	38–39	87–88
E3	10	4	Plag, Opx, Mnt, Ilm, trace Cpx + Amp	40–81 *(44 ± 6)*	44–64 *(46 ± 2)*	56–79 *(60 ± 6)*	38–39	87–88
Subgroup 2 rhyolites								
$\mathrm{F_{lava}}$	7.1	7	Plag, Opx, Mnt, Ilm	32–48 *(38 ± 3)*	41–59 *(46 ± 2)*	n/a	41–42	88–90
$\mathrm{F_{tephra}}$	7.1	7*	Plag, Opx, Mnt, Ilm	41–57 *(43 ± 2)*	43–56 *(46 ± 1)*	n/a	37–39	87–89
G	6.7	4	Plag, Opx, Mnt, Ilm	38–55 *(40 ± 1)*	45–59 *(47 ± 1)*	n/a	38–39	87–88
H	6.1	5	Plag, Opx, Mnt, Ilm	39–53 *(42 ± 5)*	44–59 *(46 ± 3)*	n/a	38–39	87–89
K	5.4	5	Plag, Opx, Mnt, Ilm	34–71 *(42 ± 4)*	38–55 *(45 ± 1)*	n/a	39–40	88–91
$\mathrm{L_{lava}}$	5.3	4	Plag, Opx, Mnt, Ilm	35–46 *(40 ± 3)*	43–53 *(45 ± 2)*	n/a	n/d	n/d
$\mathrm{L_{tephra}}$	5.3	3*	Plag, Opx, Mnt, Ilm	39–48 *(43 ± 3)*	43–54 *(45 ± 1)*	n/a	38–41	87–88
M	5.3	3	Plag, Opx, Mnt, Ilm	35–59 *(41 ± 2)*	44–59 *(46 ± 3)*	n/a	38–40	87–89
N	4.9	3	Plag, Opx, Mnt, Ilm	38–86 *(42 ± 5)*	43–53 *(45 ± 2)*	n/a	39–41	87–89
O	4.8	4	Plag, Opx, Mnt, Ilm	34–52 *(43 ± 3)*	42–58 *(44 ± 2)*	n/a	37–41	87–89
P	4.8	3*	Plag, Opx, Mnt, Ilm	39–55 *(41 ± 3)*	41–52 *(44 ± 2)*	n/a	38–41	87–89
Q	4.6	2.5*	Plag, Opx, Mnt, Ilm	39–64 *(40 ± 1)*	41–54 *(45 ± 1)*	n/a	40–42	88–89
R	4.5	3*	Plag, Opx, Mnt, Ilm	37–54 *(41 ± 4)*	39–52 *(44 ± 1)*	n/a	40–41	87–88
S	3.6	4.5	Plag, Opx, Mnt, Ilm	38–45 *(42 ± 2)*	42–53 *(44 ± 1)*	n/a	41–42	88–89
$\mathrm{S_{greys}}$	3.6	4.5	Plag, Opx, Mnt, Ilm, Cpx, Amp, Ol	38–80	43–57	61–75	37–42	74–89
$\mathrm{S_{mafic}}$	3.6	n/d	Plag, Opx, Ol, Cpx, Mnt, Ilm, Amp	42–95	56–72	52–84	36–38	74–77
T	3.2	5.5*	Plag, Opx, Mnt, Ilm	35–54 *(40 ± 2)*	39–52 *(44 ± 2)*	n/a	41–42	88–89
U	2.9	6	Plag, Opx, Mnt, Ilm	33–50 *(36 ± 2)*	41–50 *(43 ± 2)*	n/a	41–43	89–90
V	2.8	7	Plag, Opx, Mnt, Ilm	32–52 *(36 ± 4)*	38–61 *(41 ± 3)*	n/a	41–43	89–91
W	2.8	5.5	Plag, Opx, Mnt, Ilm	31–51 *(39 ± 5)*	37–55 (43 ± 3)	n/a	40–43	89–91
Subgroup 3 rhyolites								
X	2.2	4	Plag, Opx, Mnt, Ilm	39–61 *(44 ± 3)*	43–59 *(50 ± 1)*	n/a	37–38	86–87
Y1	1.8	3	Plag, Opx, Mnt, Ilm	39–51 *(45 ± 2)*	43–59 *(50 ± 1)*	n/a	38–39	86–88
Y3	1.8	2.5	Plag, Opx, Mnt, Ilm	39–61 *(45 ± 3)*	44–57 *(50 ± 2)*	n/a	38–40	85–89
Y6	1.8	2.5	Plag, Opx, Mnt, Ilm	39–69 *(46 ± 4)*	43–68 *(50 ± 2)*	n/a	37–38	86–88
Z	1.8	5.5	Plag, Opx, Mnt, Ilm	39–81 *(46 ± 4)*	45–61 *(51 ± 2)*	n/a	40–42	88–89
$\mathrm{Z_{mafic}}$	1.8	n/d	Plag, Opx, Olivine, Mnt	38–99	46–74	n/a	n/a	n/a

Mineral contents calculated by heavy liquid glass and mineral separation. Mineral compositions determined by electron probe microanalyser (EPMA). For plagioclase feldspar (Plag), anorthite content (An) = 100*(Ca/Ca + Na + K). For orthopyroxene (Opx) and clinopyroxene (Cpx), magnesium number (Mg#) = 100*(Mg/Mg + Fe + Mn). All amphibole (Amp) is magnesiohornblende. Magnetite (Mnt) and Ilmenite (Ilm) compositions calculated by methods of Lepage (2003). Mineral compositional ranges include all EPMA analyses of multiple zones within multiple crystals (see Online Resource 3 for raw data). Crystal rim compositions (shown in *italics*) on euhedral shaped grains are inferred to represent the final stages of crystal growth and hence equilibrium composition with the final melt. Crystal concentrations marked with * are from coarse ash or fine lapilli samples and therefore are not deemed to be fully representative of the magma (see text for discussion)

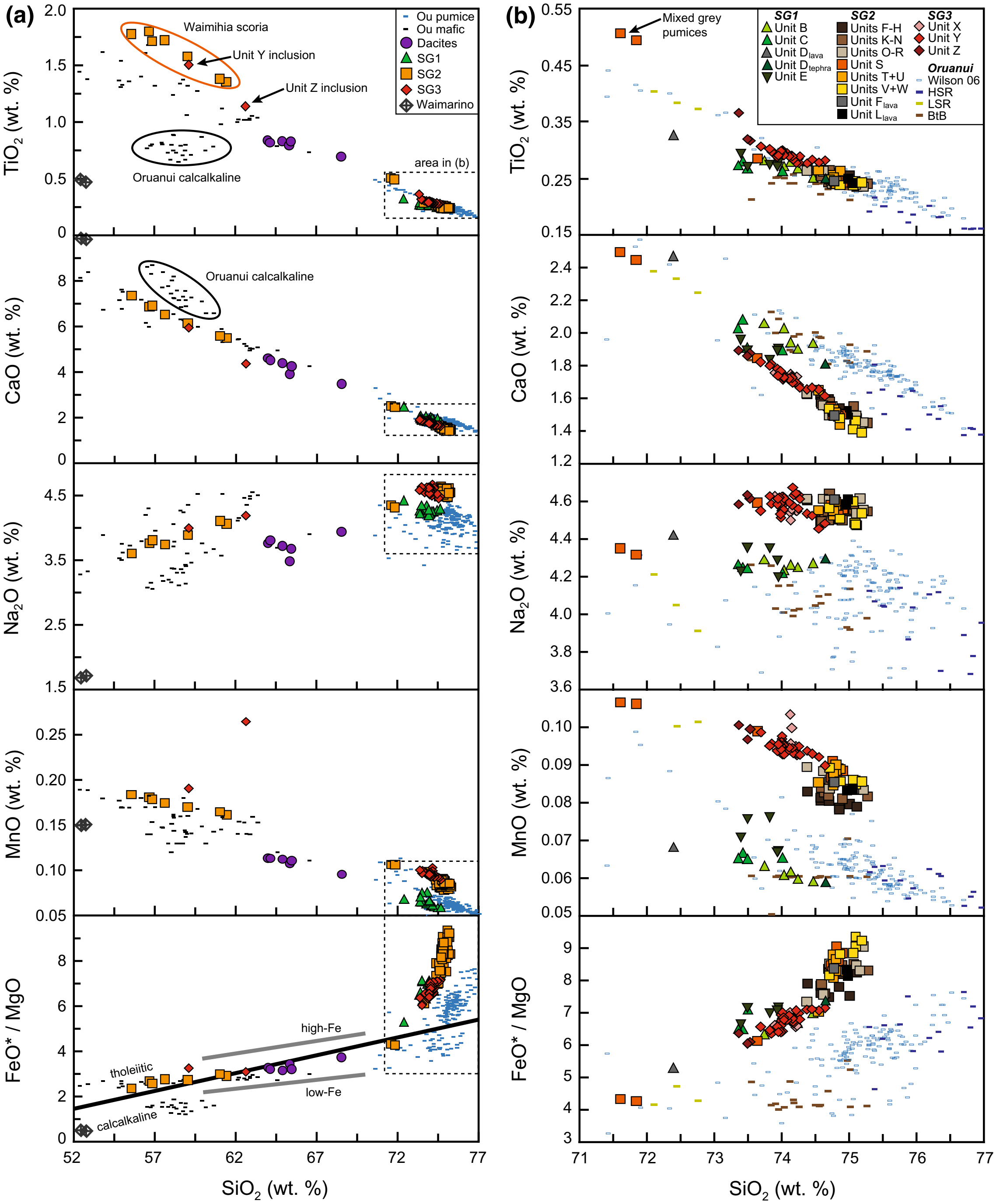

Fig. 2 Selected major-element variation diagrams for eruptive material from Taupo and Waimarino. **a** Full compositional range of pumice, lava and scoria. Oruanui data are from Wilson et al. (2006) and Allan (2013). The *grey boundaries* on the FeO*/MgO plot are from Arculus (2003) and the *black line* marks the discriminant boundary from Miyashiro (1974). **b** Enlargement of regions marked by *dashed boxes* in (**a**) with *symbols* representing eruptions by subgroup. Oruanui pumice types were identified by Allan (2013); *HSR* high-silica rhyolite, *LSR* low-silica rhyolite, *BtB* biotite bearing. All values are recalculated based on oxide totals normalised to 100 %. See Online Resource 1 for raw data, original totals and standards

and the highest Rb/Sr ratios, indicating they are the most evolved compositions in the post-Oruanui sequence. The SG2 to SG3 transition then marks the onset of an opposite trend with an increase in concentrations of most compatible elements and significantly lower Rb/Sr ratios (Fig. 4; Table 3).

Table 3 Representative major- and trace-element compositions of post-Oruanui eruptive units

	Unit										
	Ψ	Ω	A	B1	C	D (L)	D (t)	E3	F (L)	F (t)	G
Sample	P2163A	P2112A	P2147	P2116C	P2142A	R837	P2144	P2148E	P2256	P2256A	P2115A
Age BP	20,500	18,800	17,000	11,800	11,400	11,380	11,380	9950	7050	7050	6650
Major elements (wt%)											
SiO_2	64.00	64.89	68.55	74.24	73.42	72.39	74.65	73.94	74.78	74.86	74.58
TiO_2	0.84	0.83	0.70	0.27	0.28	0.33	0.25	0.27	0.24	0.26	0.26
Al_2O_3	16.77	16.18	14.86	13.67	14.26	14.34	13.47	14.01	13.24	13.30	13.50
Fe_2O_3	6.34	6.20	4.87	2.41	2.53	2.77	2.27	2.45	2.37	2.26	2.37
MnO	0.113	0.112	0.096	0.060	0.067	0.068	0.059	0.067	0.085	0.079	0.081
MgO	1.74	1.78	1.18	0.32	0.35	0.47	0.28	0.31	0.25	0.26	0.28
CaO	4.60	4.38	3.46	1.90	2.08	2.47	1.81	1.89	1.49	1.54	1.62
Na_2O	3.76	3.72	3.94	4.25	4.25	4.42	4.30	4.28	4.61	4.56	4.49
K_2O	1.74	1.81	2.21	2.84	2.72	2.67	2.87	2.74	2.86	2.85	2.77
P_2O_5	0.089	0.095	0.140	0.041	0.045	0.071	0.037	0.039	0.063	0.031	0.041
LOI	2.98	3.01	3.07	3.38	3.71	0.7	2.71	3.56	0.33	1.3	3.28
Total	100.25	100.35	100.46	99.53	100.18	100.23	100.19	99.72	100.11	99.42	100.66
Trace elements (ppm)											
Li	23.4	24.7	28.0	32.7	36.6	40.5	35.5	48.3	22.1	43.3	32.5
Sc	20.8	18.1	14.6	9.0	10.2	9.8	9.3	10.3	11.4	10.7	11.0
V	127	125	76.7	9.38	11.6	16.4	8.76	7.83	2.18	2.98	3.12
Cr	11.3	9.82	9.62	7.67	4.16	6.74	7.53	26.1	9.20	2.23	4.64
Ni	10.9	10.0	8.71	8.49	7.77	4.63	7.27	1.00	9.74	0.16	8.72
Cu	3.40	5.09	3.43	2.07	2.18	3.07	2.07	1.76	1.75	1.24	1.63
Zn	82	87	74	53	58	61	55	57	71	67	69
Ga	20.7	18.6	17.8	15.8	17.3	16.4	17.2	17.0	17.2	17.7	16.6
Rb	66	63	76	98	106	95	112	106	102	109	102
Sr	258	237	196	135	159	169	142	154	131	141	145
Y	24.5	21.7	27.7	29.5	32.3	28.6	31.3	32.9	32.6	33.0	33.5
Zr	202	180	218	190	205	195	211	216	213	226	216
Nb	7.79	7.66	8.71	8.20	9.31	8.71	9.10	8.46	9.83	9.25	9.89
Cs	2.89	3.00	3.64	4.31	4.50	4.28	4.53	5.53	4.11	5.65	4.12
Ba	466	432	490	598	671	585	654	646	641	648	622
La	18.6	16.8	20.3	22.2	24.4	22.8	25.4	25.1	24.9	26.0	25.0
Ce	45.4	42.1	43.1	47.4	53.1	49.2	53.8	54.3	54.1	54.0	56.2
Pr	4.55	4.22	5.26	5.64	6.28	5.83	6.33	6.31	6.43	6.53	6.50
Nd	18.3	17.2	21.1	21.4	23.3	23.3	24.5	24.5	24.8	25.4	26.0
Sm	4.19	3.82	4.62	4.74	5.00	4.84	5.21	5.43	5.55	5.67	5.56
Eu	1.17	1.09	1.13	0.99	1.17	1.18	1.11	1.10	1.28	1.28	1.26
Gd	4.27	3.83	4.98	4.83	5.37	5.03	5.37	5.92	5.59	5.79	5.72
Tb	0.66	0.58	0.77	0.77	0.81	0.82	0.86	0.86	0.83	0.89	0.92
Dy	4.27	3.79	4.78	4.91	5.37	5.08	5.30	5.46	5.77	5.55	5.68
Ho	0.88	0.78	0.93	0.98	1.13	1.07	1.10	1.17	1.09	1.16	1.16
Er	2.56	2.41	2.78	3.21	3.33	3.20	3.37	3.38	3.34	3.41	3.62
Tm	0.40	0.34	0.44	0.48	0.50	0.48	0.51	0.51	0.53	0.52	0.54
Yb	2.62	2.42	3.06	3.07	3.23	3.02	3.33	3.52	3.56	3.48	3.38
Lu	0.41	0.37	0.44	0.47	0.50	0.48	0.52	0.55	0.52	0.52	0.56
Hf	5.38	4.63	5.53	5.36	5.71	5.25	5.67	6.04	5.77	6.06	5.86
Pb	10.8	11.7	21.7	15.4	16.4	12.0	15.5	18.6	12.5	21.2	17.4

Table 3 continued

	Unit										
	Ψ	Ω	A	B1	C	D (L)	D (t)	E3	F (L)	F (t)	G
Th	8.1	7.1	7.7	10.3	11.0	10.9	11.2	11.7	10.7	11.1	11.1
U	1.62	1.57	1.85	2.38	2.52	2.39	2.65	2.68	2.53	2.51	2.54
Rb/Sr	0.26	0.26	0.39	0.73	0.67	0.56	0.79	0.69	0.78	0.77	0.70
Eu/Eu*	0.84	0.87	0.72	0.63	0.69	0.73	0.64	0.59	0.70	0.68	0.68

	Unit										
	H	K	L (L)	L (t)	M	N	O	P	Q	R	S
Sample	P2132	P2206A	R602	P2137	P2171	P2170	P2169A	P2168A	P2136	P2114	P2209
Age BP	6050	5350	5300	5300	5250	4850	4800	4750	4550	4450	3550
Major elements (wt%)											
SiO_2	75.12	74.70	75.01	74.71	75.28	75.07	74.38	75.11	75.22	74.71	74.82
TiO_2	0.23	0.24	0.25	0.26	0.24	0.24	0.26	0.24	0.23	0.25	0.24
Al_2O_3	13.27	13.55	13.11	13.21	13.03	13.13	13.47	13.13	13.07	13.40	13.29
Fe_2O_3	2.24	2.26	2.30	2.40	2.23	2.27	2.42	2.31	2.26	2.34	2.35
MnO	0.079	0.082	0.084	0.086	0.082	0.084	0.089	0.083	0.083	0.084	0.087
MgO	0.24	0.24	0.25	0.26	0.24	0.24	0.30	0.24	0.22	0.25	0.23
CaO	1.48	1.55	1.49	1.58	1.45	1.55	1.63	1.49	1.45	1.50	1.50
Na_2O	4.47	4.50	4.61	4.64	4.55	4.56	4.61	4.54	4.55	4.61	4.55
K_2O	2.83	2.82	2.85	2.81	2.87	2.81	2.80	2.83	2.87	2.82	2.88
P2O5	0.035	0.048	0.041	0.034	0.032	0.036	0.044	0.033	0.031	0.041	0.044
LOI	3.42	3.23	0.45	1.1	2.67	2.22	2.26	1.91	1.4	2.75	2.87
Total	100.38	100.05	99.87	100.63	100.28	100.65	99.95	100.44	100.30	99.71	99.75
Trace elements (ppm)											
Li	34.1	40.2	41.2	39.8	43.7	40.1	44.3	36.1	35.7	40.0	38.9
Sc	10.3	10.7	11.0	11.6	11.0	10.8	11.7	10.8	10.9	11.0	11.0
V	2.35	2.26	1.91	2.17	1.83	1.74	2.45	1.82	1.54	2.07	1.79
Cr	3.55	3.69	2.56	0.25	2.35	4.34	3.19	0.32	0.31	1.85	5.48
Ni	0.31	0.75	0.14	0.06	0.24	0.20	0.37	0.45	0.23	0.29	0.22
Cu	1.25	1.52	1.13	1.05	1.34	1.24	1.37	1.15	1.17	1.84	1.36
Zn	62	68	68	72	69	67	76	68	69	68	70
Ga	15.7	16.8	16.1	17.6	17.2	16.0	16.7	16.2	16.0	16.5	16.9
Rb	101	105	104	107	110	104	108	106	103	102	104
Sr	127	140	130	147	133	138	156	136	125	135	135
Y	32.2	32.9	33.2	33.6	34.5	32.6	34.8	33.3	32.4	33.2	32.7
Zr	203	212	213	225	221	213	226	222	218	223	220
Nb	7.96	9.08	9.07	11.99	9.23	8.92	8.90	8.46	8.40	8.46	11.18
Cs	5.41	5.58	5.28	4.95	5.71	5.05	5.00	5.54	5.39	5.19	4.96
Ba	620	631	633	629	665	602	658	642	622	630	620
La	24.7	25.6	25.6	25.3	26.6	24.6	26.8	25.7	25.4	25.5	25.1
Ce	52.7	53.0	54.7	53.1	56.1	51.4	57.1	55.4	54.5	54.6	55.7
Pr	6.25	6.57	6.53	6.53	6.81	6.04	6.86	6.56	6.42	6.51	6.65
Nd	24.5	25.3	25.6	25.7	25.9	24.4	26.3	25.1	24.6	25.6	26.1
Sm	5.28	5.59	5.35	5.38	5.64	5.25	5.77	5.53	5.43	5.61	5.61
Eu	1.19	1.23	1.24	1.27	1.29	1.26	1.35	1.27	1.21	1.29	1.22
Gd	5.72	6.06	5.59	5.74	6.15	5.53	6.32	6.36	5.88	6.24	5.83
Tb	0.84	0.87	0.86	0.86	0.90	0.83	0.93	0.89	0.86	0.91	0.87
Dy	5.30	5.59	5.56	5.57	5.77	5.11	5.77	5.60	5.47	5.67	5.47

Table 3 continued

	Unit										
	H	K	L (L)	L (t)	M	N	O	P	Q	R	S
Ho	1.13	1.13	1.13	1.15	1.19	1.06	1.23	1.19	1.15	1.19	1.16
Er	3.36	3.30	3.46	3.45	3.51	3.20	3.57	3.49	3.34	3.46	3.38
Tm	0.51	0.51	0.52	0.51	0.54	0.48	0.54	0.53	0.51	0.53	0.51
Yb	3.38	3.45	3.38	3.44	3.62	3.18	3.59	3.50	3.41	3.51	3.57
Lu	0.52	0.51	0.52	0.52	0.53	0.48	0.55	0.53	0.52	0.53	0.51
Hf	5.58	5.54	5.80	5.92	5.88	5.32	6.03	5.95	5.79	6.05	5.91
Pb	16.9	20.6	20.6	24.1	21.5	19.4	19.3	17.2	16.6	17.5	23.4
Th	10.8	11.0	10.8	10.7	11.5	9.9	11.2	10.9	10.6	10.9	10.7
U	2.41	2.46	2.49	2.43	2.57	2.23	2.48	2.52	2.42	2.48	2.39
Rb/Sr	0.79	0.75	0.80	0.73	0.83	0.75	0.69	0.78	0.82	0.76	0.77
Eu/Eu*	0.66	0.65	0.69	0.70	0.67	0.71	0.68	0.68	0.66	0.67	0.65

	Unit										
	S mafic	T	U	V	W	X	Y1	Y3	Y7	Z	Wai
Sample	P2202A	P2149A	P2150A	P2161A	P2155B	P2157A	P2119	P2293	P2287	P2173A	R834
Age BP	3550	3200	2850	2800	2750	2150	1718	1718	1718	~1700	<25,400
Major elements (wt%)											
SiO$_2$	55.57	74.77	74.76	74.71	75.06	74.21	74.38	74.02	73.99	73.53	52.75
TiO$_2$	1.78	0.26	0.25	0.25	0.24	0.28	0.28	0.29	0.29	0.32	0.47
Al$_2$O$_3$	15.99	13.35	13.34	13.32	13.11	13.48	13.45	13.57	13.53	13.67	12.69
Fe$_2$O$_3$	9.90	2.36	2.34	2.35	2.28	2.51	2.43	2.51	2.55	2.67	8.95
MnO	0.184	0.086	0.085	0.089	0.086	0.095	0.094	0.094	0.095	0.099	0.151
MgO	3.79	0.25	0.24	0.26	0.23	0.34	0.31	0.34	0.35	0.39	12.92
CaO	7.34	1.52	1.52	1.54	1.41	1.73	1.65	1.74	1.74	1.87	9.82
Na$_2$O	3.60	4.53	4.55	4.56	4.60	4.55	4.53	4.63	4.59	4.62	1.71
K$_2$O	1.04	2.85	2.88	2.88	2.94	2.76	2.83	2.76	2.80	2.75	0.44
P$_2$O$_5$	0.795	0.036	0.038	0.043	0.042	0.053	0.052	0.056	0.061	0.080	0.078
LOI	1.01	2.15	2.34	2.6	0.42	2.71	2.04	2.88	3.29	0.82	0.14
Total	99.02	99.32	98.90	99.14	99.00	99.56	99.20	99.81	99.79	99.49	99.96
Trace elements (ppm)											
Li	15.3	44.2	42.3	33.6	33.7	43.2	40.8	43.1	35.8	33.7	8.6
Sc	31.1	11.5	11.5	10.2	10.1	11.3	11.4	11.6	11.7	11.7	34.2
V	154	2.28	2.17	1.43	1.73	1.72	2.01	2.18	3.41	3.73	203
Cr	13.9	2.30	1.90	2.34	2.69	1.96	1.92	3.40	16.5	4.63	745
Ni	10.3	0.15	0.12	0.20	0.26	0.17	0.19	0.13	0.22	0.32	302
Cu	2.49	1.76	1.23	1.03	1.47	1.58	1.56	1.09	1.45	1.16	39.2
Zn	104	71	72	65	63	72	72	75	74	74	70
Ga	20.4	17.1	16.8	15.1	15.2	16.9	16.8	17.6	16.7	16.6	13.6
Rb	33	108	105	96	100	104	103	104	101	94	11
Sr	342	146	142	122	121	173	164	174	168	163	328
Y	24.9	34.5	34.6	31.0	31.5	34.7	34.3	34.9	33.7	31.5	11.4
Zr	96	229	210	189	188	232	231	232	223	209	39
Nb	5.33	9.84	9.75	7.72	7.95	9.73	12.65	4.02	12.47	7.95	2.24
Cs	1.67	5.12	5.19	5.05	5.23	5.26	4.85	4.08	4.84	4.91	0.62
Ba	253	658	650	571	588	637	621	611	615	578	106
La	13.8	26.4	26.9	23.8	24.3	27.0	25.9	25.9	26.1	24.0	5.8
Ce	32.3	57.2	56.8	51.2	52.7	58.2	55.0	55.7	55.3	52.4	11.9

Table 3 continued

	Unit										
	S mafic	T	U	V	W	X	Y1	Y3	Y7	Z	Wai
Pr	4.32	6.70	6.76	6.02	6.16	7.16	6.54	6.55	6.70	6.30	1.53
Nd	19.3	27.0	26.2	23.4	23.9	27.1	26.1	26.7	26.4	24.6	6.5
Sm	4.68	5.76	5.73	5.06	5.20	6.02	5.46	5.90	5.58	5.36	1.56
Eu	1.58	1.30	1.32	1.14	1.17	1.38	1.26	1.33	1.35	1.31	0.51
Gd	4.81	6.28	6.01	5.48	5.57	6.51	5.75	5.93	5.92	5.94	1.76
Tb	0.74	0.92	0.92	0.81	0.84	0.96	0.87	0.94	0.91	0.87	0.29
Dy	4.49	5.68	5.90	5.15	5.21	6.05	5.55	5.88	5.75	5.36	1.96
Ho	0.91	1.18	1.24	1.08	1.11	1.26	1.16	1.24	1.19	1.13	0.43
Er	2.54	3.59	3.60	3.14	3.27	3.60	3.55	3.74	3.48	3.30	1.25
Tm	0.37	0.55	0.54	0.47	0.50	0.57	0.52	0.55	0.53	0.51	0.19
Yb	2.27	3.64	3.57	3.12	3.26	3.81	3.40	3.70	3.42	3.32	1.23
Lu	0.34	0.54	0.55	0.48	0.49	0.56	0.52	0.58	0.52	0.50	0.19
Hf	2.64	6.17	5.82	4.97	5.17	6.32	5.99	6.26	6.02	5.56	1.20
Pb	9.7	22.1	22.7	15.5	16.6	23.1	21.5	21.1	22.4	16.0	3.0
Th	3.8	11.4	11.2	9.6	10.2	11.2	10.7	11.0	10.8	9.8	1.6
U	0.84	2.57	2.50	2.18	2.27	2.60	2.38	2.53	2.36	2.20	0.40
Rb/Sr	0.10	0.74	0.74	0.79	0.82	0.60	0.63	0.60	0.60	0.58	0.03
Eu/Eu*	1.02	0.66	0.69	0.66	0.66	0.67	0.69	0.69	0.72	0.71	0.94

Oxide abundances normalised to 100 % on a volatile-free basis, with original analytical totals and LOI given. Eruption ages are given in years before present (BP) and sourced from Wilson (1993) and Hogg et al. (2012). Units denoted with (L) are lavas and (t) are tephras for the corresponding unit. Wai is Waimarino basalt. See Online Resource 1 and 2 for raw data, original totals and standards

Glass and melt-inclusion compositions

Crystals from the dacite units contain abundant pristine melt inclusions up to 100 µm, with compositions between ~68 and 76 wt% SiO_2 (Fig. 5a). In contrast, glass selvedges on the corresponding crystals have a relatively narrow range of 72–75 wt% SiO_2. Melt inclusions in SG1 crystals are less common and typically much smaller (10–30 µm), but overlap in composition with dacite glass selvedges (<75 wt% SiO_2) and extend towards more evolved SG1 glass selvedge compositions (~75–77.5 wt% SiO_2) (Fig. 5b). SG1 glass compositions are similar to those of Oruanui plagioclase melt inclusions (Allan 2013), but are generally not as evolved as the Oruanui HSR pumice glass. SG2 melt inclusions and glass selvedges have a comparatively narrow range of compositions, and melt inclusions with <75 wt% SiO_2 are relatively rare (Fig. 6a, b). There are no measureable differences in glass chemistry within the SG2 rhyolites until the latest units (U, V and W) which have the highest SiO_2 contents of all post-Oruanui eruption glasses. SG3 units X and Y, in contrast, show a decrease in glass selvedge SiO_2 to ~75 wt%, but with melt-inclusion compositions that overlap with earlier units. Eruption Z glass forms a distinct high-SiO_2 geochemical field, but this is considered to reflect late-stage plagioclase and pyroxene microlite growth during lava degassing, resulting in interstitial melt with higher SiO_2 (e.g. Lipman 1965).

Glass trace-element compositions were analysed in parallel with whole-rock samples to assess the effects of differing crystal contents and phases between eruption groups and to investigate the evolution of the melt phase through time (Fig. 4). Dacite glass separates are significantly more evolved than their corresponding whole-rock compositions but are identical for the three eruption units (Ψ, Ω, A). Glass compositional variations from the rhyolite subgroups (SG1–3) generally parallel trends seen in whole-rock chemistry. The major exception is for SG1 rhyolites where the glass Sr concentration is significantly lower than the whole rock, likely due to high Sr abundances in plagioclase. As a result, the whole-rock and glass Rb/Sr trends from SG1 to SG2 rhyolites show opposite trends (Fig. 4).

Crystal chemistry and compositional zoning

Crystals in the dacites display a range of zoning from strongly resorbed with mottled cores followed by normal zoning, to completely unzoned (Fig. 7). However, crystal rims almost always converge towards a common and relatively narrow compositional range (Table 2). The composition of strongly zoned cores and interior zones of the dacite crystals overlap with high-enstatite (En) clinopyroxene (up

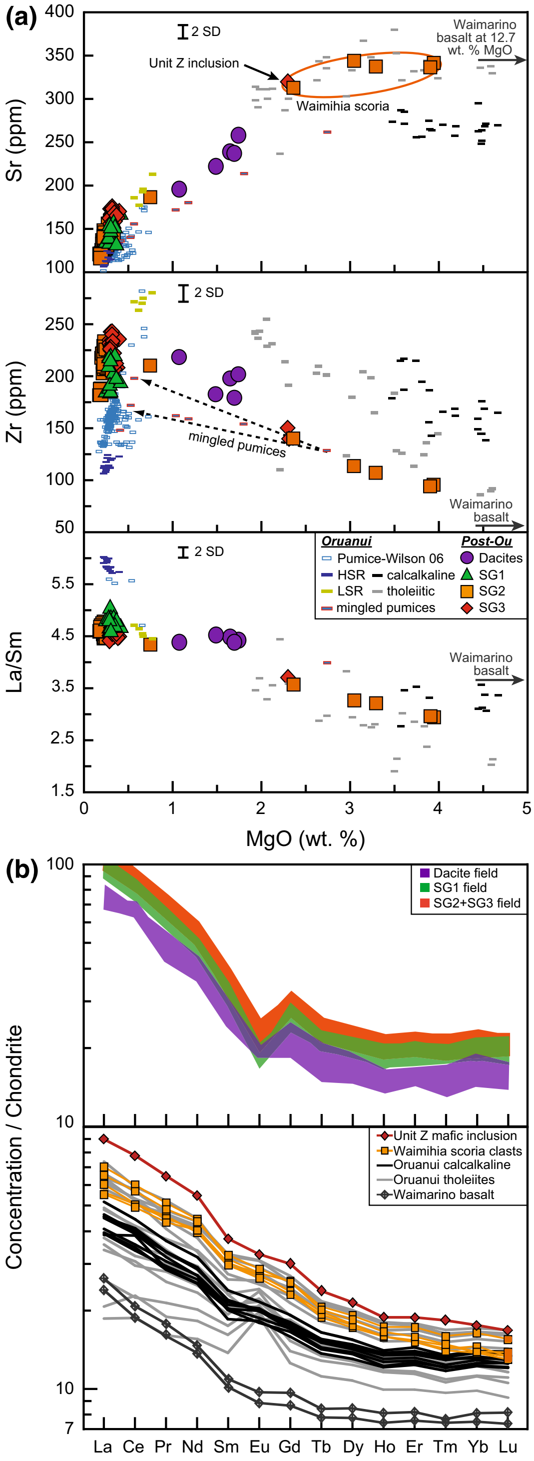

Fig. 3 Trace-element concentrations for Oruanui and post-Oruanui pumices and mafic clasts. **a** Selected trace-element variation diagrams versus MgO. Oruanui data are from Wilson et al. (2006) and Allan (2013). **b** REE patterns normalised to chondrite (Palme and Beer 1993). Oruanui tholeiitic and calcalkaline mafic clasts (*bottom*) are from Allan (2013). See Online Resource 2 for raw data

to En_{49}: Fig. 8a), orthopyroxene (up to En_{70}: Fig. 9a, b) and high-anorthite (An) plagioclase cores (up to An_{90}: Fig. 10a, b) from the Oruanui mafic clasts (Allan 2013). In comparison, the crystals from SG1 units B–D typically display less pronounced compositional zoning with textures dominated by normal and oscillatory zoning (Fig. 7). Pyroxene core compositions from units B–D largely overlap with the compositional field of dacite crystal rims (Figs. 8b, 9c) and orthopyroxenes continue the unique low-MnO compositional trend that is distinctive from Oruanui orthopyroxenes (Allan 2013). Unit E pyroxene compositions tend to occur as two subgroups with an additional higher-MnO population (Figs. 8c, 9d). SG1 plagioclases have a wide overall range of compositions with common high-An cores and interior zones (up to An_{85}), overgrown by low-An rims clustered at $<An_{50}$ with only a few crystals displaying reverse zoning (Figs. 7c, 10c, d).

Strong zonation is much less common in SG2 crystals, with many grains showing either minor normal zoning, oscillatory zoning or no zoning (Figs. 7, 9e,f, 10e,f; Table 2). Crystal rim compositions are broadly similar to those observed in SG1 rhyolites with plagioclase having slightly lower An values. Unit S mafic clasts show a wide range of crystal compositions, with rims and interior zones overlapping with dacite crystal compositions (Figs. 8d, 9f, 10f). A subset of plagioclase cores and unzoned crystals in Unit S mafic clasts are $>An_{90}$ (Fig. 10f), and olivine crystals are dominantly unzoned and Fo_{83-85} (Online Resource 3). Notably, younger SG2 units following Unit S have the most evolved crystal compositions in the post-Oruanui sequence, with plagioclase as low as An_{35} and orthopyroxene as low as En_{37} (Table 2; Figs. 9f, 10f). The SG2 orthopyroxene compositions follow a distinctly different trend to those in SG1, having higher concentrations of MnO at any given En concentration (Fig. 9e, f). SG3 crystals display contrasting zonation to those in SG2, with both plagioclase and orthopyroxene dominantly displaying reverse zoning, with a minor population of normally zoned or unzoned crystals (Fig. 7). These patterns are reflected in the crystal compositions, with cores derived from either a low-An, low-En reversely zoned population of crystals or a high-An, high-En normally zoned population (Figs. 9g, h, 10g, h). Crystal rims have distinctly higher-An ($\sim An_{50}$) and higher-En ($\sim En_{45}$) than SG2 or SG1 (Table 2). Eruption Z mafic inclusions contain crystals of a primitive origin with unzoned plagioclase up to An_{98} (Fig. 10h) and olivine up to Fo_{90} (Online Resource 3).

Fe–Ti oxide compositions change systematically between the dacites and rhyolites and also within and between the rhyolite subgroups (Fig. 11a). Magnetite and

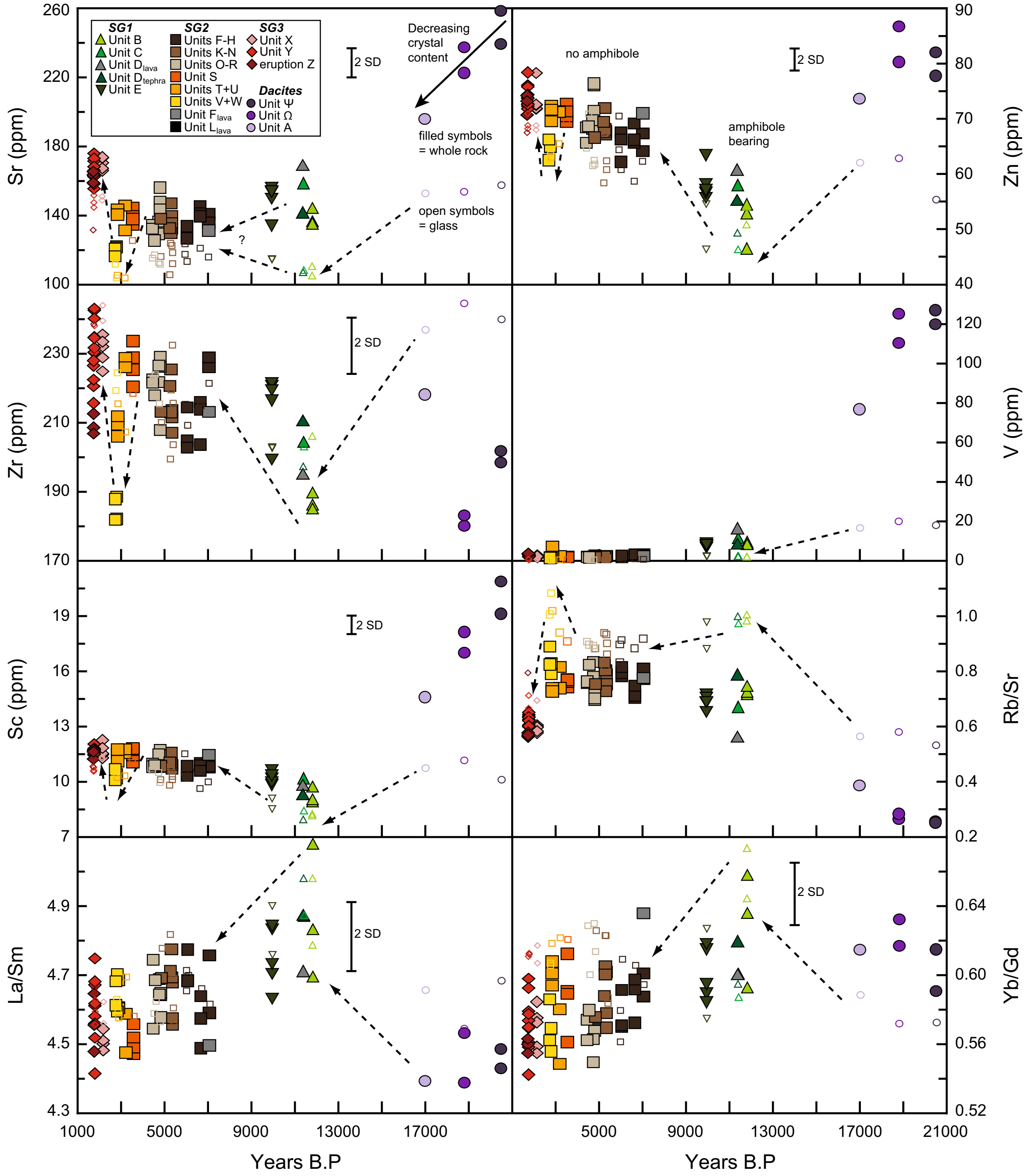

Fig. 4 Trace-element compositions of bulk pumices and lavas (*large filled symbols*) compared to pure glass separates (*small open symbols*) from the post-Oruanui eruptions versus time. 2 SD analytical uncertainties are from repeated analyses of a Taupo ignimbrite secondary standard, but not shown for V or Rb/Sr as it is approximately the size of the symbols. *Dashed arrows* indicate the inferred direction of melt evolution with crystallisation or dissolution of the observed mineral phases through time. See text for discussion and Online Resource 2 for raw data and standards

ilmenite compositions mirror the trends seen in orthopyroxene where there is an increase in MnO between the SG1 and SG2/SG3 rhyolites. Accompanying such trends, magnetite and ilmenite MgO concentrations decrease significantly from the dacites to the SG1 rhyolites, stay constant throughout most of SG2, and then slowly decrease in the later SG2 eruptions before increasing in SG3. Amphibole (where present) shows a limited compositional range in units B and C, overlapping broadly in its major and trace-element composition with Oruanui amphiboles (Fig. 12). However, amphibole found in trace amounts in units D and E shows a much wider compositional range, similar to those from the Oruanui LSR or mafic clasts, and groundmass amphibole from Unit S mafic clasts. Due to their

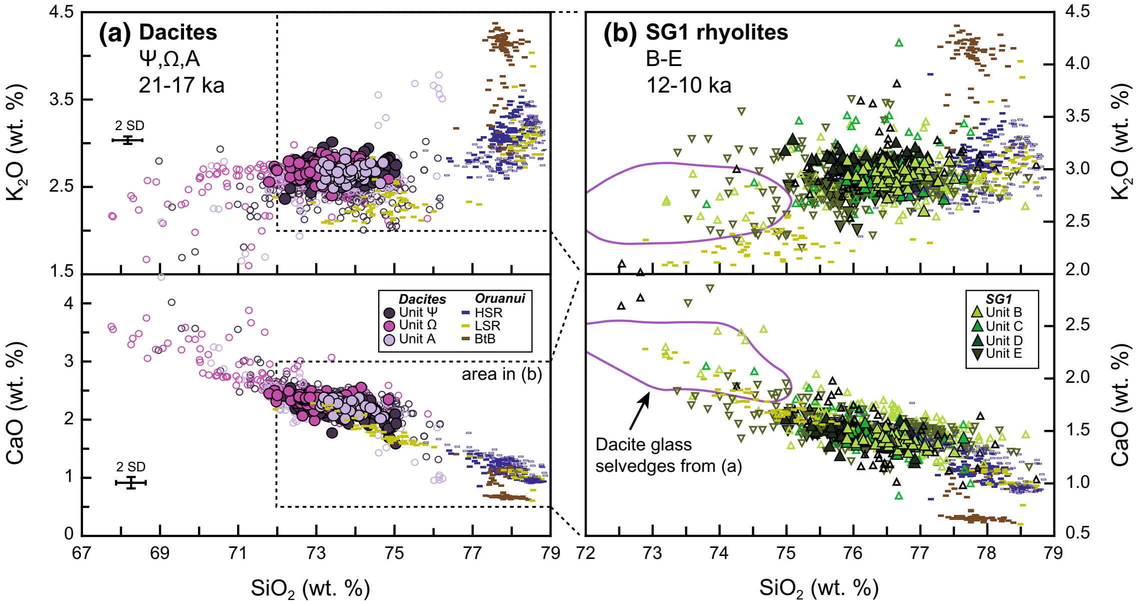

Fig. 5 Major-element variation diagrams showing the compositions of melt inclusions (*open symbols*) and glass selvedges (*filled symbols*) from plagioclase and pyroxenes from **a** dacite units Ψ, Ω and A and **b** SG1 units B–E. Oruanui glass (*filled rectangles*) and melt-inclusion data (*open rectangles*) are from Allan (2013). *Dashed boxes* in (**a**) refer to the enlarged areas shown in (**b**). All data are normalised to 100 % on a volatile-free basis. Raw data and standards are presented in Online Resource 3

scarcity, anhedral appearance and range of compositions, the Unit D and Unit E amphiboles are considered to be xenocrystic.

Intensive parameters

Temperatures

Mineral–mineral and mineral–melt geothermometers have been applied, as appropriate for each eruption (Table 4; Figs. 11, 12, 13). Where available, multiple model calibrations or varied sensitive parameters were used, such as H_2O content of the melt, to provide a full range of realistic estimates. In general, the models provide reasonably consistent temperatures (generally ±30 °C) with several trends immediately identifiable. The most obvious feature is the large increase in model temperatures of >100 °C between the Oruanui HSR magma (Allan 2013) and the post-Oruanui dacites. The inferred magma temperature then drops significantly (by >50 °C) for the post-Oruanui rhyolites of SG1 (Table 4; Fig. 13). Demarcation of temperature trends within the post-Oruanui rhyolites is hampered by the wide range of temperature outputs between the models used, even for different models based on the same crystal phases. For example, the Ghiorso and Evans (2008) Fe–Ti oxide model consistently gives the highest temperature estimates which are 20–40 °C higher than the Sauerzapf et al. (2008) model or any other available mineral–mineral or mineral–melt equilibrium-based model. In this study, we note also that Fe–Ti oxide temperature estimates for the Taupo magmas are sensitive to the EPMA method used. As reported by Evans et al. (2006), use of synthetic-oxide calibrations of Ti (rutile) and Fe (haematite) results in total offsets of TiO_2 by +1 % and FeO of as much as −2 % between natural ilmenites analysed by microprobe versus wet chemical techniques. In our study, similar discrepancies were experienced as we were unable to replicate natural standards when calibrating EPMA analyses using synthetic oxides. Evans et al. (2006) suggest that this may be the result of a problem with the microprobe matrix correction, and therefore, they corrected their experimental data [used to calibrate the Ghiorso and Evans (2008) model] by the observed offset to account for the discrepancy. Interestingly, the issues with Fe–Ti oxide calibration result in temperature discrepancies of 20–30 °C between the two calibration procedures, despite both models resulting in reasonable analytical totals of ~99–101 %. This discrepancy is, however, still within the uncertainty of the Fe–Ti oxide model used (estimated to be on the order of ~50 °C: Ghiorso and Evans 2008) and within the natural variability of the Fe–Ti oxide compositions measured (denoted by ±2 SD values in Table 4).

Despite variations in the model results, relative differences between temperature estimates are consistent and align with the observed variations in mineral compositions

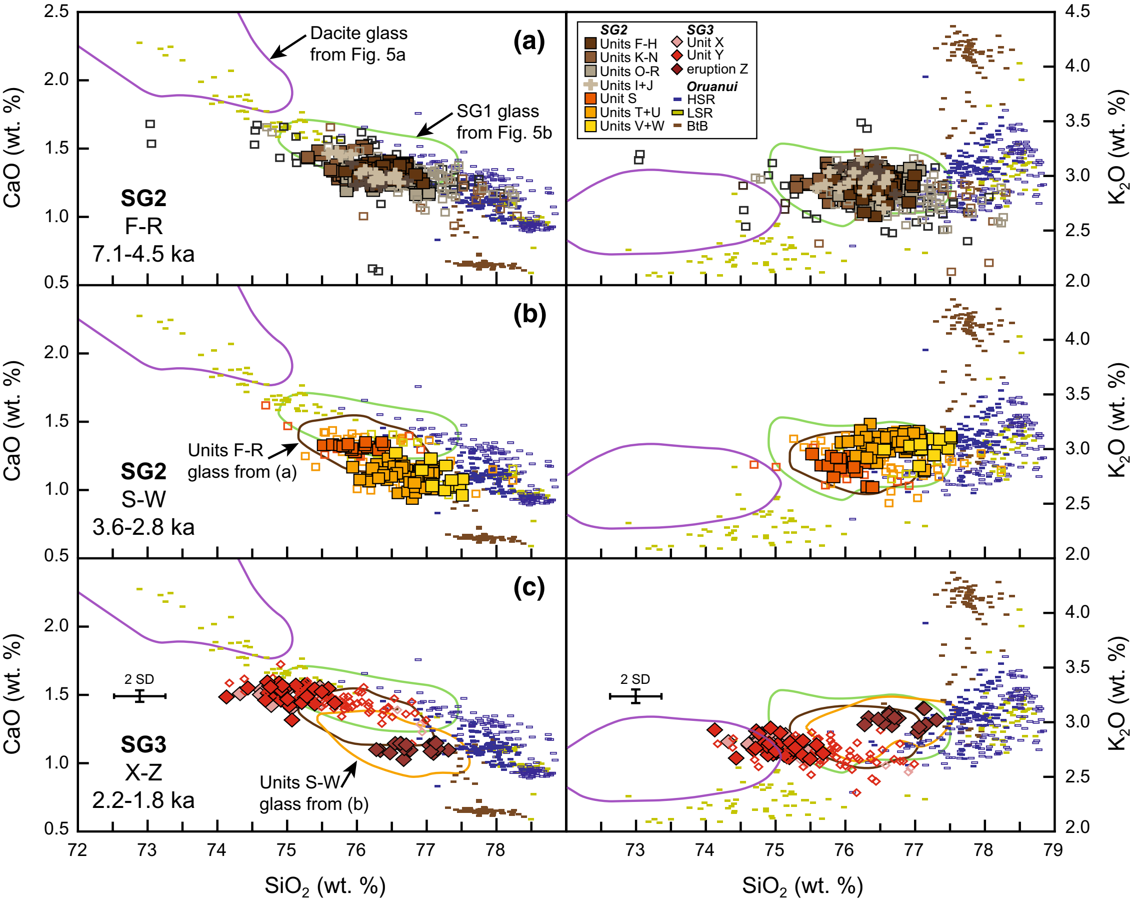

Fig. 6 Major-element variation diagrams showing the compositions of melt inclusions (*open symbols*) and glass selvedges (*filled symbols*) from plagioclase and pyroxenes from **a** SG2 units F–R, **b** SG2 units S–W and **c** SG3 units X, Y and eruption Z. Only matrix glass was analysed for units I and J as they were too fine grained to obtain reliable mineral separates. Oruanui selvedge glass and melt-inclusion data are from Allan (2013). All data are normalised to 100 % on a volatile-free basis and raw data and standards are presented in Online Resource 3

and zonation patterns. Consequently, rather than using absolute temperatures, which are largely subject to the model used and the particular analytical approach, we express the variation between the eruptions as a relative temperature difference (ΔT) relative to the average Oruanui HSR temperatures presented in Allan (2013) using Plag-melt, OPX-melt, amphibole thermometry and recalibrated Fe–Ti oxide temperatures (Fig. 13). For the dacites, ΔT is ~115–140 °C using the Fe–Ti oxide models and ~80–105 °C using the Plag- and OPX-melt models (Fig. 13). The ΔT then drops for the SG1 rhyolites to ~50–65 °C using the Fe–Ti oxide models and ~20–30 °C using the Plag- and OPX-melt models, as well as for the Ridolfi et al. (2010) amphibole thermometer (Fig. 13). The SG2 magmas show two contrasting trends. Using the Fe–Ti oxide models, temperature estimates mildly increase over time to ΔT of ~60–80 °C, but then decrease in units U, V and W. The Plag- and OPX-melt model temperatures for SG2, in contrast, stay constant through time and then ΔT reduces to <20 °C for units U, V and W. These contrasting model results may result from the increase in MnO in SG2 ilmenites, as the Fe–Ti thermometry models are sensitive to the $MnTiO_3$ mol fraction (Ghiorso and Evans 2008). The SG3 rhyolites then show a significant increase in ΔT to ~70–80 °C using the Fe–Ti oxide models and ~40–60 °C using the Plag- and OPX-melt models (Fig. 13), in agreement with trends observed in pumice and mineral chemistry. Temperatures calculated from rare equilibrium Fe–Ti oxide pairs (after Bacon and Hirschmann 1988) from mafic samples return bimodal temperature estimates centred around 980 and 850 °C, with the lower temperature estimates reflecting inherited Fe–Ti oxides from the rhyolites. The higher-temperature estimates are consistent with amphibole and 2-pyroxene thermometry on the same samples (Table 4) and cover a similar range to the Oruanui mafic magmas (Allan 2013).

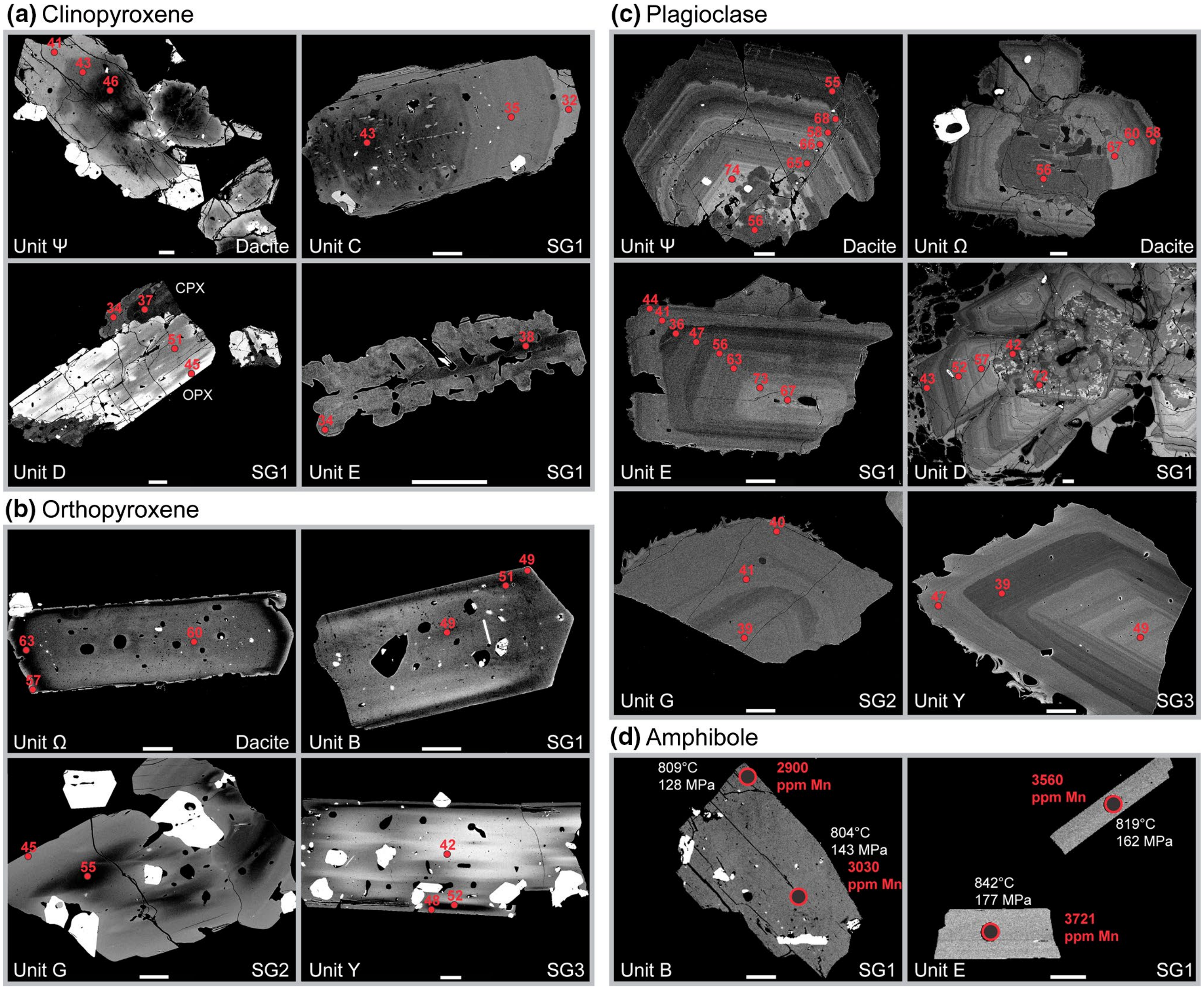

Fig. 7 Representative back-scattered electron (BSE) images and compositions of the main mineral types identified in each of the post-Oruanui subgroups. **a** Clinopyroxene from the dacites and SG1 rhyolites showing variation in enstatite (En) contents (En % = 100*[Mg/(Ca + Mg + ∑Fe)]) through time, and the change from large euhedral grains in the dacites and first SG1 eruptions (units Ψ and C) to small anhedral crystals in the later SG1 eruption (units D and E). *Red dots* denote the approximate probe spot locations with their corresponding compositions. **b** Orthopyroxene from each subunit showing variation in En content and crystal zonation through time. **c** Plagioclase from each subunit showing variation in anorthite (An) content (An % = 100*[Ca/(Ca + Na + K)]) and crystal zonation. **d** Amphibole from the SG1 eruptions showing the change in crystal size and intensive parameters calculated using Ridolfi et al. (2010). *Red circles* represent approximate LA-ICPMS spot locations. *White scale bars* are 100 μm in all images

Oxygen fugacities

Similar to temperature estimates, Fe–Ti oxide oxygen fugacity estimates also vary with the oxybarometry model applied. In particular, the model of Sauerzapf et al. (2008) consistently gives oxygen fugacity estimates that are higher by ~0.4 log units compared to the model of Ghiorso and Evans (2008). In both models, the oxygen fugacity of the dacites is the highest, being well above the NNO buffer (Fig. 11). The rhyolites are more reduced, being either slightly above or on the NNO buffer (Sauerzapf et al. 2008), or slightly below or on the NNO buffer (Ghiorso and Evans 2008). The SG2 rhyolites have the most reduced oxygen fugacities, which drop below the NNO buffer for units T–W. The SG3 rhyolite units X and Y then shift back above the NNO buffer and are the least reduced units observed in the rhyolite subgroups. The oxygen fugacity estimated from the amphibole oxybarometer of Ridolfi et al. (2010) is also typically higher than that observed for the Fe–Ti oxides, by 0.2–0.8 log units. In general, the post-Oruanui rhyolites are more reduced than both the Oruanui HSR and LSR, despite having a similar temperature range to the latter.

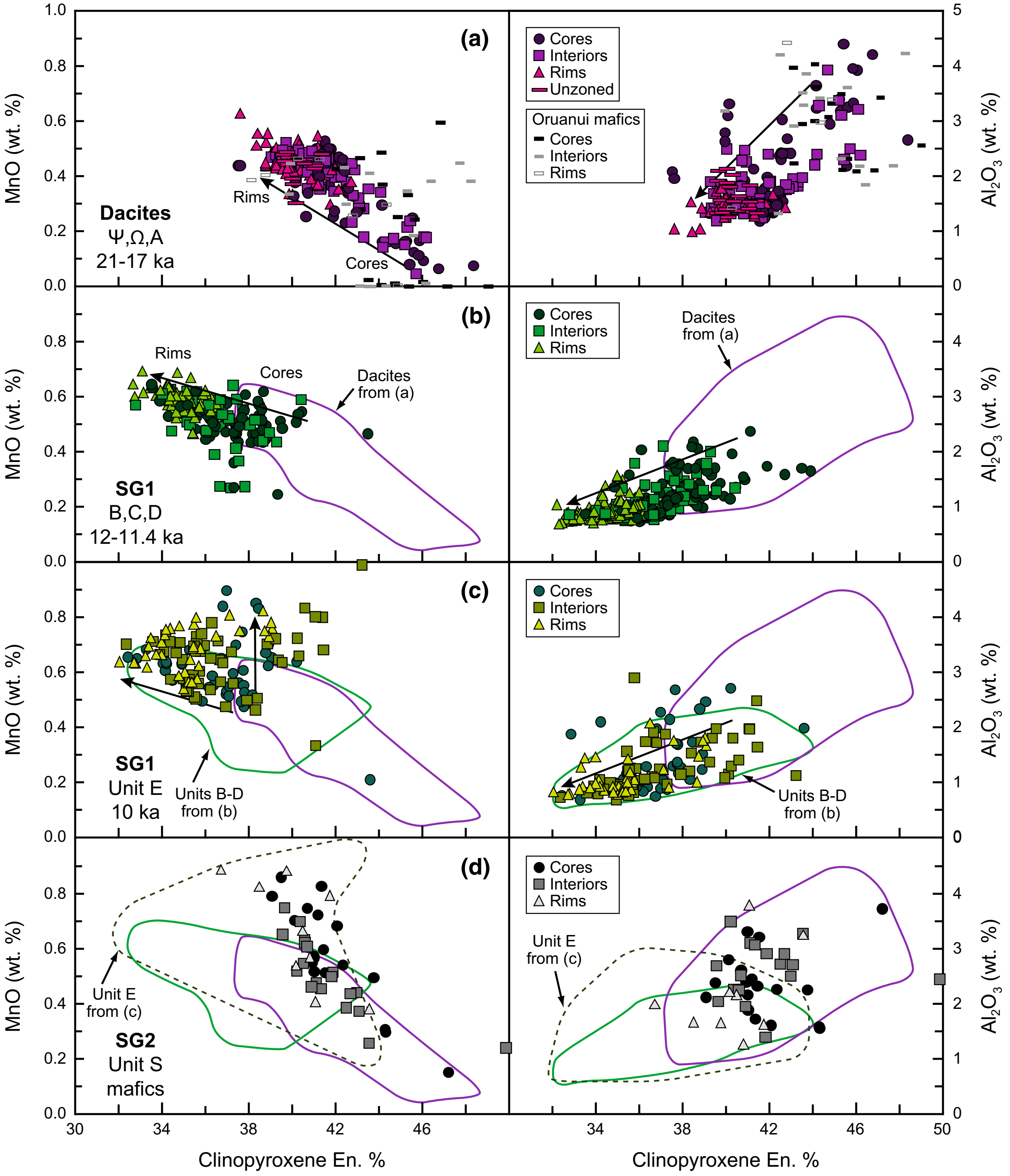

Fig. 8 Variation diagrams showing the composition of zones within clinopyroxene from **a** post-Oruanui dacites and Oruanui mafic clasts (the latter from Allan 2013), **b** SG1 units B–D, **c** Unit E and **d** Unit S mafic clasts. *Large arrows* indicate general direction of normal crystal core to rim compositional zoning. Enstatite content (En %) calculated as 100*(Mg/(Ca + Mg + ∑Fe)). See Online Resource 3 for raw data and standards

Melt volatile content

Melt inclusions were abundant within plagioclase from the dacites and display a range of compositions (Figs. 5a, 7c). The large size (up to 100 μm) and number of melt inclusions within single crystals allowed for multiple inclusions to be analysed several times for volatile concentrations by FTIR. In most cases, the plagioclase melt inclusions have leaked during decompression and ascent as reflected by the low H_2O and CO_2 contents (Online Resource 5). However, some inclusions gave multiple analyses of >5 wt% H_2O, despite with low CO_2 values (<50 ppm). We therefore consider that these inclusions give a minimum estimate of the volatile concentrations in the dacites. Such values are

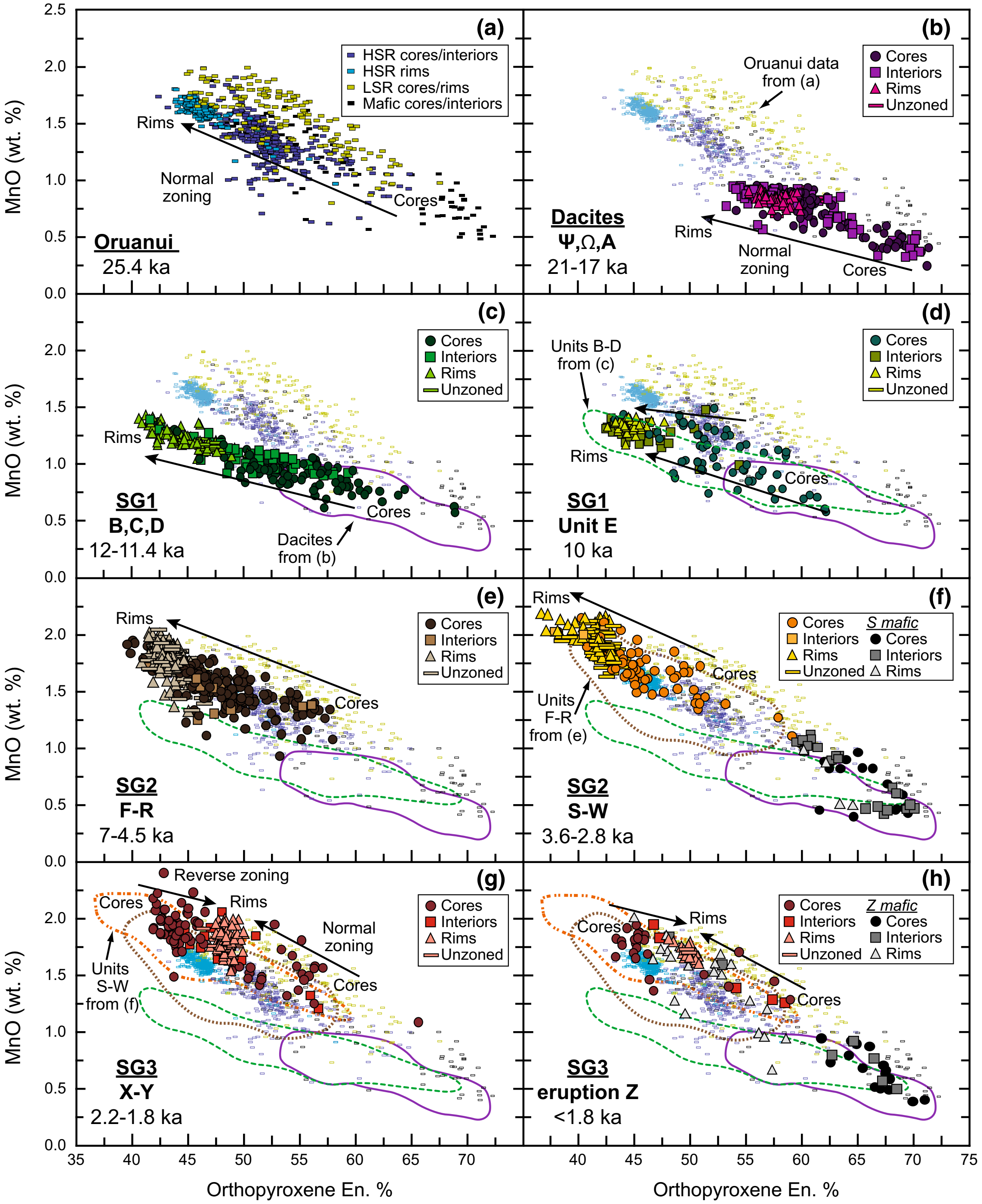

Fig. 9 Variation diagrams showing the composition of zones within orthopyroxene from **a** Oruanui rhyolites and mafics (Allan et al. 2013), **b** post-Oruanui dacites, **c** SG1 units B–D, **d** SG1 Unit E, **e** SG2 units F–R, **f** SG2 units S–W and mafic clasts from Unit S, **g** SG3 units X–Y and **h** SG3 eruption Z lava and mafic inclusions. *Large arrows* indicate the general direction of crystal core to rim compositional change. Enstatite content (En %) calculated as 100*(Mg/(Ca + Mg + ∑Fe)). Oruanui data from **a** are shown as *small open rectangles* in **b**–**h**. Note the contrasting compositions between the SG2 and SG3 orthopyroxenes and the SG1 orthopyroxenes, and the change from normal zoning with low-En rims in SG2 to dominantly reverse zoning with high-En rims in the SG3 eruptions. See Online Resource 3 for raw data and standards

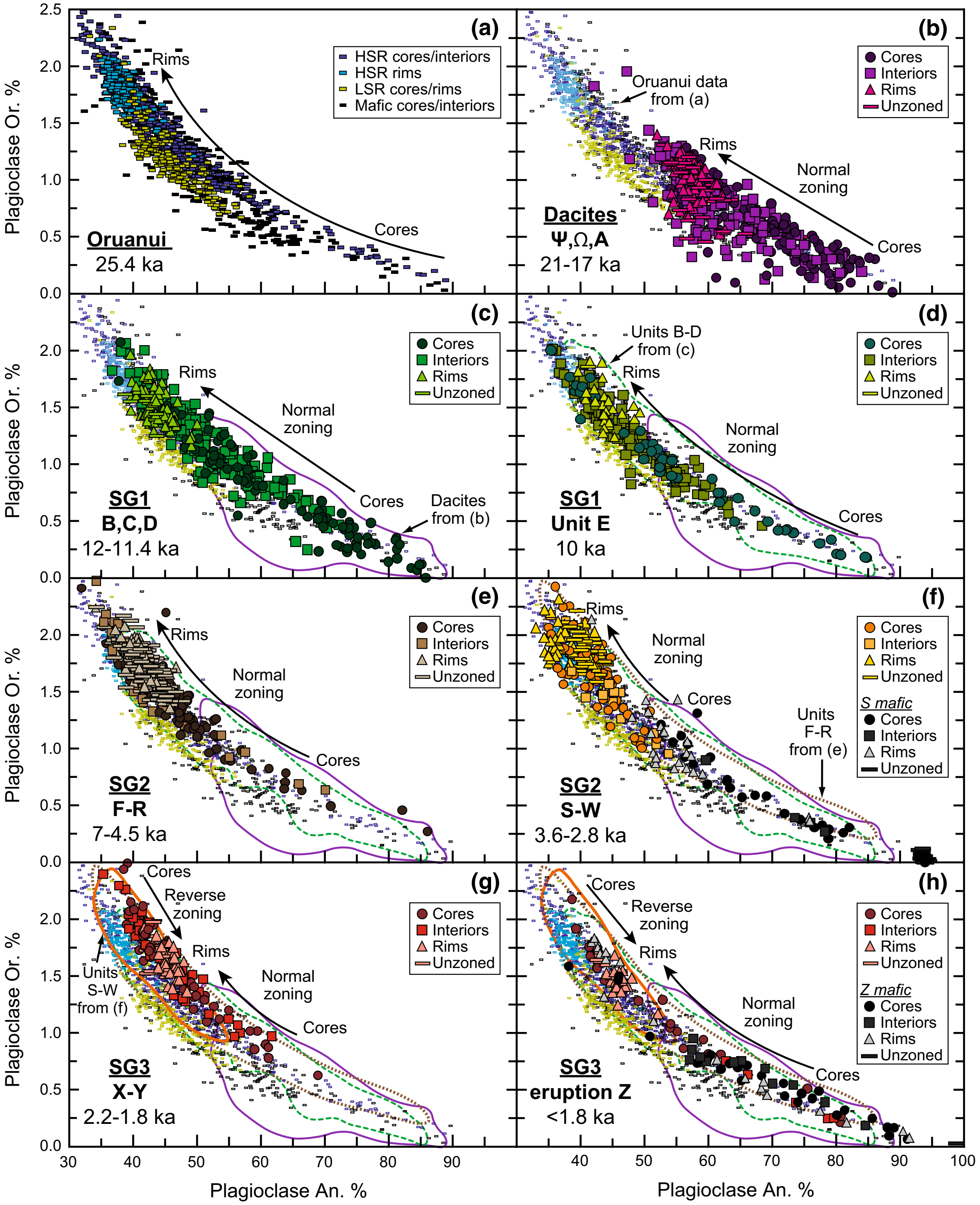

Fig. 10 Variation diagrams showing the composition of zones within plagioclase from **a** Oruanui rhyolite types and mafics (Allan 2013), **b** post-Oruanui dacites, **c** SG1 units B–D, **d** SG1 Unit E, **e** SG2 units F–R, **f** SG2 units S–W and mafic clasts from Unit S, **g** SG3 units X–Y and **h** SG3 eruption Z lava and mafic inclusions. Plagioclase anorthite content (An %) calculated as 100*(Ca/(Ca + Na + K)), Orthoclase content (Or %) calculated as 100*(K/(Ca + Na + K)). Note the change from normal zoning with low-An rims in SG2 to dominantly reverse zoning with high-An rims in the SG3 eruptions. Other details are as in Fig. 9. See Online Resource 3 for raw data and standards

in broad agreement with estimates using the plagioclase hydrometer of Putirka (2008) which also gives high H_2O contents of ~4.5 wt% at 900 °C (Table 4).

Melt inclusions are much smaller and far less common in the post-Oruanui rhyolites. Their volatile contents were not investigated in this study, but are reported for Unit Y

Table 4 Temperature estimates calculated from mineral–mineral and mineral–melt equilibrium models

Unit	Age (ka)	Fe–Ti oxide temperatures (°C)			2-PX	CPX-melt	Plag-melt		OPX-melt	
Oruanui		G&E 08	Sz 08	A&L 88			4.5 % H_2O	5.5 %	4.5 % H_2O	5.5 %
HSR	25.4	796 ± 44	771 ± 18	n/d	n/a	n/a	807 ± 4	787 ± 4	793 ± 5	785 ± 5
LSR	25.4	840 ± 44	809 ± 33	n/d	n/a	n/a	861 ± 8	842 ± 8	848 ± 11	839 ± 10
Dacites		G&E 08	Sz 08	A&L 88			4.5 % H_2O	5.5 %	4.5 % H_2O	5.5 %
Ψ	20.5	938 ± 20 (7)	896 ± 19	905 ± 13	907 ± 18 (15)	886 ± 10 (17)	889 ± 4 (42)	865 ± 4	890 ± 3 (11)	880 ± 3
Ω	18.8	943 ± 16 (12)	903 ± 14	911 ± 11	911 ± 22 (37)	891 ± 10 (35)	894 ± 4 (31)	870 ± 3	894 ± 5 (40)	885 ± 5
A	17	930 ± 18 (14)	890 ± 16	900 ± 13	905 ± 15 (12)	890 ± 14 (14)	891 ± 3 (38)	865 ± 3	899 ± 6 (13)	890 ± 5
SG1		G&E 08	Sz 08	A&L 88			4.5 % H_2O	5.5 %	4.5 % H_2O	5.5 %
B	11.8	846 ± 26 (22)	823 ± 18	836 ± 22	832 ± 22 (28)	803 ± 14 (27)	835 ± 5 (19)	813 ± 5	812 ± 6 (45)	805 ± 6
C	11.4	849 ± 19 (6)	824 ± 14	839 ± 16	837 ± 18 (15)	794 ± 25 (16)	835 ± 4 (9)	814 ± 4	817 ± 6 (17)	809 ± 5
D_{lava}	11.4	847 ± 12 (6)	818 ± 10	840 ± 10	842 ± 16 (14)	803 ± 11 (14)	838 ± 4 (29)	817 ± 4	825 ± 3 (14)	817 ± 3
D_{tephra}	11.4	850 ± 37 (10)	823 ± 27	840 ± 29	826 ± 34 (5)	803 ± 6 (5)	835 ± 6 (12)	814 ± 6	813 ± 5 (9)	805 ± 5
E	10	861 ± 11 (17)	832 ± 8	850 ± 9	821 ± 18 (29)	810 ± 17 (36)	839 ± 3 (24)	817 ± 3	820 ± 3 (34)	812 ± 3
SG2		G&E 08	Sz 08	A&L 88			4.5 % H_2O	5.5 %	4.5 % H_2O	5.5 %
F_{lava}	7.1	859 ± 22 (7)	840 ± 15	845 ± 19	n/a	n/a	n/d	n/d	826 ± 3 (29)	818 ± 3
F_{tephra}	7.1	858 ± 18 (9)	831 ± 14	847 ± 14	n/a	n/a	836 ± 2 (14)	812 ± 2	827 ± 3 (19)	819 ± 3
G	6.7	861 ± 14 (13)	833 ± 10	849 ± 10	n/a	n/a	830 ± 2 (4)	808 ± 2	819 ± 3 (20)	811 ± 3
H	6.1	860 ± 24 (11)	835 ± 16	848 ± 21	n/a	n/a	830 ± 4 (9)	808 ± 4	822 ± 3 (20)	814 ± 3
K	5.4	849 ± 37 (13)	829 ± 23	838 ± 31	n/a	n/a	832 ± 4 (29)	810 ± 4	826 ± 2 (29)	818 ± 2
L_{tephra}	5.3	874 ± 19 (7)	845 ± 16	858 ± 15	n/a	n/a	838 ± 4 (19)	816 ± 4	824 ± 3 (17)	816 ± 3
M	5.3	864 ± 20 (9)	838 ± 14	851 ± 16	n/a	n/a	832 ± 3 (18)	811 ± 3	821 ± 4 (21)	813 ± 4
N	4.9	876 ± 19 (9)	848 ± 15	860 ± 14	n/a	n/a	830 ± 4 (18)	808 ± 4	826 ± 3 (26)	818 ± 3
O	4.8	862 ± 34 (12)	838 ± 30	850 ± 24	n/a	n/a	828 ± 2 (16)	806 ± 2	816 ± 3 (25)	808 ± 3
P	4.8	870 ± 28 (6)	844 ± 22	854 ± 22	n/a	n/a	832 ± 2 (25)	810 ± 2	826 ± 2 (24)	818 ± 2
Q	4.6	869 ± 14 (7)	845 ± 11	854 ± 11	n/a	n/a	832 ± 5 (21)	811 ± 5	825 ± 3 (25)	817 ± 3
R	4.5	876 ± 12 (7)	850 ± 9	859 ± 10	n/a	n/a	832 ± 4 (20)	810 ± 4	825 ± 3 (18)	817 ± 3
S	3.6	874 ± 15 (14)	850 ± 10	857 ± 12	n/a	n/a	834 ± 3 (25)	812 ± 3	826 ± 2 (23)	818 ± 2
S_{mafic}	3.6	1019 ± 18 (7)	973 ± 20	947 ± 13	986 ± 33 (7)	n/a	n/a	n/a	n/a	n/a
T	3.2	876 ± 7 (6)	852 ± 6	859 ± 14	n/a	n/a	819 ± 4 (19)	798 ± 4	821 ± 3 (28)	813 ± 3
U	2.9	863 ± 16 (10)	844 ± 7	848 ± 14	n/a	n/a	817 ± 3 (18)	796 ± 2	816 ± 4 (23)	808 ± 4
V	2.8	853 ± 15 (12)	837 ± 8	839 ± 13	n/a	n/a	815 ± 5 (11)	794 ± 5	813 ± 5 (16)	805 ± 5
W	2.8	851 ± 15 (7)	836 ± 9	837 ± 14	n/a	n/a	814 ± 4 (15)	793 ± 4	813 ± 6 (24)	806 ± 6
SG3		G&E 08	Sz 08	A&L 88			4.5 % H_2O	5.5 %	4.5 % H_2O	5.5 %
X	2.2	878 ± 15 (8)	848 ± 12	863 ± 11	n/a	n/a	848 ± 4 (20)	825 ± 4	849 ± 2 (18)	840 ± 2
Y	1.8	879 ± 23 (16)	850 ± 16	865 ± 18	n/a	n/a	850 ± 3 (49)	828 ± 3	852 ± 3 (60)	843 ± 2
Z	1.8	871 ± 23 (11)	850 ± 10	856 ± 14	n/a	n/a	*850 ± 3 (24)*	*827 ± 3*	*852 ± 3 (24)*	*844 ± 3*

Fe–Ti oxide temperature estimates are from either touching magnetite-ilmenite pairs or coexisting oxide pairs on the same crystal or glomerocryst using the models of Ghiorso and Evans (2008) (G&E), Sauerzapf et al. (2008) (Sz) and Andersen and Lindsley (1988) (A&L). All magnetite–ilmenite pairs satisfied the Mg–Mn partitioning test of Bacon and Hirschmann (1988). Temperatures from matched mineral–glass pairs fall within the equilibrium criterion for each thermometer as outlined by Putirka (2008), with clinopyroxene being an exception likely due to the equations not adequately accounting for partitioning of Fe^{2+} relative to Fe^{3+} in pyroxene (Gelman et al. 2013). Water in plagioclase–liquid and orthopyroxene–liquid thermometers from Putirka (2008) is shown for both 4.5 and 5.5 wt% H_2O for comparison. Clinopyroxene–liquid thermometer is shown for 5 wt% H_2O only. Pressures were set at 100 MPa for the rhyolites and 200 MPa for the dacites for the mineral–melt thermometers. Number of temperature estimates shown for each thermometer in brackets, uncertainty is 2 SD. Oruanui HSR and LSR data are from Allan (2013) and Wilson et al. (2006), with recalibrated Fe–Ti oxide compositions based on the normalisation technique of Evans et al. (2006). n/a not available, n/d not determined

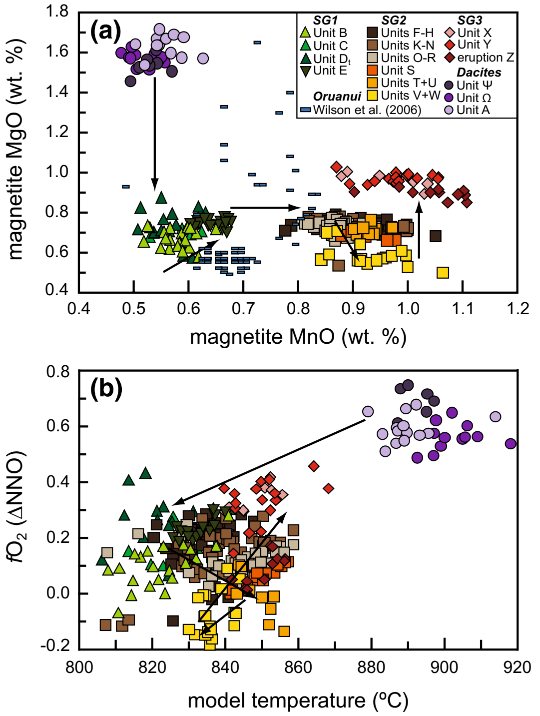

Fig. 11 Compositions of Fe–Ti oxides and intensive parameter estimates from the post-Oruanui dacites and rhyolite subgroups. *Arrows* indicate trends linking the eruptions through time. **a** Variations in MgO and MnO in magnetite between the subgroups through time. Similar broad trends are also reflected in the composition of ilmenite (see Table 4 and Online Resource 3, Table 2). **b** Temperature and fO_2 [plotted as $\log_{10} fO_2$ relative to the Ni–NiO oxygen buffer of O'Neill and Pownceby (1993)] estimates calculated from matched magnetite and ilmenite pairs using the Fe–Ti exchange-based thermometer of Sauerzapf et al. (2008). Only coexisting Fe–Ti oxide pairs (either sharing a common boundary or occurring together in the same phenocryst) were used to ensure textural equilibrium (Blundy and Cashman 2008). Fe–Ti pairs were also tested for equilibrium using the Mg/Mn partitioning test from Bacon and Hirschmann (1988)

in Dunbar et al. (1989a) and Dunbar and Kyle (1993). Water content estimates have been made using amphibole hygrometry for the SG1 rhyolites and plagioclase hygrometry for the remaining eruptions. The amphibole model of Ridolfi et al. (2010) yields an H_2O estimate of ~5–6.5 wt% for units B–E (Fig. 12), similar to the upper range of volatile estimates for the Oruanui HSR (Liu et al. 2006; Allan et al. 2012; Allan 2013) and in line with the plagioclase hygrometer of Putirka (2008) at magma temperatures of <820 °C (Table 4). For the SG2–SG3 eruptions, higher-temperature estimates from Fe–Ti oxides are more consistent with lower melt H_2O contents of <5 wt%, in agreement with changes in observed mineral phases, and volatile concentrations in plagioclase-hosted melt inclusions from Unit Y measured by ion microprobe and FTIR (Dunbar and Kyle 1993; Saunders 2009, respectively).

Pressure

Two methods have been used to estimate the crystallisation pressures for the post-Oruanui magmas. First, the amphibole barometer of Ridolfi et al. (2010) yields model pressures for SG1 rhyolites that are similar to the pressure range determined for Oruanui magmas (Fig. 12). Unzoned amphiboles in units B and C yield model pressures of ~100–150 MPa, similar to those in the Oruanui HSR amphiboles and consistent with pressures calculated from Oruanui quartz-hosted melt inclusions (Liu et al. 2006). The inferred xenocrystic amphiboles from the early SG1 units give model values that overlap with the Oruanui LSR and mafic amphiboles, reflecting their likely deeper source. Groundmass amphibole from Unit S mafic clasts yield pressure estimates of >250 MPa, corresponding to the highest pressures inferred from Oruanui mafic amphiboles (Allan 2013). However, these high-pressure estimates may be considered less reliable using the Ridolfi et al. (2010) barometer as they could alternatively reflect strong compositional shifts or temperature changes with magma mixing (e.g. Coombs et al. 2013; Erdmann et al. 2014). Saturation pressures (P_{H_2O}) calculated for the few dacite melt inclusions with high H_2O are ~200 MPa at 900 °C (Online Resource 5; Newman and Lowenstern 2002) and are considered to be minima as the low CO_2 values suggest that leakage has occurred during decompression. If CO_2 levels are assumed to be similar to those observed in quartz melt inclusions from the Oruanui (>100 ppm: Liu et al. 2006), P_{H2O} estimates increase to >220 MPa. Such pressures are equivalent to depths of >8 km in the TVZ crust and are intermediate in value between the amphibole barometry estimates for the shallower SG1 rhyolites (4–6 km) and deeper mafic clasts (>10 km) (Fig. 12a). For comparative purposes, pressures calculated for Oruanui melt inclusions are typically 120–150 MPa (Liu et al. 2006) and <150 MPa for the Taupo ignimbrite (Unit Y), the latter using a water content of 4.3 wt% at temperatures of 850 °C (Dunbar and Kyle 1993; Saunders 2009). Slightly higher pressures of 150–200 MPa have been calculated for the Taupo ignimbrite using rhyolite melts geobarometery, based on quartz–feldspar-melt equilibrium pressures (Bégué et al. 2014). However, we did not find phenocrystic quartz in any of the eruptive phases of the Taupo (Unit Y) eruption or any of the other post-Oruanui eruptions (Table 2).

Discussion

The trends identified in whole-rock, glass and mineral compositions from the post-Oruanui eruptions highlight not only broad changes in erupted magma chemistries in the aftermath of the Oruanui supereruption, but also subtle,

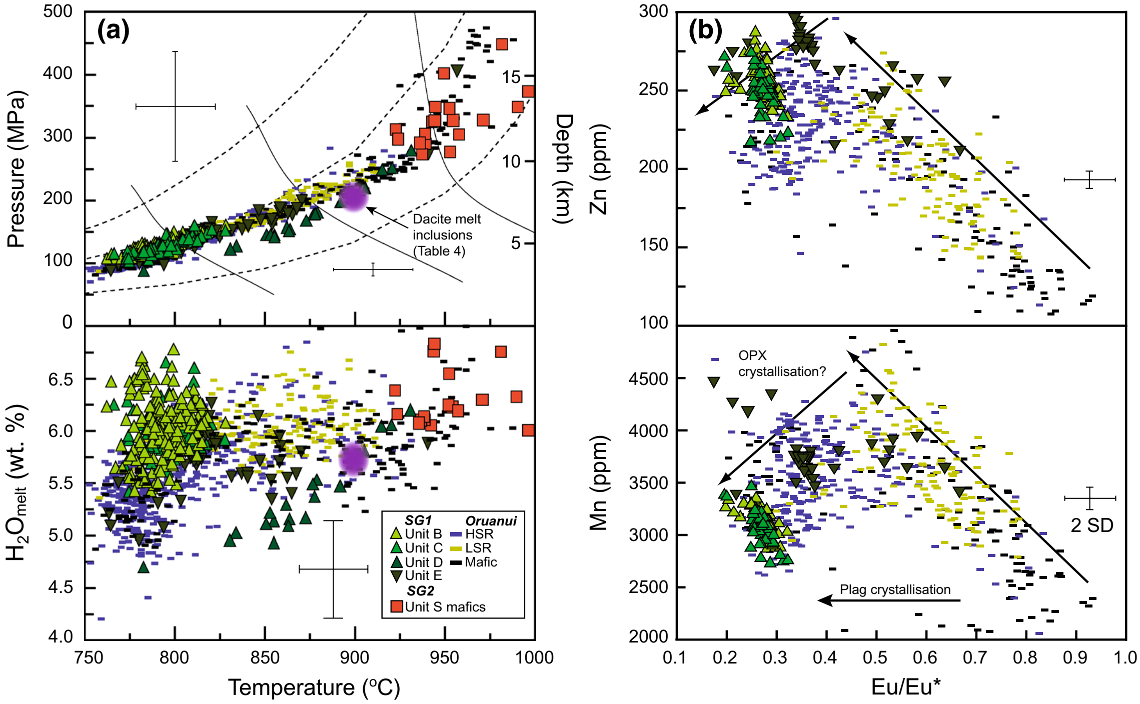

Fig. 12 Variation diagrams showing **a** intensive parameter estimates and **b** trace-element compositions for post-Oruanui amphiboles (this study) and the Oruanui magma-type amphiboles from Allan (2013). Temperatures, pressures and melt H_2O estimates were made using the Ridolfi et al. (2010) model with 2 SD error bars shown for the range of compositions. See Online Resources 3 and 4 for raw data

yet important changes in the host magmatic system over short time intervals. Sutton et al. (1995, 2000) observed stepwise compositional changes between, and limited variation within, three separate rhyolitic subgroups and interpreted these changes to reflect petrogenetically distinct magmatic systems. We build upon their interpretations to consider what processes generated the observed changes in composition, with implications for the structure of Taupo's post-supereruption magmatic system through time.

Comparisons between Oruanui and post-Oruanui magma compositions

The huge volume of the Oruanui melt-dominant magma body, the implicit consequential size of the underlying mush system (Allan 2013), and the geographical superposition of vents for the Oruanui and post-Oruanui eruptions (Fig. 1) make it likely that residual melts or crystals from the Oruanui system should occur in the post-supereruptive environment. Such an inference applies whether Oruanui compositions are represented by specific whole-rock, melt or mineral compositional trends or contribute to unique mixing trends with any newly generated melts. The field of Oruanui rhyolite compositions, however, does not appear to be explicitly represented in the post-Oruanui eruptions, which instead show several key contrasts:

1. Mineral compositions differ significantly from the Oruanui, with unique compositional trends in orthopyroxene MnO content for the dacites and SG1 rhyolites, and plagioclase does not overlap in composition with low-An Oruanui plagioclase (Figs. 9, 10).
2. Whole-rock and glass compositions follow separate linear trends on many major and trace-element variation diagrams (Figs. 2, 3), with post-Oruanui whole-rock compositions not reaching the high-silica values of the Oruanui HSR. Both groundmass and melt-inclusion glasses in the post-Oruanui eruptives are chemically distinctive, only rarely chemically overlapping with the high-silica Oruanui glass (Figs. 5, 6).
3. The post-Oruanui magmas are distinctly more radiogenic than the Oruanui magmas with $^{87}Sr/^{86}Sr > 0.7059$ (Sutton et al. 1995) and no signs of any mixing relationship.
4. The post-Oruanui magmas experienced different crystallisation conditions to the Oruanui magmas, as they developed under significantly hotter and more reducing conditions, but at similar inferred depths within the crust (Figs. 11, 12, 13; Table 4).

Barker et al. (2014) showed that the post-Oruanui magmas inherited very few Oruanui-aged zircons (<12 % within uncertainty) and suggested that the Oruanui

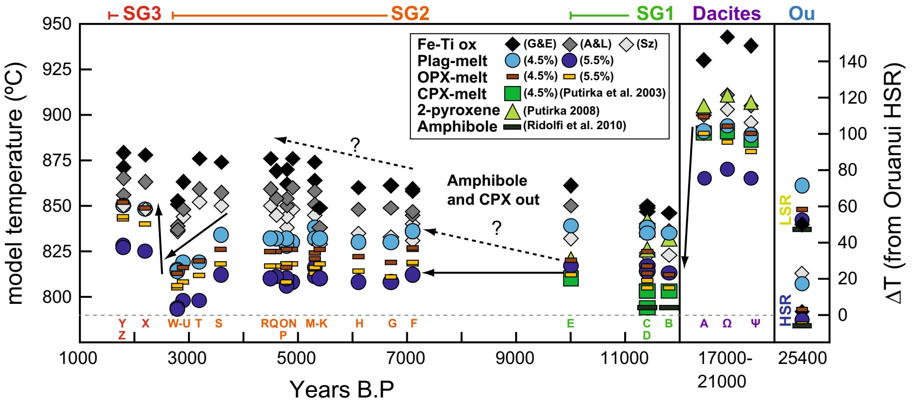

Fig. 13 Variations in magmatic temperature estimates for selected mineral–mineral and mineral–melt equilibrium models for eruptions from Taupo volcano through time. Temperatures for the Oruanui HSR and LSR are from Allan (2013) and Wilson et al. (2006), with recalibrated Fe–Ti oxide compositions based on the normalisation technique of Evans et al. (2006). Fe–Ti oxide temperature estimates are either from touching magnetite-ilmenite pairs or from coexisting oxide pairs on the same crystal or glomerocryst using the models of Ghiorso and Evans (2008) (G&E), Andersen and Lindsley (1988) (A&L) and Sauerzapf et al. (2008) (Sz). All pairs satisfied the Mg–Mn partitioning test of Bacon and Hirschmann (1988). Temperatures from matched mineral–glass pairs satisfy the equilibrium criterion for each thermometer as outlined by Putirka (2008), with the exception of clinopyroxene likely due to the equations inadequately accounting for partitioning of Fe^{2+} relative to Fe^{3+} in pyroxene (Gelman et al. 2013). Water in plagioclase–liquid and orthopyroxene–liquid thermometers from Putirka (2008) is shown for both 4.5 and 5.5 wt% H_2O for comparison. Clinopyroxene–liquid thermometer is shown for 5 wt% H_2O only. Pressures were set at 100 MPa for the rhyolites and 200 MPa for the dacites for the mineral–melt thermometers. See text for discussion

magmatic system was chronologically reset through thermally induced dissolution of zircon. Here, we extend this interpretation to suggest that the wider mush system experienced a significant shift in temperature and storage conditions to the extent that little or no chemical evidence of the Oruanui magmatic system survived to be imparted to the post-Oruanui magmatic system.

Widespread thermal modification of the post-Oruanui magmatic system requires a significant heat source. As shown by quantitative field constraints, mafic magma intrusion into crystalline silicic mush can have significant effects on the structure and thermal stability of magma reservoirs and can result in large-scale overturn (Bain et al. 2013). Hot mafic magmas of two compositional lineages are recorded as discrete pyroclasts and as inclusions in pumice from the Oruanui eruption (Sutton et al. 1995; Wilson et al. 2006; Allan 2013). The total volume of mafic magma erupted in the Oruanui (3–5 km^3: Wilson et al. 2006) is considered to represent only a minor portion of the mafic melts involved in the parental magmatic system. Here, it is inferred that the huge decompression caused by the evacuation of >530 km^3 of Oruanui rhyolite resulted in widespread mafic magma influx and heating of any remaining melt body or crystalline residue in the immediate post-supereruptive environment. Synchronous changes in storage conditions are supported by the relative shift in $^{87}Sr/^{86}Sr$ ratios, where the more radiogenic post-Oruanui magmas are consistent with increased melting and assimilation of country rock, most plausibly Mesozoic greywacke (Sutton et al. 1995, 2000; Charlier et al. 2010).

In contrast to the differences noted for silicic compositions, post-Oruanui mafic materials, analysed as discrete clasts from Unit S and mafic inclusions in pumice from Unit Y and eruption Z, have whole-rock major and trace-element compositions which overlap with the Oruanui tholeiitic mafic clasts (Figs. 2, 3; Allan 2013). These observations highlight that although the Oruanui and post-Oruanui silicic melts are significantly different, the deeper-derived mafic magmas appear to have remained the same. However, the contrast between post-Oruanui mafic compositions and the primitive calcalkaline Waimarino basalt erupted <20 km to the south during this time period (Fig. 1a) suggests that there may be pronounced contrast in mafic melt chemistry and sources across geographical distances of <30 km. Alternatively, these contrasts may reflect differences in crystal fractionation paths, crystal accumulation, mixing and filtering action in the crust due to largely different crustal structures and plumbing systems, as demonstrated in the broader trends in basalt chemistry across the TVZ (Gamble et al. 1990, 1993).

Post-supereruption reorganisation and reconstruction of Taupo's magmatic system

Origin and significance of the ~21–17 ka dacites

The post-Oruanui dacites are hotter, more oxidised and relatively more crystal rich than the later rhyolites of SG1–3, with a wide range in crystal core and melt-inclusion

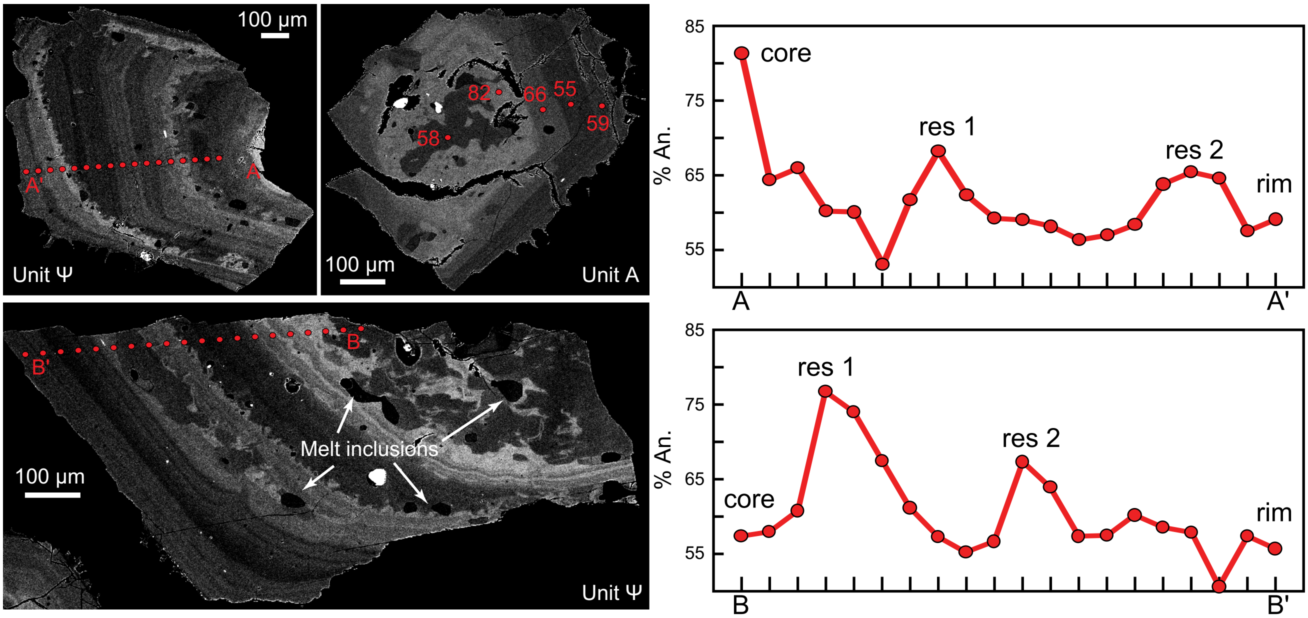

Fig. 14 Representative BSE images and compositional profiles of plagioclase from the post-Oruanui dacites showing variation in anorthite (An) from core to rim, with approximate probe spot locations shown by *red dots* with their corresponding compositions. Multiple high-An resorption zones (*res*) are inferred to represent dissolution resulting from recharge and mixing with hotter or less evolved mafic melts

compositions accompanying a comparatively narrow range in crystal rim and matrix glass compositions (Figs. 5, 8, 9). Charlier et al. (2010) showed that Unit Ω was strongly zircon undersaturated and yet contained minor amounts of euhedral xenocrystic zircons, the U–Pb age spectrum of which was used to link the grains to greywacke country rock and intrusions dating from the 350 ka Whakamaru eruption. Such observations provide unequivocal evidence for open-system dacite melt genesis involving some proportion of assimilated crustal material, with the crustal source needing to melt to the point of disintegration to liberate individual zircons (Charlier et al. 2010). Gelman et al. (2013) proposed that crustal involvement and zircon incorporation were due to down-temperature evolution of a mid-to-lower crustal dacite magma via fractional crystallisation with some minor late assimilation. Our mineral compositions for all three dacite units match those of Unit Ω analysed by Gelman et al. (2013) where crystal rim compositions are relatively restricted and most of the crystal cargo appears to be in equilibrium with the host melt (Table 4). However, the wide range of crystal core textures, compositions and melt-inclusion compositions in the dacites suggest that there were periods of significant mineral–melt disequilibrium (Figs. 5, 7, 14). Such observations raise questions as to whether the dacite compositions at Taupo were formed solely through down-temperature fractional crystallisation from a less evolved basaltic parent or whether mixing processes also played an important role.

In considering the origin of the dacites, two key variables are important:

1. *The depths and conditions of crystallisation*. Assuming a crustal density of 2.65 g/cm^3, pressures estimates from Unit Ω melt inclusions of ~200–220 MPa equate to depths of ~7.5–9 km (Online Resource 5). These are deeper than those calculated from Oruanui melt inclusions (4–6.5 km: Liu et al. 2006), but corresponds to estimates for depths of the Oruanui mush body from amphibole barometry (Allan et al. 2013) and low resistivity zones, interpreted as partially molten bodies, in an area north of Taupo (Heise et al. 2010). Similar depths for intermediate composition mush zones are also reported for Okataina volcanic centre in the TVZ (Shane et al. 2007, 2008; Smith et al. 2010; Cole et al. 2014). Rim compositions of Taupo dacite plagioclase (~An$_{60}$) are consistent with experimental studies of plagioclase in similar composition melts at P_{H_2O} >180 MPa at 900 °C, a melt fraction of ~0.8 and 5.5 wt% H_2O (Fig. 10 of Cashman and Blundy 2013). Melt-inclusion pressures are therefore considered to reflect the final storage conditions of the dacites, consistent with plagioclase rim compositions. However, high-An cores and resorbed internal boundaries in plagioclase also either highlight a history of the dacites at significantly higher pressures and temperatures or more plausibly reflect interaction with and/or

inheritance of crystals from hotter, less evolved melts (Fig. 14). The pressure range of 300–700 MPa (equivalent to depths of 11–26 km) used for modelling by Gelman et al. (2013) is not consistent, however, with either the observed compositional range of plagioclase or the crustal structure of the TVZ, where there is a rapid transition at 15 km depth to heavily intruded mafic lower crust (Harrison and White 2006). Even mafic compositions erupted from Taupo rarely yield barometry estimates of >400 MPa (Fig. 12; Allan 2013).

2. *The compositions of parental magmas or assimilates.* Four starting compositions are considered to be plausible for modelling AFC or partial melting processes in genesis of the dacites. First, if the dacites were generated through fractionation from a basaltic or basaltic–andesite parent, then the most appropriate starting composition is likely to be similar to the Oruanui mafic clasts. However, the mafic clasts range in composition and themselves reflect differentiation and/or mixing processes, with the tholeiitic clasts notably approaching the composition of the dacites (Wilson et al. 2006; Allan 2013; Figs. 2, 3). Second, a greywacke parent or assimilant could be considered as a source, which would explain the elevated $^{87}Sr/^{86}Sr$ values and zircon age spectrum (Graham et al. 1992, 1995; Sutton et al. 2000; Charlier et al. 2010). The isotopic ranges, bulk composition and mineralogy of the dacites, however, preclude a source purely from the melting of greywacke (Conrad et al. 1988). Third, a Whakamaru plutonic residue could be involved given the geographical overlapping of the caldera margins (Fig. 1a; Wilson et al. 1986). Whakamaru magmas have broadly similar whole-rock and isotopic compositions to the Oruanui and post-Oruanui magmas, and small amounts of assimilation would be difficult to identify, except through zircon inheritance (Charlier et al. 2010; Barker et al. 2014). Fourth, mixing with Oruanui mush compositions could have occurred, given the apparent depths at which the dacites were stored. However, as with the Whakamaru source, significant levels of melting or assimilation immediately prior to eruption would likely result in inheritance of Oruanui crystal cores and xenocrystic melt inclusions. Oruanui crystal compositions and Oruanui-aged zircons in the dacites and SG1 rhyolite magmas occur only in minor proportions (<5 %: Charlier et al. 2010; Barker et al. 2014). If Oruanui residues were important in the genesis of dacite magmas, all direct evidence for this source has been overprinted.

Given the parameters and scenarios outlined above, we consider it most plausible that the dacites were sourced from a region spatially overlapping with the base of the proto-Oruanui mush system, at depths of ≥~8 km (Allan 2013), similar to that documented by Millet et al. (2014) for dacites erupted from nearby Tauhara volcano (Fig. 1a). The Oruanui crystal mush would, from its mineralogical characteristics, provide a logical level at which ascending mafic magmas would pond due to density contrasts. Newly incoming mafic melts stalling and differentiating at this level would heat the proto-Oruanui system and drive widespread thermal dissolution of Oruanui-sourced crystal phases such as zircon. Bulk compositions of the dacites can be generated for some elements by ~40–50 % mixing between Oruanui rhyolite and a low SiO_2 tholeiitic end-member (Fig. 15a). However, the dacite compositions do not fall on Oruanui mixing trends for elements such as Zr or P (Fig. 3a), which are decoupled and characteristic of crystal fractionation involving apatite, but not zircon (Lee and Bachmann 2014). Although mixing clearly occurred at some point in their early history (Fig. 14), the majority of the post-Oruanui dacite mineral rims are in equilibrium with their host melt and show evidence for extensive crystallisation to evolved compositions (Fig. 14; Gelman et al. 2013). Indeed, dacite compositions can be modelled by perfect fractional crystallisation from the most primitive Oruanui tholeiitic compositions, through ~60 % crystallisation (Sutton et al. 2000), but they must have additionally incorporated significant amounts of more radiogenic material at some point in order to achieve elevated $^{87}Sr/^{86}Sr$ values.

Establishment of the (new?) silicic mush system from <17 ka

After ~5 ka of quiescence following the post-Oruanui dacite eruptions, Taupo resumed erupting with the SG1 rhyolites, with three features genetically linking them to the earlier dacites (Sutton et al. 2000). First, the mineralogies of the dacites and SG1 rhyolites are similar, with crystal compositions forming continuous chemical trends and with SG1 crystal core compositions overlapping with those of dacite rims and interiors (Figs. 8, 9, 10). Second, dacite glass compositions lie on a trend intermediate to the dacite whole-rock and SG1 rhyolites (Fig. 4), while some melt inclusions from the SG1 rhyolites overlap compositionally with dacite glass selvedges (Fig. 5). Third, the dacites and SG1 rhyolites have similar $^{87}Sr/^{86}Sr$ values, with only a slight increase, which can be explained by incorporation of ~2–5 % extra greywacke melt (Sutton et al. 2000). The rhyolites are significantly more reduced than the dacites, but this is not surprising given the differing intensive parameters, mineralogy, crystal compositions and the presence of pyrrhotite inclusions in the dacites, which indicate sulphide precipitation that could significantly affect degassing dynamics (e.g. Burgisser and Scaillet 2007).

The dacite whole-rock and dacite glass compositions can be linked by ~30–35 wt% fractional crystallisation using

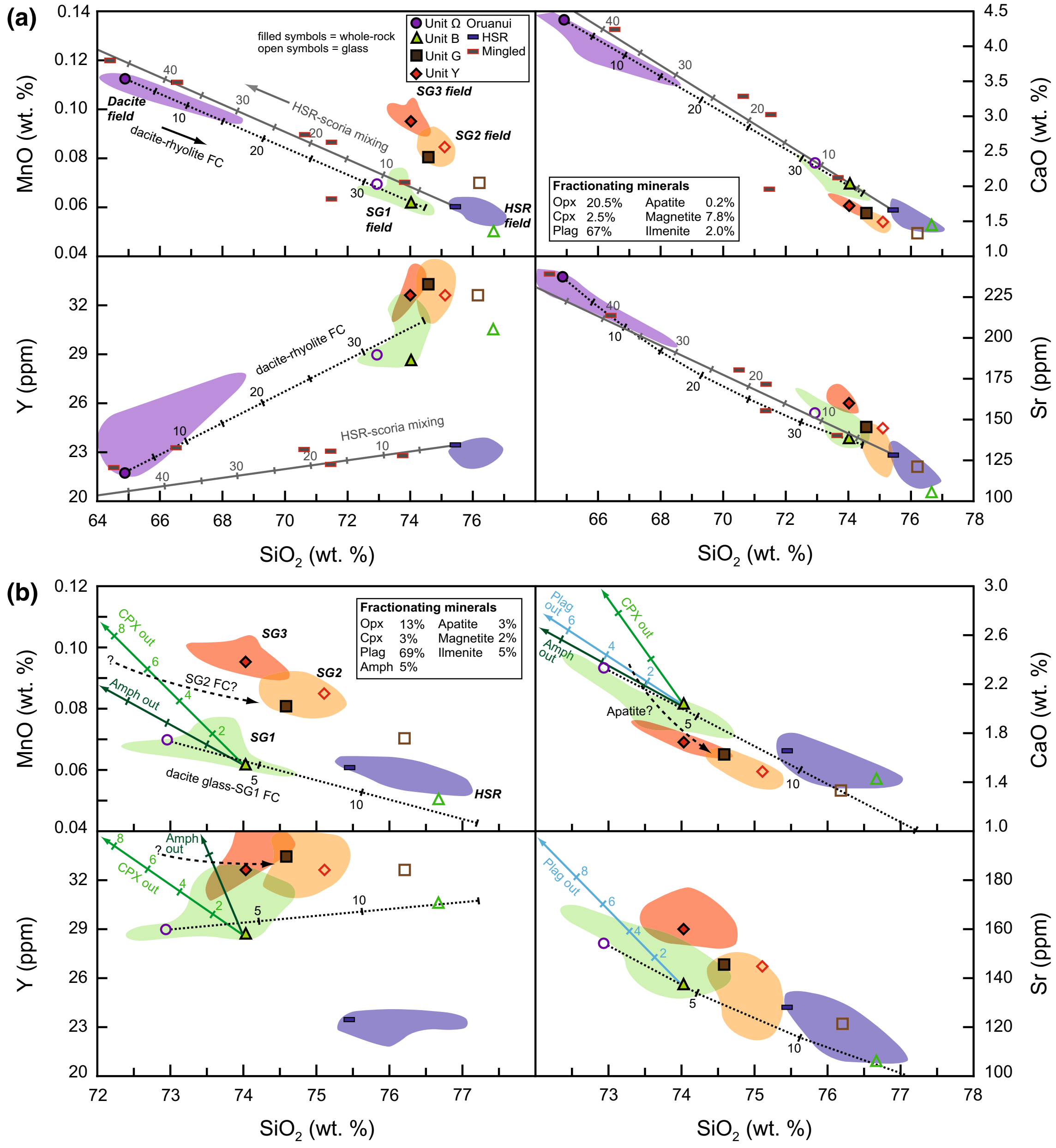

Fig. 15 Selected major and trace-element variation diagrams showing the inferred chemical evolution pathways of post-Oruanui magmas with fractional crystallisation and/or magma mixing. **a** Fractional crystallisation (FC) path (*dotted black line*) linking the Ω dacite whole-rock composition with dacite glass and rhyolite whole-rock compositions through >30 % crystallisation. Magma mixing trend (*grey line*) between the Oruanui HSR and the Oruanui tholeiite scoria from Wilson et al. (2006) is shown for an alternative origin of the dacite magmas. Mingled pumices refer to Oruanui pumices showing physical evidence for mixing. **b** Fractional crystallisation path linking the Ω dacite glass composition with the SG1 rhyolite whole-rock and glass compositions. A representative whole-rock (*filled symbol*) and glass (*open symbol*) compositional pair are shown for each subgroup for reference. Mixing vectors (*green* and *blue arrows*) refer to the compositional change inferred with the dissolution of the observed mineral phases, with tick marks at 2 % increments. Note the elevated MnO and Y resulting from the dissolution of clinopyroxene and/or amphibole. *Dashed black* FC *arrow* represents the potential evolution path of the SG2 and SG3 magmas after post-SG1 dissolution. Mineral partition coefficients calculated from mineral rim-glass pairs for amphibole and clinopyroxene are from this study and Allan (2013) for orthopyroxene. Plagioclase Sr partition coefficients calculated using Blundy and Wood (1991) for An_{55} for the dacites and An_{40} for the rhyolites at 900 and 840 °C, respectively. Models performed using PETROMODELER program from Ersoy (2013). See text for discussion

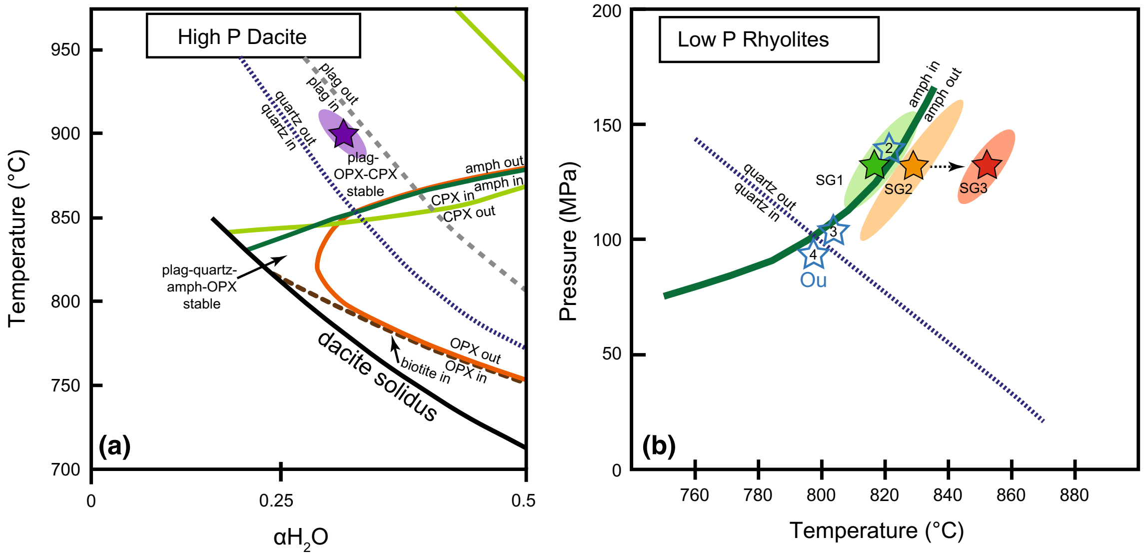

Fig. 16 Comparison between magmatic conditions for the post-Oruanui magmas and experimental results for phase equilibria from **a** Conrad et al. (1988) for average TVZ dacites at high pressures (10 kbars) and **b** Coombs and Gardner (2001) for rhyolites from Katmai at 4 wt% H_2O. The inferred conditions for the post-Oruanui magmas are shown by *filled stars* within an ellipse representing the approximate range of temperature (Table 4) and pressure (Fig. 12) estimates. *Blue stars* labelled 2–4 represent key points in the development and decompression of the Oruanui (*Ou*) melt-dominant body from Allan et al. (2013) for comparison, where quartz is only stable in the shallowest region of the Oruanui magma reservoir

the outermost rim compositions of the crystal phases (Sutton et al. 2000; Fig. 15a). Some elements (e.g. Sr, Ti) do not fit the model, likely due to slight enrichments through resorbed or inherited high-An or high-En crystal cores. With further fractionation of the dacite glass by ~5 wt%, using mineral phases of the SG1 rhyolites, the whole-rock SG1 rhyolite compositions can be achieved, and with 10–15 % fractionation, the SG1 rhyolite glass compositions can be reached (Fig. 15b). The degree of crystallisation required to chemically link the dacite whole-rock and rhyolite melt compositions approaches ~50 %, which we infer to correspond with an important stage in the evolution of the magmatic system. At crystallinity levels of >50 %, the magma is likely to reach rheological locking point and form a rigid mush (e.g. Marsh 1981; Vigneresse et al. 1996; Bachmann and Bergantz 2008; Dufek and Bachmann 2010; Deering et al. 2011). The dacite magmas are therefore interpreted to represent a forerunner or pre-mush snapshots of the newly established and genetically linked rhyolite-generating system, which cooled in the time period between eruption of the dacites and SG1 rhyolites. A subpopulation of zircons in the post-Oruanui rhyolites have ages clustering at ~16 ka, implying that parts of the magmatic system were evolved enough to crystallise zircon during this time (Barker et al. 2014). By 12 ka, it is apparent that a significant volume of silicic mush had rebuilt, with relatively uniform magma chemistries being erupted from geographically dispersed vents (Fig. 1). The rhyolite-producing magmatic system at Taupo rebuilt itself in only ~10 kyr following the supereruption and had moved into a new cycle of eruptions only ~13.5 kyr after the Oruanui event.

The strong connection between the dacites and SG1 rhyolites is also reflected in the appearance of amphibole, indicating lower pressures and changing conditions in the magmatic system. Recent studies have shown that caution must be taken when using Al concentrations in amphibole (Ridolfi et al. 2010) as a proxy for crystallisation pressure alone (Coombs et al. 2013; Shane and Smith 2013; Erdmann et al. 2014). However, model pressures of 100–150 MPa from amphibole in units B and C match values from Oruanui HSR amphibole rims, which in turn are in agreement with volatile saturation pressures from Oruanui quartz-hosted melt inclusions (Fig. 12; Liu et al. 2006; Allan et al. 2012). In addition, the majority of amphiboles from units B and C are unzoned and euhedral, with little to no difference in composition between their cores and rims (Fig. 7d). The appearance of euhedral amphibole in SG1 is considered to reflect changing mineral stability in the early magmatic system (Fig. 16). In such a case, the dacites were likely too hot for amphibole or quartz to crystallise but were able to crystallise plagioclase, clinopyroxene and orthopyroxene, in agreement with experimental studies (Fig. 16a; Conrad et al. 1988), albeit conducted at much higher pressures than those considered likely for the post-Oruanui dacites. Experimental studies on rhyolites of broadly similar composition to Taupo (Coombs and Gardner 2001) are consistent with the observed mineralogy changes at 12 ka, where the early SG1 magmas had cooled sufficiently and moved to lower pressures to enter the amphibole stability field (Fig. 16b). Crystal fractionation paths between the dacites and SG1 rhyolites require amphibole crystallisation to explain the trends observed in amphibole-compatible elements such as Y and Mn (Fig. 15b). The younger SG1 (and SG2/SG3) eruptions then moved out of the amphibole stability field again, by either a slight temperature increase (Table 4; Fig. 16b) or H_2O decrease (e.g. Dall'Agnol et al. 1999; Klimm et al. 2003). Notably, in the experimental studies of Conrad et al. (1988), clinopyroxene stability is closely aligned with that of amphibole and the two only appear stable in a relatively narrow compositional window (Fig. 16a). The coincidental appearance and disappearance of these two phases from the SG1 rhyolites can therefore be explained by minor changes in the conditions of crystallisation in the shallow silicic magmatic system during this time.

Relationships between the temporally separated rhyolitic subgroups <10 ka

The SG2 (7.1–2.7 ka) and SG3 (2.2 ka to present) rhyolites are chemically distinct in comparison with the Oruanui and SG1 rhyolites (Figs. 2, 4). The apparent shift in compositions from SG1 to SG2 was interpreted by Sutton et al. (2000) to mean that a change in magma source was required in the intervening ~3-kyr period. Such interpretations have major implications for inferred magma storage times and repose intervals between eruption groups. Did the SG2 and SG3 magmas originate from different magmatic systems at different positions and depths within the crust (cf. Sutton et al. 1995; Smith et al. 2005) or could they instead have come from the same source as the SG1 magmas but with changing conditions of crystallisation?

Changes in whole-rock and glass chemistry within the SG1 rhyolites and between the SG1 and SG2 rhyolites are accompanied by changes in mineralogy, indicating that phase stability may play a role in the observed chemical shifts. In comparison with the earlier SG1 eruptions, Unit E (last of the SG1 eruptions) has lower whole-rock CaO concentrations, with higher MnO, as well as subtle differences in trace-element concentrations such as Zn, Zr, Sc and Y (Figs. 2, 4). In addition, the compositions of key mineral phases diverge from the trends seen in the earlier units B and C (Figs. 8, 9, 10, 11). Unit E has compositions trending towards the SG2 rhyolites, in line with the observed changes in crystal chemistry. The first of the SG2 eruptions then have significantly higher MnO, Na_2O, Zn, Zr, Y, Sc and lower CaO, La/Sm and Yb/Gd (Figs. 2, 3, 4). However, changes in these elements and elemental ratios can be explained by two processes that do not require a drastic change in source between SG1 and SG2:

1. *Dissolution of amphibole and/or clinopyroxene due to changing intrinsic conditions*. If the magma moved out of the amphibole and/or clinopyroxene stability fields between SG1 and SG2, several elements would be liberated by dissolution, or not sequestered by growth, of these mineral phases (Fig. 15b). For example, trace-element analysis of crystal rims and glass separates for the SG1 rhyolites allows calculation of amphibole-melt partition coefficients of $D_{Mn} = 8$, $D_Y = 9$, $D_{Sc} = 60$, $D_{Zn} = 5$ and $D_{MREE} = 5$–10, and clinopyroxene-melt partition coefficients of $D_{Mn} = 12$, $D_Y = 3$, $D_{Sc} = 50$, $D_{Zn} = 3$ and $D_{MREE} = 2$–4 (Online Resource 4). Liberation into, or retention of, these compatible elements in the melt phase between subgroups and prior to crystal-melt segregation could then help explain stepwise shifts in trace-element compositions (Fig. 15b). Shifting melt compositions are also reflected in differences in orthopyroxene compositions through time. Orthopyroxene-melt partition coefficients of D_{Mn} remain constant between SG1 and SG2 at ~25–30, but there is ~20–30 % relative increase in MnO concentrations in both SG2 orthopyroxene (Fig. 9c–e) and whole-rock compositions (Fig. 2b). This stepwise increase could be achieved through dissolution alone if the original source contained $\leq$5 % clinopyroxene or $\leq$7 % amphibole (or a combination of both: Fig. 15b). Similar compositional shifts can be achieved for other elements compatible in amphibole and clinopyroxene such as Y, Sc and Zn through $\leq$5 % dissolution.
2. *Changes in crystal zonation, plagioclase crystallisation and maturation of the mush system*. Many of the whole-rock compositional trends can be explained by variable degrees of enrichment through inherited crystal cores from precursor magmas. SG1 magmas, for example, have a high proportion of crystals with high-An or high-En cores (Figs. 9, 10). Even though the pumices are generally crystal poor (<7 wt%: Table 2), minor enrichments in highly compatible trace elements such as Sr and V can be explained by inheritance of high-An plagioclase and high-En pyroxene cores, respectively (Fig. 4). Crystal inheritance is much less common in the SG2 eruption products, interpreted to reflect a physical disconnect between the new rhyolite-producing and the precursor dacite-producing magmatic systems (Figs. 9, 10). We infer that this change is likely due to maturation and thickening of the mush system with cooling and extensive crystallisation between eruption groups reflected in the zircon model-age spectra (Barker et al. 2014). The observed changes in CaO and Na_2O can then be explained by further crystallisation of a mineral assemblage dominated by plagioclase and orthopyroxene, consistent with a slight decrease in plagioclase An contents, espe-

cially towards the end of the SG2 eruptions (Table 2; Fig. 15b). For SG3 rhyolites, the opposite is true, with melt compositions more consistent with the dissolution of the observed crystal phases and accompanying increases in most highly compatible elements (Figs. 2, 3, 4). Mineral compositional zoning and thermometry suggest that between the SG2 and SG3 eruptions the magmatic system underwent significant heating, resulting in partial mineral disequilibrium, dissolution and a corresponding shift in melt compositions (Figs. 9, 10, 11, 15b). The connection between subgroups remains evident through similar melt-inclusion compositions (Fig. 6) and reversely zoned SG3 minerals which have core compositions overlapping with corresponding mineral phases from the final SG2 eruptions (Figs. 9g, h, 10g, h).

Summary of Taupo's magmatic system through time

Given the geographically overlapping vent sites (Fig. 1), we suggest that the post-Oruanui eruptives were tapped from a common and likely unitary mush system which changed and evolved through a series of stages as reflected in eruptive products as summarised below:

1. *25.4 ka: Evacuation of the Oruanui magmatic system* (Fig. 17a). Prior to the Oruanui eruption, there was a thermally and compositionally zoned crystal-rich mush body that developed over tens of thousands of years, likely spanning a large portion of the crust from 3.5 to ~10 km depth (Liu et al. 2006; Wilson et al. 2006; Allan 2013). The top of this mush body was quartz bearing and the roots quartz free. The crystal-poor HSR melt-dominant body was then rapidly formed (over <3000 years) via melt extraction from the Oruanui mush, as inferred from zircon model-age spectra (Wilson and Charlier 2009), and compositional zoning relationships in Oruanui amphibole and orthopyroxene crystals (Allan et al. 2013). The uniformity of model temperatures at ~790 °C (Fig. 13) indicates that immediately prior to eruption the melt-dominant body was uniform in composition due to vigorous mixing and lacked any significant thermal gradient (Wilson et al. 2006; Allan 2013). We infer from the presence of two lineages of mafic magmas in the Oruanui eruption and the lack of Oruanui compositions in the post-25.4 ka eruptive sequence that the Oruanui mush source was modified beyond recognition by immediate post-supereruption intrusion of hot mafic magmas. Such an inference is consistent with the small proportion of Oruanui-aged zircons found in the post-Oruanui rhyolites (Barker et al. 2014).
2. *~21–17 ka: Generation and eruption of the post-Oruanui dacites* (Fig. 17b). The higher temperatures, less evolved compositions and inferred depths of storage for the dacites reflect unusual conditions in the early post-Oruanui environment. Mineral zonation patterns are consistent with early episodes of magma mixing, heating and disequilibrium followed by down-temperature fractional crystallisation plus continuing minor assimilation of greywacke country rock and Quaternary plutonic material of Whakamaru age (Charlier et al. 2010). Given the >8 km equilibration depth of the dacite magmas, the residual Oruanui source region may have had a structural influence on where the dacite magmas lodged and may have also contributed material and/or melt through early magma mixing, but any evidence for large-scale inheritance (including zircons) was overprinted. The consistency in the glass and mineral chemistries and similar conditions of storage between the three dacite magmas highlight that their generation processes were repetitive in Taupo's early post-supereruptive environment. Although the dacites appear to have erupted only from the northern region of the Oruanui caldera, it is inferred that similar melt compositions were widespread throughout Taupo's magmatic system, as reflected by the close affinity of the dacites with the SG1 magmas which were erupted from more widely distributed vents (Fig. 1a). Given the close temporal relationship of the dacites with a nearby rhyolite eruption at ~16 ka (Puketarata), we speculate that this renewal of activity may reflect rifting, particularly for Puketarata as its vents form a lineament that lie along a major fault structure (Fig. 1a; Brooker et al. 1993; Leonard et al. 2010).
3. *12–10 ka: Eruption of the SG1 rhyolites* (Fig. 17c). The first-erupted SG1 rhyolites show evidence for extensive crystallisation at depths as shallow as 4–5 km, with subordinate amphibole reflecting temperatures of <~850 °C and high-melt H_2O content of ~5.5 wt%. Minor changes in temperature and/or melt H_2O contents within the SG1 eruptive period possibly resulted in changes in mineral stability following the eruption of units B and C. Eruptions that show evidence for a change in vent site (e.g. Unit E) do not show significant variability in pumice compositions, indicating that the rhyolite-forming magmatic system likely spanned a significant area across the Oruanui collapse structure. The only unit sourced from the northern Taupo region (Acacia Bay dome: Unit D) is similar in composition to the other SG1 rhyolites, but shows further evidence for assimilation of Whakamaru-aged plutonic material (Barker et al. 2014). In addition, the positioning of vents along linear structures aligned or coincidental with modern faults indicates that the local tectonic

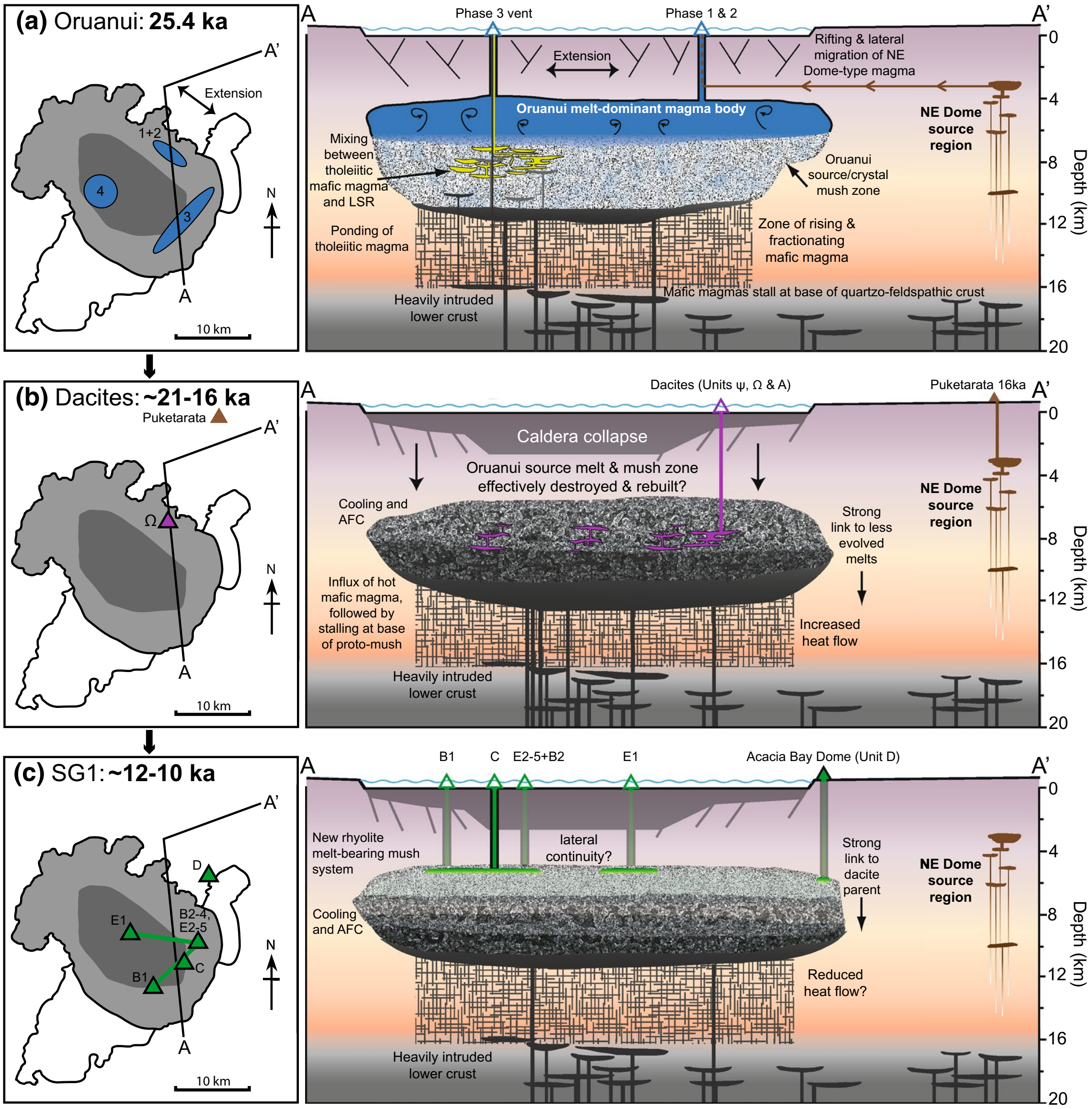

Fig. 17 Schematic illustration of the inferred structural changes in Taupo's magmatic system from **a** the Oruanui magmatic system from Allan (2013) at ~25.4 ka, **b** the post-supereruption dacite eruptions from ~21 to 16 ka and **c** the first rhyolite eruptions (SG1) at ~12 ka. The depth of the melt-dominant lenses and mush zones are inferred from amphibole barometry using Ridolfi et al. (2010), melt-inclusion P_{H2O} data from Liu et al. (2006), and this study. Vent sites are from Wilson (1993, 2001); *coloured tie lines* indicate a syneruptive shift in vent site. The horizontal extent of the magmatic system is inferred from the shape of the Oruanui collapse structure from Davy and Caldwell (1998) and subsequent vent site positions. The lateral continuity of the melt-dominant bodies and mush zones and the exact depth of mafic magma intrusion and ponding are largely unknown. See text for discussion

stress regime may play an important role in determining where the eruptions vented (Rowland et al. 2010; Fig. 1a). The SG1 rhyolites notably coincide with a period of vigorous andesitic volcanism and regional rifting in the southern TVZ (Kohn and Topping 1978; Nairn et al. 1998), and volcanism at Taupo during the SG1 time period may similarly have been influenced by rifting (Rowland et al. 2010).

4. *7–2.8 ka: Eruption of the SG2 rhyolites* (Fig. 18a). During the ~3-kyr period between the SG1 and SG2 eruptions, the magmatic system underwent widespread dissolution of amphibole and clinopyroxene and then crystallisation of a mineral assemblage limited to plagioclase, orthopyroxene, apatite and Fe–Ti oxides. The SG2 rhyolites reflect a more established magmatic system with less evidence for parental dacitic or mafic

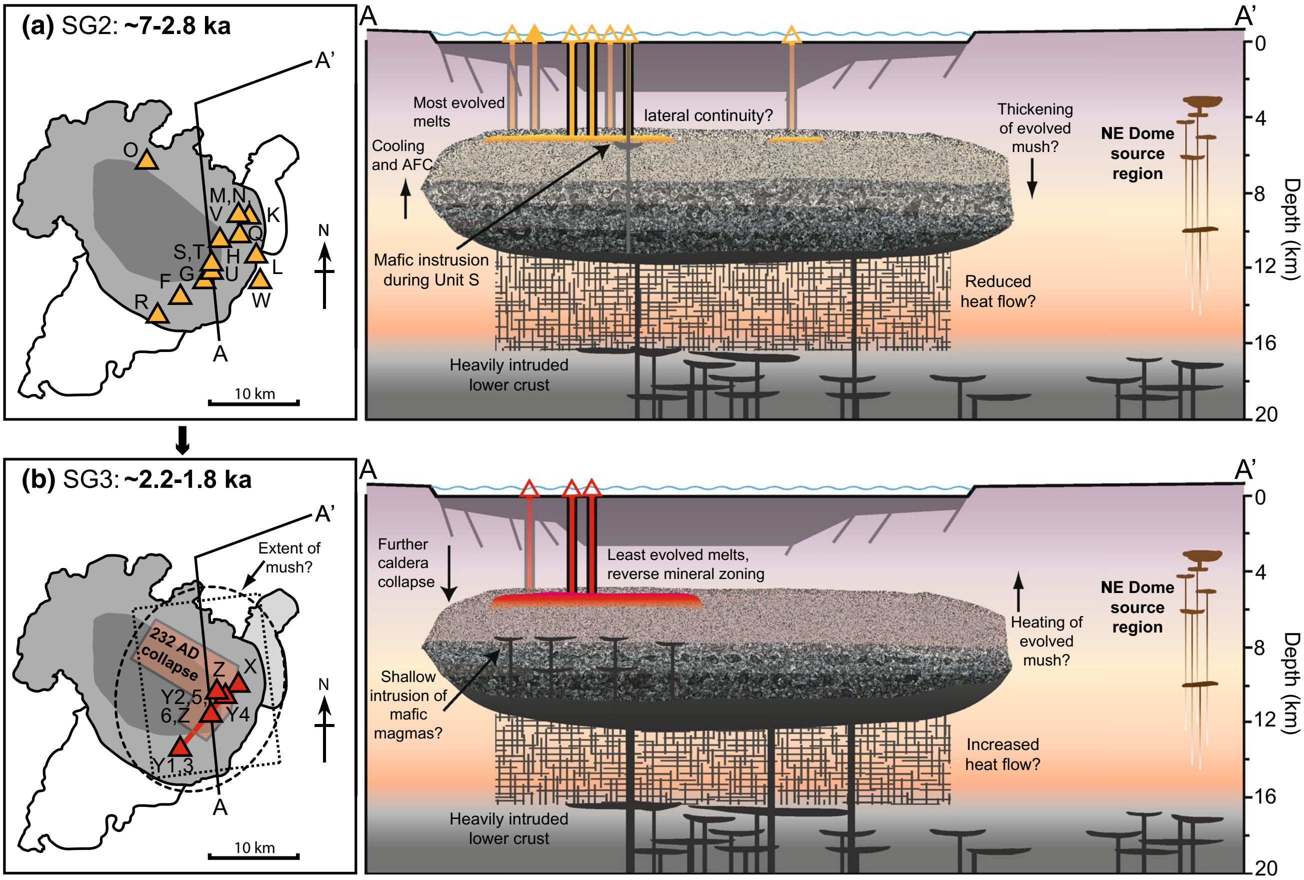

Fig. 18 Schematic illustration of the inferred structural changes in Taupo's magmatic system from **a** the SG2 eruptions from ~7 to 2.8 ka and **b** the lead into the SG3 eruptions at ~2.2 ka. The *black dotted* and *dashed* regions refer to scenarios used to estimate the horizontal extent of the modern silicic mush system as indicated by vent spacing of previous eruptions (see text for discussion). The *red shaded* area refers to the area of 232 AD (Unit Y) caldera collapse as indicated by gravity anomalies (Davy and Caldwell 1998). Other details are as in Fig. 17

melts in inherited crystal cores or melt inclusions. The largest SG2 eruption at 3.5 ka (Unit S) shows evidence for mafic magma intrusion with discrete mafic clasts and mixed pumices (Blake et al. 1992). However, there is no evidence in the subsequent SG2 eruptions for widespread interaction with mafic magma through strong mineral disequilibrium textures or abrupt compositional shifts, despite geographically overlapping vent sites. The final eruptions of SG2 (units U-W), in contrast, show evidence for further cooling and crystallisation of the mush system.

5. *2.2–1.8 ka: Eruption of the SG3 rhyolites* (Fig. 18b). At some point during the ~600-year period between SG2 and SG3 eruptions, the silicic magmatic system underwent significant heating (>30–40 °C increase in magma temperatures) and mineral dissolution as shown by mineral zonation and shifting melt compositions. Notably, the SG3 magmas have the lowest $^{87}Sr/^{86}Sr$ of all post-Oruanui rhyolites (Sutton et al. 2000), inferred (following Knesel et al. 1999) to reflect increased mafic magma recharge through time. These observations are in line with the shift in temperature, trace-element compositions and crystal zonation. No direct evidence has been found in this study for mafic interaction with the Unit X magma. However, the rare presence of small mafic inclusions in pumices from Unit Y and dome carapace pumiceous blocks from eruption Z suggests that mafic magmas were probably the cause of the heating trends seen in Unit X. The rapid heating of Taupo's magmatic system during this time may also have led to the exceptionally large eruption volume of Unit Y in the post-Oruanui sequence. Eruption Y resulted in further caldera collapse in the northeast part of Lake Taupo (Davy and Caldwell 1998). Following eruption Y, Taupo's magmatic system once again experienced an influx of hot mafic material as indicated by mafic inclusions and crystals of a primitive origin in the eruption Z dome carapace pumices.

The contemporary magmatic system

The two most recent eruptions from Taupo at 232 ± 5 AD (Unit Y) and lava extrusions of eruption Z shortly thereafter (collectively the 'Taupo eruption' of Wilson and Walker 1985) comprise the largest eruptive volume in the post-Oruanui sequence, releasing >35 km^3 magma and further destabilising the magmatic system. Important questions arise from the size and nature of this latest activity with regard to future activity and monitoring at Taupo. For example, did the associated caldera collapse change the structure of the mush system? Was the Taupo eruption large enough for the volcano to now require a long period of magmatic recovery and volcanic quiescence or is the system capable of erupting in its present state?

The uniform chemistry and mineralogy within single eruptions (Dunbar et al. 1989b; Sutton et al. 1995; this paper) indicate that the crystal-poor rhyolites erupted from Taupo were assembled as largely unzoned melt-dominant bodies prior to eruption. The key processes occurring within an eruptive cycle must therefore include the effective extraction of melt from the crystal mush and its rapid eruption before cooling and (re-)crystallisation occur. Therefore, the size of the melt-bearing mush system is a critical factor in regard to the impact of a single eruption on the potential for future productivity and behaviour.

To provide a first-order estimate for the potential size of the modern silicic magma system, we provide the following simplified scenario. For an area of 200–300 km^2 (as estimated from the distribution of Oruanui vents and associated caldera collapse), the 530 km^3 Oruanui melt-dominant body (assuming a uniform thickness) is estimated to have been ~1.5–2.5 km thick. This estimate is in accord with the range of model pressures from melt inclusions and amphibole compositions (Liu et al. 2006; Allan et al. 2013; Fig. 17a). An even larger volume of crystal mush is then required below the melt-dominant body to >8–10 km depth, which in turn is buffered and heated by deeper-derived mafic magmas. From the evidence provided here, the silicic mush system was extensively rebuilt in the post-supereruptive environment. The newly rebuilt system likely extends over similar depths to the Oruanui system from at least 8 km (given the depth estimates for the dacite units) to ~5 km depth as inferred from the calculated storage depths of the SG1 rhyolites. The question that then arises is: over what horizontal extent does this zone of hot mush material span, and how much extractible melt is potentially available for eruption? We consider two hypothetical scenarios for the modern structure of Taupo's magmatic system:

1. The melt-generating mush system has reestablished to a similar horizontal extent observed in the pre-Oruanui system. The post-Oruanui vents are spaced over an area of ~280–330 km^2 assuming the minimum area encompassed by a quadrilateral or ellipsoidal shape, respectively (Fig. 18b). Neither of these estimates account for the additional extent of the Oruanui collapse structure and are therefore considered as minima. If the mush system has an assumed thickness of ~3 km (from ~5 to 8 km depth), a volume of melt-bearing material of >800–1000 km^3 can therefore be implied. Assuming the mush had a minimum crystallinity of ~50 %, 35 km^3 of crystal-poor rhyolite magma erupted in Unit Y represents only a relatively minor proportion (~7–10 %) of melt present in the silicic system at the time of eruption.
2. The horizontal extent of the rebuilt post-Oruanui mush is much smaller than the Oruanui system, and the vent spacing does not reflect the true width of the modern system, but instead has been exaggerated by lateral transport of magma to the vents where it was erupted. Such processes are demonstrated to have occurred at Taupo (Wilson and Charlier 2009; Allan et al. 2012) and are seen in the alignment of vent sites in some post-Oruanui eruptions (Wilson 1993; Houghton et al. 2010). However, in these examples, magma transports through diking occurred in a NNE–SSW direction, perpendicular to the direction of extension in TVZ rifting. In contrast, many of the vents at Taupo are linked across opposite directions (Fig. 1a) and so we consider a scenario of extensive lateral transport to be less likely. The minimum area of collapse associated with the eruption of Unit Y is estimated to be ~70–80 km^2 from residual gravity anomalies (Davy and Caldwell 1998; Fig. 18b). We therefore infer a minimum volume estimate for the pre-Unit Y mush system of ~200–250 km^3 assuming a mush thickness of 3 km. Again, 35 km^3 of melt could be readily extracted from this volume of mush assuming a crystallinity of ~50 %.

While our volume estimates are in need of confirmation by geophysical imaging, they are consistent with the trends in eruptive volume and areas in which recent unrest has occurred. Historic unrest episodes at Taupo in 1982–1983 have been linked to magma intrusion at ~8 km depth (Smith et al. 2007; cf. Fig. 18b). Smith et al. (2007) linked the subsequent subsidence measured along the northern shoreline of Lake Taupo to inferred 'dewatering' of >2.5 km^3 of melt, notably a larger volume than most of the post-Oruanui eruptions. These inferences imply that magma bodies are being generated or emplaced even into historic times, but have not (yet?) erupted, raising issues of what controls periods of unrest versus eruption at Taupo and what additional factors will push Taupo into its next phase of eruptive activity.

Taupo's post-supereruptive behaviour: typical or unique in a global context?

Can the post-Oruanui behaviour of Taupo be considered typical for worldwide examples of post-caldera magmatic systems, or does it arise from the hyperactive eruptive behaviour and large inferred magma flux for this volcano (Wilson et al. 2009)? Part of the issue with comparing Taupo's post-supereruptive behaviour with worldwide examples is the uniqueness of having such a large volume eruption combined with the exceptionally frequent occurrence of smaller eruptions and preservation of their products. There were only ~5000 years between the Oruanui eruption and the first dacite eruption, a gap that is within the uncertainties of the age determinations of many worldwide Quaternary large silicic eruptions. At Valles caldera, New Mexico, the 1.25 Ma Bandelier eruption was rapidly followed by large-scale structural resurgence and post-caldera volcanism with low-silica rhyolite ring plain domes erupting 27 ± 27 kyr after the eruption (Phillips et al. 2007). For the 767 ka Bishop Tuff eruption at Long Valley, the post-caldera environment was dominated by both voluminous magmatic (>100 km^3) and structural resurgence. Hildreth (2004) considered that the post-Bishop early rhyolites (751 ± 16–652 ± 14 ka: Mankinen et al. 1986) reflected crystal-poor melts drawn from a similar but largely reorganised mush source to the Bishop but with limited physical interaction with deeper mafic magmas. The 161 ka Kos Plateau Tuff eruption at Kos–Nisyros led to decompression-induced crystallisation within the remaining mush pile, and subsequent eruptions were hotter, drier and more reduced, likely resulting from mafic recharge (Bachmann et al. 2012). In contrast, post-caldera activity at Yellowstone following the 639 ± 2 ka Lava Creek Tuff eruption was dominated by structural resurgence, then longer-term (hundreds of thousands of years) magma replenishment and recycling of modified and hydrothermally altered caldera fill or mush with the eruption of small volume domes from 516 to 473 ka (Bindeman et al. 2001; Girard and Stix 2009). At another extreme, post-caldera activity may be expressed by a switch in magmatic expression. At Aira caldera, for example, following the >400 km^3 caldera-forming event at 22 ka, the large andesitic cone Sakurijima began to grow <10 kyr later on the southern caldera rim and has been the main focus of activity to the modern day (Aramaki 1984).

In the context of other large silicic magmatic systems, Taupo's apparent post-caldera recovery time and rate of renewed volcanism are exceptionally rapid. However, to what extent this rapidity is unmatched elsewhere, either due to the absence of immediately post-caldera eruptions, non-preservation of their products or uncertainties with age resolution, remains unclear. The examples of post-caldera chronologies cited above are from lavas, whereas conditions at Taupo have yielded an overwhelmingly pyroclastic record, represented beyond the caldera-filling lake. There is a wide range of post-caldera behaviour observed, distinctive to each setting worldwide. Controlling variables may include (but are not limited to) magma supply rate, the size of the pre-caldera mush body and what proportion was erupted, the tectonic setting and stress state of the crust, magmatic system structure and components, heat flow in the crust and eruption triggers. In the TVZ, Taupo's rapid post-caldera recovery may simply be a direct consequence of its high magma flux (Wilson et al. 2009). Worldwide, large-scale eruptions invariably act to modify the magmatic system structure, with post-caldera reorganisation resulting in an influx of new magma which can accompany structural and/or magmatic resurgence. Notably, structural resurgence is not observed at Taupo, again reflecting a feedback response between magma injection (inflation) and extensional tectonics so that surface uplift on short timescales is followed by subsidence on longer timescales (Manville and Wilson 2003; Ellis et al. 2007).

Large silicic magma reservoirs are often considered to result from longevity of magmatic episodes and gradual thermomechanical evolution over timescales of hundreds of thousands to millions of years (e.g. de Silva and Gregg 2014). However, as shown here, supereruptions or large-scale caldera-forming events may act to significantly alter the structure and subsequent behaviour of the magmatic system and style of volcanism on much shorter timescales. In the case of Taupo volcano, the Oruanui eruption acted to largely destroy and reset the history of the magmatic system so that the modern day volcano and its eruptive products show little connection in timing and composition to their supereruptive progenitor.

Conclusions

Following the 25.4 ka Oruanui supereruption, Taupo volcano experienced significant changes, with eruptive products reflecting the fine-scale temporal reorganisation, reconstruction and evolution of a largely new and very active magmatic system. The first dacitic eruptions between 21 and 17 ka reflect reorganisation of the magmatic system at a time of high heat flow and mafic intrusion. Dacite mineralogies and compositions reflect a rebuilding silicic system that then cooled and crystallised, developing a melt-bearing crystal mush and density trap from which subsequently rhyolite magmas began to be tapped only 13.5 kyr after the supereruption. The three rhyolite magma subgroups from 12 ka to present show fine-scale temporal changes in melt chemistry and mineral phase stability with fluctuating conditions of crystallisation, which are closely linked to the development, stabilisation and maturation of a new, probably unitary mush system. Rare mafic clasts in the post-Oruanui eruptions suggest that although the silicic magmatic system has changed in character, the deeper mafic roots that provide heat and control the stability of the overlying silicic system have remained similar. Temporal changes in silicic magma chemistry and eruptive frequencies reflect the evolution of a recovering magmatic system combined with heating and cooling associated with fluctuating mafic inputs and periods of rifting that control the accumulation and release of crystal-poor rhyolite magma. The patterns of magmatism and volcanism through time are consistent with the reestablishment of a large mush system beneath Taupo volcano (at least 200 and possibly up to 1000 km^3 in volume). This system continues to actively produce significant volumes of melt to the modern day, as implied by the modern hydrothermal heat flux (Bibby et al. 1995) and modelling of the most recent unrest episode (Smith et al. 2007). Despite the recent 232 AD eruption being the largest in the past 25 kyr, we consider that Taupo volcano will continue its hyperactive eruptive behaviour and that it is well capable of resuming volcanism within timescales of human interest and concern.

Acknowledgments We thank John Gamble, Roger Briggs, Michelle Coombs, George Cooper, Melissa Rotella and Bruce Charlier for helpful discussions. Olivier Bachmann, Benjamin Andrews and an anonymous reviewer are thanked for their constructive comments. We are grateful to the late John Watson for his analytical services. New Zealand Forest Managers and Timberlands kindly allowed access to Lake Taupo Forest and Waimihia Forest, respectively, for sample collection. We acknowledge financial support from the Marsden Fund of the Royal Society of New Zealand (Grant VUW0813), a Royal Society of New Zealand James Cook Fellowship to CJNW, and a Victoria University Doctoral Scholarship, a Postgraduate Research Excellence Award and two Victoria University Strategic Research Grants awarded to SJB. CIS acknowledges the Japan Society for the Promotion of Science (JSPS) postdoctoral fellowship for work at JAMSTEC with A.R.L. Nichols.

References

Allan ASR (2013) The Oruanui eruption: insights into the generation and dynamics of the world's youngest supereruption. PhD thesis, Victoria University, Wellington, New Zealand (http://hdl.handle.net/10063/2975)

Allan ASR, Wilson CJN, Millet M-A, Wysoczanski RJ (2012) The invisible hand: tectonic triggering and modulation of a rhyolitic supereruption. Geology 40:563–566

Allan ASR, Morgan DJ, Wilson CJN, Millet M-A (2013) From mush to eruption in centuries: assembly of the super-sized Oruanui magma body. Contrib Mineral Petrol 166:143–164

Andersen DJ, Lindsley DH (1988) Internally consistent solution models for Fe–Mg–Mn–Ti oxides: fe–Ti oxides. Am Mineral 73:714–726

Aramaki S (1984) Formation of the Aira Caldera, southern Kyushu, ~22,000 years ago. J Geophys Res 89:8485–8501

Arculus RJ (2003) Use and abuse of the terms calcalkaline and calcalkalic. J Petrol 44:929–935

Bachmann O, Bergantz GW (2004) On the origin of crystal-poor rhyolites: extracted from batholithic crystal mushes. J Petrol 45:1565–1582

Bachmann O, Bergantz G (2008) The magma reservoirs that feed supereruptions. Elements 4:17–21

Bachmann O, Deering CD, Ruprecht JS, Huber C, Skopelitis A, Schnyder C (2012) Evolution of silicic magmas in the Kos–Nisyros volcanic center, Greece: a petrological cycle associated with caldera collapse. Contrib Mineral Petrol 163:151–166

Bacon CR, Hirschmann MM (1988) Mg/Mn partitioning as a test for equilibrium between coexisting Fe–Ti oxides. Am Mineral 73:57–61

Bain AA, Jellinek AM, Wiebe RA (2013) Quantitative field constraints on the dynamics of silicic magma chamber rejuvenation and overturn. Contrib Mineral Petrol 165:1275–1294

Barker SJ, Wilson CJN, Smith EGC, Charlier BLA, Wooden J, Hiess J, Ireland TR (2014) Post-supereruption magmatic reconstruction of Taupo volcano (New Zealand), as reflected in zircon ages and trace elements. J Petrol 55:1511–1533

Baumgart IL (1954) Some ash showers of the central North Island. NZ J Sci Technol B35:456–467

Bégué F, Gualda GAR, Ghiorso MS, Pamukcu AS, Kennedy BM, Gravley DM, Deering CD, Chambefort I (2014) Phase-equilibrium geobarometers for silicic rocks based on rhyolite-MELTS. Part 2: application to Taupo Volcanic Zone rhyolites. Contrib Mineral Petrol 168:1082

Behrens H, Ohlhorst S, Holtz F, Champenois M (2004) CO_2 solubility in dacitic melts equilibrated with H_2O–CO_2 fluids: implications for modeling the solubility of CO_2 in silicic melts. Geochim Cosmochim Acta 68:4687–4703

Bibby HM, Caldwell TG, Davey FJ, Webb TH (1995) Geophysical evidence on the structure of the Taupo Volcanic Zone and its hydrothermal circulation. J Volcanol Geotherm Res 68:29–58

Bindeman IN, Valley JW, Wooden JL, Persing HM (2001) Post-caldera volcanism: in situ measurement of U–Pb age and oxygen isotope ratio in Pleistocene zircons from Yellowstone caldera. Earth Planet Sci Lett 189:197–206

Blake S, Wilson CJN, Smith IEM, Walker GPL (1992) Petrology and dynamics of the Waimihia mixed magma eruption, Taupo Volcano, New Zealand. J Geol Soc Lond 149:193–207

Blundy J, Cashman K (2008) Petrological reconstruction of magmatic system variables and processes. In: Putirka KD, Tepley FJ (eds) Minerals, inclusions and volcanic processes. Rev Mineral Geochem 69:179–239

Blundy JD, Wood BJ (1991) Crystal-chemical controls on the partitioning of Sr and Ba between plagioclase feldspar, silicate melts, and hydrothermal solutions. Geochim Cosmochim Acta 55:193–209

Brooker MR, Houghton BF, Wilson CJN, Gamble JA (1993) Pyroclastic phases of a rhyolitic dome-building eruption: Puketarata tuff ring, Taupo Volcanic Zone, New Zealand. Bull Volcanol 55:395–406

Burgisser A, Scaillet B (2007) Redox evolution of a degassing magma rising to the surface. Nature 445:194–197

Caricchi L, Annen C, Blundy J, Simpson G, Pinel V (2014) Frequency and magnitude of volcanic eruptions controlled by magma injection and buoyancy. Nature Geosci 7:126–130

Cashman K, Blundy J (2013) Petrological cannibalism: the chemical and textural consequences of incremental magma body growth. Contrib Mineral Petrol 166:703–729

Charlier BLA, Wilson CJN, Lowenstern JB, Blake S, van Calsteren PW, Davidson JP (2005) Magma generation at a large, hyperactive silicic volcano (Taupo, New Zealand) revealed by U–Th and U–Pb systematics in zircons. J Petrol 46:3–32

Charlier BLA, Wilson CJN, Davidson JP (2008) Rapid open-system assembly of a large silicic magma body: time-resolved evidence from cored plagioclase crystals in the Oruanui eruption deposits, New Zealand. Contrib Mineral Petrol 156:799–813

Charlier BLA, Wilson CJN, Mortimer N (2010) Evidence from zircon U–Pb age spectra for crustal structure and felsic magma genesis at Taupo volcano, New Zealand. Geology 38:915–918

Cole JW, Deering CD, Burt RM, Sewell S, Shane PAR, Matthews NE (2014) Okataina Volcanic Centre, Taupo Volcanic Zone, New Zealand: a review of volcanism and synchronous pluton development in an active, dominantly silicic caldera system. Earth Sci Rev 128:1–17

Conrad WK, Nicholls IA, Wall VJ (1988) Water-saturated and -undersaturated melting of metaluminous and peraluminous crustal compositions at 10 kb: evidence for the origin of silicic magmas in the Taupo Volcanic Zone, New Zealand, and other occurrences. J Petrol 29:765–803

Coombs ML, Gardner JE (2001) Shallow storage conditions for the rhyolite of the 1912 eruption at Novarupta, Alaska. Geology 29:775–778

Coombs ML, Sisson TW, Bleick HA, Henton SM, Nye CJ, Payne AL, Cameron CE, Larsen JF, Wallace KL, Bull KF (2013) Andesites of the 2009 eruption of Redoubt Volcano, Alaska. J Volcanol Geotherm Res 259:349–372

Dall'Agnol R, Scaillet B, Pichavant M (1999) An experimental study of a lower Proterozoic A-type granite from the eastern Amazonian craton, Brazil. J Petrol 40:1673–1698

Davy BW, Caldwell TG (1998) Gravity, magnetic and seismic surveys of the caldera complex, Lake Taupo, North Island, New Zealand. J Volcanol Geotherm Res 81:69–89

de Silva SL, Gregg PM (2014) Thermomechanical feedbacks in magmatic systems: implications for growth, longevity, and evolution of large caldera-forming magma reservoirs and their supereruptions. J Volcanol Geotherm Res 282:77–91

Deering CD, Bachmann O, Dufek J, Gravley DM (2011) Rift-related transition from andesite to rhyolite volcanism in the Taupo Volcanic Zone (New Zealand) controlled by crystal-melt dynamics in mush zones with variable mineral assemblages. J Petrol 52:2243–2263

Dufek J, Bachmann O (2010) Quantum magmatism: magmatic compositional gaps generated by melt-crystal dynamics. Geology 38:687–690

Dunbar NW, Kyle PR (1993) Lack of volatile gradient in the Taupo plinian-ignimbrite transition: evidence from melt inclusion analysis. Am Mineral 78:612–618

Dunbar NW, Hervig RL, Kyle PR (1989a) Determination of pre-eruptive H_2O, F and Cl contents of silicic magmas using melt inclusions: examples from Taupo volcanic centre, New Zealand. Bull Volcanol 51:177–184

Dunbar NW, Kyle PR, Wilson CJN (1989b) Evidence for limited zonation in silicic magma systems, Taupo Volcanic Zone, New Zealand. Geology 17:234–236

Ellis SM, Wilson CJN, Bannister S, Bibby HM, Heise W, Wallace L, Patterson N (2007) A future magma inflation event under the rhyolitic Taupo volcano, New Zealand: numerical models based on constraints from geochemical, geological, and geophysical data. J Volcanol Geotherm Res 168:1–27

Erdmann S, Martle C, Pichavant M, Kushnir A (2014) Amphibole as an archivist of magmatic crystallization conditions: problems, potential, and implications for inferring magma storage prior to the paroxysmal 2010 eruption of Mount Merapi, Indonesia. Contrib Mineral Petrol 167:1016

Ersoy EY (2013) PETROMODELER (Petrological Modeler) a Microsoft Excel spreadsheet program for modelling melting, mixing, crystallization and assimilation processes in magmatic systems. Turkish J Earth Sci 22:115–125

Evans BW, Scaillet B, Kuehner SM (2006) Experimental determination of coexisting iron- titanium oxides in the systems FeTiAlO, FeTiAlMgO, FeTiAlMnO, and FeTiAlMgMnO at 800 and 900°C, 1–4 kbar, and relatively high oxygen fugacity. Contrib Mineral Petrol 152:149–167

Froggatt PC, Lowe DJ (1990) A review of late Quaternary silicic and some other tephra formations from New Zealand: their stratigraphy, nomenclature, distribution, volume, and age. NZ J Geol Geophys 33:89–109

Gamble JA, Smith IEM, Graham IJ, Kokelaar BP, Cole JW, Houghton BF, Wilson CJN (1990) The petrology, phase relations and tectonic setting of basalts from the Taupo Volcanic Zone, New Zealand and the Kermadec Island Arc—Havre Trough, SW Pacific. J Volcanol Geotherm Res 43:253–270

Gamble JA, Smith IEM, McCulloch MT, Graham IJ, Kokelaar BP (1993) The geochemistry and petrogenesis of basalts from the Taupo Volcanic Zone and Kermadec Island Arc, S.W. Pacific. J Volcanol Geotherm Res 54:265–290

Gelman SE, Deering CD, Gutierrez FJ, Bachmann O (2013) Evolution of the Taupo volcanic center, New Zealand: petrological and thermal constraints from the Omega dacite. Contrib Mineral Petrol 166:1355–1374

Ghiorso MS, Evans BW (2008) Thermodynamics of rhombohedral oxide solid solutions and a revision of the Fe–Ti two-oxide geothermometer and oxygen-barometer. Am J Sci 308:957–1039

Girard G, Stix J (2009) Buoyant replenishment in silicic magma reservoirs: experimental approach and implications for magma dynamics, crystal mush remobilization, and eruption. J Geophys Res 114:B08203

Glazner AF, Bartley JM, Coleman DS, Gray W, Taylor RZ (2004) Are plutons assembled over millions of years by amalgamation from small magma chambers? GSA Today 14(4/5):4–11

Graham IJ, Hackett WR (1987) Petrology of calc-alkaline lavas from Ruapehu volcano and related vents, Taupo Volcanic Zone, New Zealand. J Petrol 28:531–567

Graham IJ, Gulson BL, Hedenquist JW, Mizon K (1992) Petrogenesis of Late Cenozoic volcanic rocks from the Taupo Volcanic Zone, New Zealand, in the light of new lead isotope data. Geochim Cosmochim Acta 56:2797–2819

Graham IJ, Cole JW, Briggs RM, Gamble JA, Smith IEM (1995) Petrology and petrogenesis of volcanic rocks from the Taupo Volcanic Zone: a review. J Volcanol Geotherm Res 68:59–87

Hackett WR (1985) Geology and petrology of Ruapehu Volcano and related vents. PhD thesis, Victoria University of Wellington, Wellington, New Zealand

Harrison A, White RS (2006) Lithospheric structure of an active backarc basin: the Taupo Volcanic Zone, New Zealand. Geophys J Int 167:968–990

Healy J (1964) Stratigraphy and chronology of late Quaternary volcanic ash in Taupo, Rotorua, and Gisborne districts. Part 1. Dating of the younger volcanic eruptions of the Taupo region. NZ Geol Surv Bull 73:7–42

Heise W, Caldwell TG, Bibby HM, Bennie SL (2010) Three dimensional electrical resistivity image of magma beneath an active continental rift, Taupo Volcanic Zone, New Zealand. Geophys Res Lett 37:L1030

Hildreth W (1981) Gradients in silicic magma chambers: implications for lithospheric magmatism. J Geophys Res 86:10153–10192

Hildreth W (2004) Volcanological perspectives on Long Valley, Mammoth Mountain, and Mono Craters: several contiguous but discrete systems. J Volcanol Geotherm Res 136:169–198

Hildreth W, Wilson CJN (2007) Compositional zoning of the Bishop Tuff. J Petrol 48:951–999

Hogg AG, Lowe DJ, Palmer J, Boswijk G, Ramsey CB (2012) Revised calendar date for the Taupo eruption derived by ^{14}C

wiggle-matching using a New Zealand kauri ^{14}C calibration data set. Holocene 22:439–449

Houghton BF, Carey RJ, Cashman KV, Wilson CJN, Hobden BJ, Hammer JE (2010) Diverse patterns of ascent, degassing, and eruption of rhyolite magma during the 1.8 ka Taupo eruption, New Zealand: evidence from clast vesicularity. J Volcanol Geotherm Res 195:31–47

Ihinger PD, Hervig RL, McMillan PF (1994) Analytical methods for volatiles in glasses. In: Carroll MR, Holloway JR (eds) Volatiles in magmas. Rev Mineral Geochem 30:67–121

Klimm K, Holtz F, Johannes W, King PL (2003) Fractionation of metaluminous A-type granites: an experimental study of the Wangrah Suite, Lachlan Fold Belt, Australia. Precamb Res 124:327–341

Knesel KM, Davidson JP, Duffield WA (1999) Evolution of silicic magma through assimilation and subsequent recharge: evidence from Sr isotopes in sanidine phenocrysts, Taylor Creek Rhyolite, NM. J Petrol 40:773–786

Kohn BP, Topping WW (1978) Time-space relationships between late Quaternary rhyolitic and andesitic volcanism in the southern Taupo Volcanic Zone, New Zealand. Geol Soc Am Bull 89:1265–1271

Lee C-TA, Bachmann O (2014) How important is the role of crystal fractionation in making intermediate magmas? Insights from Zr and P systematics. Earth Planet Sci Lett 393:266–274

Leonard GS, Begg JG, Wilson CJN (2010) Geology of the Rotorua area: scale 1:250,000. Inst Geol Nucl Sci 1:250,000 geological map 5. Institute of Geological & Nuclear Sciences Limited, Lower Hutt, New Zealand

Lipman PW (1965) Chemical comparison of glassy and crystalline volcanic rocks. US Geol Surv Bull 1201-D: 24 pp

Lipman PW (2007) Incremental assembly and prolonged consolidation of Cordilleran magma chambers: evidence from the Southern Rocky Mountain volcanic field. Geosphere 3:42–70

Lipman PW, Bachmann O (2015) Ignimbrites to batholiths: integrating perspectives from geological, geophysical, and geochronological data. Geosphere 11:705–743

Liu Y, Anderson AT, Wilson CJN, Davis AM, Steele IM (2006) Mixing and differentiation in the Oruanui rhyolitic magma, Taupo, New Zealand: evidence from volatiles and trace elements in melt inclusions. Contrib Mineral Petrol 151:71–87

Malfait WJ, Seifert R, Petitgirard S, Perrillat J-P, Mezouar M, Ota T, Nakamura E, Lerch P, Sanchez-Valle C (2014) Supervolcano eruptions driven by melt buoyancy in large silicic magma chambers. Nature Geosci 7:122–125

Mankinen EA, Grommé CS, Dalrymple GB, Lanphere MA, Bailey RA (1986) Paleomagnetism and K–Ar ages of volcanic rocks from Long Valley caldera, California. J Geophys Res 91:633–652

Manville V, Wilson CJN (2003) Interactions between volcanism, rifting and subsidence: implications of intracaldera palaeoshorelines at Taupo volcano, New Zealand. J Geol Soc Lond 160:3–6

Marsh BD (1981) On the crystallinity, probability of occurrence, and rheology of lava and magma. Contrib Mineral Petrol 78:85–98

Miller CF, Wark DA (2008) Supervolcanoes and their explosive supereruptions. Elements 4:11–16

Millet M-A, Tutt CM, Handler MH, Baker JA (2014) Processes and time scales of dacite magma assembly and eruption at Tauhara volcano, Taupo Volcanic Zone, New Zealand. Geochem Geophys Geosyst 15:213–237

Miyashiro A (1974) Volcanic rock series in island arcs and active continental margins. Am J Sci 274:321–355

Nairn IA, Kobayashi T, Nakagawa M (1998) The ~ 10 ka multiple vent pyroclastic eruption sequence at Tongariro Volcanic Centre, Taupo Volcanic Zone, New Zealand: part 1. Eruptive processes during regional extension. J Volcanol Geotherm Res 86:19–44

Newman S, Lowenstern JB (2002) VolatileCalc: a silicate melt-H_2O–CO_2 solution model written in Visual Basic for Excel. Comput Geosci 28:597–604

Nichols ARL, Wysoczanski RJ (2007) Using micro-FTIR spectroscopy to measure volatile contents in small and unexposed inclusions hosted in olivine crystals. Chem Geol 242:371–384

O'Neill HS, Pownceby MI (1993) Thermodynamic data from redox reactions at high- temperatures 1. An experimental and theoretical assessment of the electrochemical method using stabilized zirconia electrolytes, with revised values for the Fe–FeO, CO–COO, Ni, NiO and Cu–Cu_2O oxygen buffers, and new data for the W–WO_2 buffer. Contrib Mineral Petrol 114:296–314

Okumura S, Nakamura M, Nakashima S (2003) Determination of molar absorptivity of IR fundamental OH-stretching vibration in rhyolitic glasses. Am Mineral 88:1657–1662

Palme H, Beer H (1993) Abundances of the elements in the solar system. In: Voight HH (ed) Landolt-Börnstein, Group VI: astronomy and astrophysics: instruments; methods; solar system, vol 3(a). Springer, Berlin, pp 196–221

Pearce NJG, Westgate JA, Perkins WT (1996) Developments in the analysis of volcanic glass shards by laser ablation ICP–MS: quantitative and single internal standard multi-element methods. Quat Int 34:213–227

Phillips EH, Goff F, Kyle PR, McIntosh WC, Dunbar NW, Gardner JN (2007) The $^{40}Ar/^{39}Ar$ age constraints on the duration of resurgence at the Valles caldera, New Mexico. J Geophys Res 112:B08201

Putirka KD (2008) Thermometers and barometers for volcanic systems. In: Putirka K, Tepley FJ (eds) Minerals, inclusions and volcanic processes. Rev Mineral Geochem 69:61–120

Ramsey MH, Potts PJ, Webb PC, Watkins P, Watson JS, Coles BJ (1995) An objective assessment of analytical method precision: comparison of ICP-AES and XRF for the analysis of silicate rocks. Chem Geol 124:1–19

Ridolfi F, Renzulli A, Puerini M (2010) Stability and chemical equilibrium of amphibole in calc-alkaline magmas: an overview, new thermobarometric formulations and application to subduction-related volcanoes. Contrib Mineral Petrol 160:45–66

Rowland JV, Wilson CJN, Gravley DM (2010) Spatial and temporal variations in magma- assisted rifting, Taupo Volcanic Zone, New Zealand. J Volcanol Geotherm Res 190:89–108

Sauerzapf U, Lattard D, Burchard M, Engelman R (2008) The titanomagnetite-ilmenite equilibrium: new experimental data and thermo-oxybarometric application to the crystallization of basic to intermediate rocks. J Petrol 49:1161–1185

Saunders KE (2009) Micro-analytical studies of the petrogenesis of silicic arc magmas in the Taupo Volcanic Zone and southern Kermadec Arc, New Zealand. PhD thesis, Victoria University of Wellington, Wellington, New Zealand (http://hdl.handle.net/10063/943)

Shane P, Smith VC (2013) Using amphibole crystals to reconstruct magma storage temperatures and pressures for the post-caldera collapse volcanism at Okataina volcano. Lithos 156–159:159–170

Shane P, Martin SB, Smith VC, Beggs KF, Darragh MB, Cole JW, Nairn IA (2007) Multiple rhyolite magmas and basalt injection in the 17.7 ka Rerewhakaaitu eruption episode from Tarawera volcanic complex, New Zealand. J Volcanol Geotherm Res 164:1–26

Shane P, Nairn IA, Smith VC, Darragh M, Beggs KF, Cole JW (2008) Silicic recharge of multiple rhyolite magmas by basaltic intrusion during the 22.6 ka Okaraka eruption episode, New Zealand. Lithos 103:527–549

Simon JI, Weis D, DePaolo DJ, Renne PR, Mundil R, Schmitt AK (2014) Assimilation of preexisting Pleistocene intrusions at Long Valley by periodic magma recharge accelerates rhyolite generation: rethinking the remelting model. Contrib Mineral Petrol 167:955

Smith VC, Shane P, Nairn IA (2005) Trends in rhyolite geochemistry, mineralogy, and magma storage during the last 50 kyr at Okataina and Taupo volcanic centres, Taupo Volcanic Zone, New Zealand. J Volcanol Geotherm Res 148:372–406

Smith EGC, Williams TD, Darby DJ (2007) Principal component analysis and modeling of the subsidenceof the shoreline of Lake Taupo, New Zealand, 1983–1999: evidence for dewatering of a magmatic intrusion? J Geophys Res 112:B08406

Smith VC, Shane P, Nairn IA (2010) Insights into silicic melt generation using plagioclase, quartz and melt inclusions from the caldera-forming Rotoiti eruption, Taupo volcanic zone, New Zealand. Contrib Mineral Petrol 160:951–971

Sutton AN, Blake S, Wilson CJN (1995) An outline geochemistry of rhyolite eruptives from Taupo volcanic centre, New Zealand. J Volcanol Geotherm Res 68:153–175

Sutton AN, Blake S, Wilson CJN, Charlier BLA (2000) Late Quaternary evolution of a hyperactive rhyolite magmatic system: Taupo volcanic centre, New Zealand. J Geol Soc Lond 157:537–552

Tamic N, Behrens H, Holtz F (2001) The solubility of H_2O and CO_2 in rhyolitic melts in equilibrium with a mixed CO_2–H_2O fluid phase. Chem Geol 174:333–347

Vandergoes MJ, Hogg AG, Lowe DJ, Newnham RM, Denton GH, Southon J, Barrell DJA, Wilson CJN, McGlone MS, Allan ASR, Almond PC, Petchey F, Dabell K, Dieffenbacher-Krall AC, Blaauw M (2013) A revised age for the Kawakawa/Oruanui tephra, a key marker for the last Glacial Maximum in New Zealand. Quat Sci Rev 74:195–201

Vigneresse JL, Barbey P, Cuney M (1996) Rheological transitions during partial melting and crystallization with application to felsic magma segregation and transfer. J Petrol 37:1579–1600

von Aulock FW, Kennedy BM, Schipper CI, Castro JM, Martin DE, Oze C, Watkins JM, Wallace PJ, Puskar L, Bégué F, Nichols ARL, Tuffen H (2014) Advances in Fourier transform infrared spectroscopy of natural glasses: from sample preparation to data analysis. Lithos 206–207:52–64

Vucetich CG, Pullar WA (1973) Holocene tephra formations erupted in the Taupo area and interbedded tephras from other volcanic sources. NZ J Geol Geophys 16:745–780

Wilson CJN (1993) Stratigraphy, chronology, styles and dynamics of late Quaternary eruptions from Taupo volcano, New Zealand. Phil Trans R Soc Lond A343:205–306

Wilson CJN (2001) The 26.5 ka Oruanui eruption, New Zealand: an introduction and overview. J Volcanol Geotherm Res 112:133–174

Wilson CJN, Charlier BLA (2009) Rapid rates of magma generation at contemporaneous magma systems, Taupo volcano, New Zealand: insights from U–Th model-age spectra in zircons. J Petrol 50:875–907

Wilson CJN, Walker GPL (1985) The Taupo eruption, New Zealand I. General aspects. Phil Trans R Soc Lond A314:199–228

Wilson CJN, Houghton BF, Lloyd EF (1986) Volcanic history and evolution of the Maroa-Taupo area, central North Island. In: Smith IEM (ed) Late Cenozoic Volcanism in New Zealand. R Soc NZ Bull 23:194–223

Wilson CJN, Houghton BF, McWilliams MO, Lanphere MA, Weaver SD, Briggs RM (1995) Volcanic and structural evolution of Taupo Volcanic Zone, New Zealand: a review. J Volcanol Geotherm Res 68:1–28

Wilson CJN, Blake S, Charlier BLA, Sutton AN (2006) The 26.5 ka Oruanui eruption, Taupo volcano, New Zealand: development, characteristics and evacuation of a large rhyolitic magma body. J Petrol 47:35–69

Wilson CJN, Gravley DM, Leonard GS, Rowland JV (2009). Volcanism in the central Taupo Volcanic Zone, New Zealand: tempo, styles and controls. In: Thordarson T et al. (eds) Studies in volcanology: the legacy of George Walker. IAVCEI Proc Volcanol 2:225–247

Wolff JA (1985) The effect of explosive eruption processes on geochemical patterns within pyroclastic deposits. J Volcanol Geotherm Res 26:189–201

Wysoczanski R, Tani K (2006) Spectroscopic FTIR imaging of water species in silicic volcanic glasses and melt inclusions: an example from the Izu-Bonin arc. J Volcanol Geotherm Res 156:302–314